# Canadian Beaufort Sea - Marine Ecosystem Assessment (CBS-MEA) report on the physical system - 2018

Ryan Galley, Andrea Niemi, Jane Eert, Andrew Majewski, Matthew Friesen, William Williams

Fisheries and Oceans Canada
Freshwater Institute
501 University Crescent
Winnipeg, Manitoba
Canada, R3T 2N6

2026

Canadian Technical Report of Hydrography and Ocean Sciences 428

Fisheries and Oceans Canada | Pêches et Océans Canada

Canada

**Canadian Technical Report of Hydrography and Ocean Sciences**

Technical reports contain scientific and technical information of a type that represents a contribution to existing knowledge but which is not normally found in the primary literature. The subject matter is generally related to programs and interests of the Oceans and Science sectors of Fisheries and Oceans Canada.

Technical reports may be cited as full publications. The correct citation appears above the abstract of each report. Each report is abstracted in the data base *Aquatic Sciences and Fisheries Abstracts.*

Technical reports are produced regionally but are numbered nationally. Requests for individual reports will be filled by the issuing establishment listed on the front cover and title page.

Regional and headquarters establishments of Ocean Science and Surveys ceased publication of their various report series as of December 1981. A complete listing of these publications and the last number issued under each title are published in the *Canadian Journal of Fisheries and Aquatic Sciences*, Volume 38: Index to Publications 1981. The current series began with Report Number 1 in January 1982.

**Rapport technique canadien sur l'hydrographie et les sciences océaniques**

Les rapports techniques contiennent des renseignements scientifiques et techniques qui constituent une contribution aux connaissances actuelles mais que l'on ne trouve pas normalement dans les revues scientifiques. Le sujet est généralement rattaché aux programmes et intérêts des secteurs des Océans et des Sciences de Pêches et Océans Canada.

Les rapports techniques peuvent être cités comme des publications à part entière. Le titre exact figure au-dessus du résumé de chaque rapport. Les rapports techniques sont résumés dans la base de données *Résumés des sciences aquatiques et halieutiques*.

Les rapports techniques sont produits à l'échelon régional, mais numérotés à l'échelon national. Les demandes de rapports seront satisfaites par l'établissement auteur dont le nom figure sur la couverture et la page de titre.

Les établissements de l'ancien secteur des Sciences et Levés océaniques dans les régions et à l'administration centrale ont cessé de publier leurs diverses séries de rapports en décembre 1981. Vous trouverez dans l'index des publications du volume 38 du *Journal canadien des sciences halieutiques et aquatiques*, la liste de ces publications ainsi que le dernier numéro paru dans chaque catégorie. La nouvelle série a commencé avec la publication du rapport numéro 1 en janvier 1982.

Canadian Technical Report of
Hydrography and Ocean Sciences 428

2026

# Canadian Beaufort Sea - Marine Ecosystem Assessment (CBS-MEA) report on the physical system - 2018

by

Ryan Galley, Andrea Niemi, Jane Eert, Andrew Majewski, Matthew Friesen, William Williams

Fisheries and Oceans Canada
Freshwater Institute
501 University Crescent
Winnipeg, Manitoba
Canada, R3T 2N6

© His Majesty the King in Right of Canada, as represented by the Minister of the Department of Fisheries and Oceans, 2026

This work is licensed under the Open Government Licence

Cat. No. Fs.97-18/428E-PDF ISBN 978-1-100-01146-2 ISSN 1488-5417

https://doi.org/10.60825/txnm-q171

Correct Citation for this publication:

Galley, R., Niemi, A., Eert, J., Majewski, A., Friesen, M., Williams, W. 2026. Canadian Beaufort Sea - Marine Ecosystem Assessment (CBS-MEA) report on the physical system – 2018. Can. Tech. Rep. Hydrogr. Ocean Sci. 428: ix + 106 p. https://doi.org/10.60825/txnm-q171

# TABLE OF CONTENTS

**LIST OF FIGURES** ..... iv

**LIST OF TABLES** ..... vii

**ABSTRACT** ..... viii

**RÉSUMÉ** ..... ix

**1 Introduction** ..... 1

**2 Data and Methods** ..... 3

**2.1 Environmental Forcing** ..... 4

**2.2 Sea Ice Concentration and Motion** ..... 4

**2.3 Sea ice-adjusted Surface Solar Radiation Downwards** ..... 5

**2.4 CBS-MEA sampling** ..... 6

**3 Results and Discussion** ..... 7

**3.1 Winter 2018** ..... 7

**3.2 Spring 2018** ..... 9

**3.3 Summer 2018** ..... 10

**3.3.1 Summer 2018 Ocean Conditions** ..... 12

**3.4 Autumn 2018** ..... 16

**4 Conclusions** ..... 18

**5 Acknowledgements** ..... 20

**6 References** ..... 21

**7 Figures** ..... 24

**8 Tables** ..... 55

**Appendix A – Profiles and Maps** ..... 56

# LIST OF FIGURES

Figure 1. Monthly mean 2-m air temperature (°C) in 2018 over the Beaufort Sea and Amundsen Gulf.

Figure 2. Monthly 2-m air temperature anomalies (°C) in 2018 from the climatological average period 1983-2010 in the Beaufort Sea and Amundsen Gulf.

Figure 3. Monthly sea level pressure (kPa) over the Beaufort Sea and Amundsen Gulf in 2018.

Figure 4. Monthly sea level pressure anomalies (kPa) in 2018 from the climatological average period 1983-2010 in the Beaufort Sea and Amundsen Gulf.

Figure 5. Monthly mean 10-m wind speed (m $s^{-1}$) and direction in 2018 in the Beaufort Sea and Amundsen Gulf.

Figure 6. Monthly 10-m wind speed (m $s^{-1}$) and direction anomalies from the climatological average period 1983-2010 in the Beaufort Sea and Amundsen Gulf in 2019.

Figure 7. Mean monthly sea ice concentration ($10^{ths}$) for total sea ice and three stages of development (old, first-year, and young + new ice) for January, February, and March [winter] 2018.

Figure 8. Mean monthly sea ice concentration anomalies ($10^{ths}$) for total sea ice and three stages of development (old, first-year, and young + new ice) for January, February, and March [winter] 2018.

Figure 9. Mean monthly sea ice concentration ($10^{ths}$) for total sea ice and three stages of development (old, first-year, and young + new ice) for April, May, and June [spring] 2018.

Figure 10. Mean monthly sea ice concentration anomalies ($10^{ths}$) for total sea ice and three stages of development (old, first-year, and young + new ice) for April, May, and June [spring] 2018.

Figure 11. Mean monthly sea ice concentration ($10^{ths}$) for total sea ice and three stages of development (old, first-year, and young + new ice) for July, August, and September [summer] 2018.

Figure 12. Mean monthly sea ice concentration anomalies ($10^{ths}$) for total sea ice and three stages of development (old, first-year, and young + new ice) for July, August, and September [summer] 2018.

Figure 13. Mean monthly sea ice concentration ($10^{ths}$) for total sea ice and three stages of development (old, first-year, and young + new ice) for October, November, and December [autumn] 2018.

Figure 14. Mean monthly sea ice concentration anomalies ($10^{ths}$) for total sea ice and three stages of development (old, first-year, and young + new ice) for October, November, and December [autumn] 2018.

Figure 15. Monthly mean sea ice velocity (cm $s^{-1}$) and direction in 2018 in the Beaufort Sea and Amundsen Gulf.

Figure 16. Monthly sea ice velocity (cm $s^{-1}$) and direction anomalies in 2018 from the climatological mean period 1983-2010 in the Beaufort Sea and Amundsen Gulf.

Figure 17. Mean monthly sea ice-adjusted surface solar radiation downwards (J $m^{-2}$) in 2018 in the Beaufort Sea and Amundsen Gulf.

Figure 18. Monthly sea ice-adjusted surface solar radiation downwards anomalies (J $m^{-2}$) in 2019 compared to the climatological average period 1983-2010 in the Beaufort Sea and Amundsen Gulf.

Figure 19. (a) Mean accumulated sea ice-adjusted surface solar radiation downwards (J $m^{-2}$) between January and August in 2018 (inclusive), and (b) accumulated sea ice-adjusted surface solar radiation downwards anomaly (J $m^{-2}$) between January and August 2019 (inclusive) compared to the climatological average over the period 1983-2010.

Figure 20. (a) Mean accumulated sea ice-adjusted surface solar radiation downwards (J $m^{-2}$) between January and December in 2018 (inclusive), and (b) accumulated sea ice-adjusted surface solar radiation downwards anomaly (J $m^{-2}$) between January and December 2018 (inclusive) compared to the climatological average over the period 1983-2010.

Figure 21. (a) CBS-MEA CTD station and section locations in the 2018 study region, overlain on ETOPO1 bathymetry data, (b) leg 1 stations and generalized ice conditions, (c) leg 2 stations and generalized ice conditions..

Figure 22. (a) Surface temperature (°C), and (b) surface salinity at each CBS-MEA station in 2018.

Figure 23. (a) Depth of the maximum $N^2$ in meters (b) ocean heat content (kJ in a $1m^2$ column to a depth of the $N^2$ max), and (c) Freshwater anomaly (m) relative to S = 34.8, to the depth of the $N^2$ max at each CBS-MEA station in 2018.

Figure 24. Sections from west to east across Dolphin and Union Strait in 2018: salinity (a, b) and temperature (c, d). Full depth is shown in (a, c) and enlarged to show only the top 50 m in (b, d). $N^2$-derived surface layer depths at each station are denoted by white dots.

Figure 25. Sections from west to east along Minto Inlet in 2018: salinity (a, b) and temperature (c, d). Full depth (a, c) and enlarged to show only the top 50 m (b, d). $N^2$-derived surface layer depths at each station are denoted by white dots.

Figure 26. Sections from south to north across Minto Inlet in 2018: salinity (a, b) and temperature (c, d). Full depth (a, c) and enlarged to show only the top 50 m (b, d). $N^2$-derived surface layer depths at each station are denoted by white dots.

Figure 27. Sections from west to east across Darnley Bay using the Bennett Point (BPT) stations in 2018: salinity (a) and temperature (b). $N^2$-derived surface layer depths at each station are denoted by white dots.

Figure 28. Sections from west to east across Franklin Bay in 2018: salinity (a, b) and temperature (c, d). Full depth (a, c) and enlarged to show only the top 50 m (b, d). $N^2$-derived surface layer depths at each station are denoted by white dots.

Figure 29. Sections from south to north in Franklin Bay and southern Amundsen Gulf in 2018: salinity (a, b) and temperature (c, d). Full depth (a, c) and enlarged to show only the top 50 m (b, d). $N^2$-derived surface layer depths at each station are denoted by white dots.

Figure 30. Sections from south to north using the Cape Bathurst (CPB) stations in 2018: salinity (a, b) and temperature (c, d). Full depth (a, c) and enlarged to show only the top 50 m (b, d). $N^2$-derived surface layer depths at each station are denoted by white dots.

Figure 31. Sections from south to north using the Kugmallit Bay (KUG) stations in 2018: salinity (a, b) and temperature (c, d). Full depth (a, c) and enlarged to show only the top 50 m (b, d). $N^2$-derived surface layer depths at each station are denoted by white dots.

# LIST OF TABLES

Table 1. Surface and surface layer oceanographic parameters at each CBS-MEA station, August-September 2018. Freshwater content (FWC) and ocean heat content (OHC) are integrated over the surface layer depth.

# ABSTRACT

Galley, R., Niemi, A., Eert, J., Majewski, A., Friesen, M., Williams, W. 2026. Canadian Beaufort Sea - Marine Ecosystem Assessment (CBS-MEA) report on the physical system – 2018. Can. Tech. Rep. Hydrogr. Ocean Sci. 428: ix + 106 p. https://doi.org/10.60825/txnm-q171

The Beaufort Regional Environmental Assessment – Marine Fishes Project (BREA-MFP, 2012-2014), and more recently the Canadian Beaufort Sea – Marine Environmental Assessment (CBS-MEA) program (2017-present), seek to create and annually augment regional ecological knowledge, with the support and collaboration of Inuvialuit communities and the Inuvialuit Game Council. CBS-MEA integrates physical oceanography with marine food web parameters on an annual basis, with the long-term goal of characterizing interannual variability and change in the ecosystem. Conductivity-Temperature-Depth (CTD) data from 3 August to 8 September 2018 reveal the end-of-summer physical oceanographic characteristics in the region based on profiles of temperature, salinity, potential density, Brunt-Väisälä frequency squared ($N^2$), temperature-salinity plots, and temperature and salinity sections, as well as derived surface layer depth and the ocean heat content and freshwater content in the surface mixed layer at the CTD stations. We further set these oceanographic observations in the context of the annual evolution of air temperature, sea level pressure, winds, and sea ice concentration and motion in the region. Anomalously warm winter and spring air temperatures and anomalous atmospheric forcing in winter enhanced sea ice transport into the region in 2018, and contributed to significant sea ice mobility and lead presence in the Cape Bathurst flaw lead polynya system and Amundsen Gulf. Enhanced old sea ice import to the region from the north, and substantial sea ice export to the west also occurred in winter and spring as anticyclonic conditions persisted in the region. In summer, pressure changes created northwesterly ice motion, driving old ice southward and into the mouth of Amundsen Gulf. Sea ice in the region affected the amount of surface solar radiation downward available to heat the ocean surface over the annual cycle. In autumn, a return to anticyclonic sea ice motion continued to import ice from the north and export to the west at higher-than-average velocities, creating conditions for substantial and anomalous new-plus-young sea ice formation in October, November and December.

# RÉSUMÉ

Galley, R., Niemi, A., Eert, J., Majewski, A., Friesen, M., Williams, W. 2026. Canadian Beaufort Sea - Marine Ecosystem Assessment (CBS-MEA) report on the physical system – 2018. Can. Tech. Rep. Hydrogr. Ocean Sci. 428: ix + 106 p. https://doi.org/10.60825/txnm-q171

Le projet d'évaluation environnementale régionale de la mer de Beaufort – Poissons marins (BREA-MFP, 2012-2014) et, plus récemment, le programme canadien d'évaluation de l'environnement marin de la mer de Beaufort (CBS-MEA) (depuis 2017) visent à développer et à enrichir chaque année les connaissances écologiques régionales, avec le soutien et la collaboration des communautés inuvialuites et du Conseil inuvialuit du gibier. Le programme CBS-MEA intègre chaque année des données d'océanographie physique aux paramètres du réseau trophique marin, dans le but à long terme de caractériser la variabilité interannuelle et les changements au sein de l'écosystème. Les données CTD (conductivité, température, profondeur) recueillies du 3 août au 8 septembre 2018 révèlent les caractéristiques océanographiques physiques de fin d'été dans la région, sur la base de profils de température, de salinité, de densité potentielle, de la fréquence de Brunt-Väisälä au carré (N2), des diagrammes température-salinité et des coupes de température et de salinité, ainsi que de la profondeur de la couche de surface dérivée et du contenu thermique et en eau douce de la couche de mélange superficielle aux stations CTD. Nous avons également replacé ces observations océanographiques dans le contexte de l'évolution annuelle de la température de l'air, de la pression au niveau de la mer, des vents, ainsi que de la concentration et du mouvement de la glace de mer dans la région. Des températures de l'air anormalement chaudes en hiver et au printemps, ainsi qu'un forçage atmosphérique anormal en hiver, ont favorisé le transport de glace de mer vers la région en 2018 et ont contribué à une mobilité importante de la glace de mer et à la présence de chenaux dans le système de polynie de Cape Bathurst et dans le golfe d'Amundsen. Un afflux accru de glace de mer ancienne vers la région en provenance du nord, ainsi qu'une exportation importante de glace de mer vers l'ouest, ont également été observés en hiver et au printemps, alors que des conditions anticycloniques persistaient dans la région. En été, les variations de pression ont généré un mouvement de la glace vers le nord-ouest, poussant la glace ancienne vers le sud et vers l'embouchure du golfe d'Amundsen. La glace de mer présente dans la région a influencé la quantité de rayonnement solaire de surface disponible pour réchauffer la surface de l'océan au cours du cycle annuel. À l'automne, le retour à un mouvement anticyclonique de la banquise a continué à favoriser l'importation de glace depuis le nord et son exportation vers l'ouest à des vitesses supérieures à la moyenne, créant ainsi les conditions propices à une formation importante et anormale de glace de mer nouvelle et jeune en octobre, novembre et décembre.

## 1 Introduction

In 2018 in the northern hemisphere, Arctic amplification continued in earnest. Surface air temperatures continued to warm at twice the rate as warming occurring over the rest of the earth. 2018 was the second warmest year on record in the Arctic to that point since 1900 (+1.7°C relative to the 1981-2010 climatological average) (Osborne et al., 2018).

Winter maximum Arctic sea ice extent in March 2018 was the second lowest to that point in the climatological satellite record (since 1979), and all 12 of the lowest winter maximum sea ice extents occurred in the 12 years ending in 2018 (Perovich et al., 2018). The summer (September) sea ice extent in 2018 was the sixth lowest to that point in the satellite record (Perovich et al., 2018). The oldest, thickest sea ice extent in the northern hemisphere had declined to 0.13 million $km^2$ in 2018, a 95% reduction since 1985 (Perovich et al., 2018). First-year sea ice dominated the ice cover, comprising 77% of the March 2018 ice pack (Perovich et al., 2018). In addition to the sea ice conditions in the Canadian Beaufort Sea and Amundsen Gulf, sea ice conditions and processes in Fram Strait, the Barents Sea and the Bering Sea were of particular interest in 2018 as part of the hemispherical evolution of the Arctic marine environment through the annual cycle.

An unprecedented decline in Arctic sea ice outflow through Fram Strait (between Greenland and Svalbard) was observed in 2018 through an analysis of a combination of ice thickness measurements from upward looking sonar and remote sensing observations (Sumata et al., 2022). The reduction of sea ice volume export from the Arctic to the north Atlantic through Fram Strait was found to be nearly 60% relative to the 2000-2017 average, and 75% compared to the 1990s average (Sumata et al., 2022). Using a combination of backward trajectories of ice floes, remote sensing products, and atmospheric reanalysis data, Sumata et al. (2022) showed that anomalously warm atmospheric conditions upstream of Fram Strait in the preceding winter months could not have caused the observed thinning/depletion. However, sea ice stayed north of Fram Strait for roughly three months prior to its arrival at the Strait in an area characterized by strong oceanic heat supply to the sea ice from Atlantic Water. The sea ice was stagnant in this area as a result of anomalous sea level pressure in early 2018 created by a high atmospheric pressure center in the Barents Sea and a low atmospheric pressure center over the Canadian Arctic Archipelago and Greenland which produced southerly winds that slowed and even stopped sea ice motion in Fram Strait (Sumata et al, 2022). Sumata et al. (2022) also indicate that southerly winds brought warm air masses to the area north of Fram Strait, leading to reduced ice growth in the first months of 2018.

By 2018 the a*tlantification* of the Barents Sea (Barton et al., 2018) was long-underway – a positive feedback that had reduced the sea ice extent in the Barents Sea compared to the climatological average in almost every month of every year between 2004 and 2018 (except autumn 2014). Reduced sea ice extent in the Barents Sea leads to warm sea surface temperatures, which allows for inflow of warm, salty Atlantic Water to the region and more specifically to the surface. The replacement of relatively cold, fresh Arctic Water at the surface with warmer, saltier water reduces the density gradient that used to protect the surface from the Atlantic Water layer in the Barents Sea.

In the Bering Sea, the winter of 2017-2018 saw the lowest winter-maximum sea-ice coverage recorded between 1980 and 2019. Throughout almost the entire winter, ice extent remained at record lows, dropping to less than 40% of the historical average. Stabeno and Bell (2019) indicate that warm winds blowing from the south in November delayed sea ice freeze up in the Bering Sea, and although sea ice did form in the first months of 2018, it was relatively thin. A sudden shift to strong, warm southerly winds in February and March drove the ice back north and caused a massive retreat (Stabeno and Bell, 2019). This harkens back to the earlier work of Woodgate et al. (2010) that showed significant oceanic heat transport from the Pacific north through the narrow, shallow Bering Strait into the western Arctic reduced the sea ice concentration and volume in the Chukchi Sea. 2017 was the warmest the Pacific Ocean had been to that point in the absence of an El Niño (NOAA, 2018) which limited the presence of ice in the Bering Sea and lowered sea ice concentrations in the Chukchi Sea over winter 2017-2018 (NSIDC, 2026, Perovich et al., 2018, Wang et al., 2021). Massive reductions in sea ice in the Bering Sea also caused the cold pool, an area of bottom water below 2°C on the Bering Sea shelf, to shrink to its smallest size on record by August 2018. Sea ice onset timing has downstream ecosystem effects extending beyond the physical oceanographic system; it influences the timing of spring phytoplankton blooms, zooplankton abundance and the survival of young pollock (Stabeno and Bell, 2019). It also impacts humans by changing their ability to travel and hunting on/from sea ice, as well as reducing coastal protection from wave action (Stabeno and Bell, 2019).

Since the middle of the 2000s, substantial multiyear sea ice loss has been observed in the Canada Basin (Bailey and Timmermans, 2025) and more specifically in the Beaufort Sea (Galley et al., 2016). Over the long-term (1979-2023), trends in sea ice volume in the Canada Basin have been dominated by thermodynamics, as opposed to sea ice motion (Bailey and Timmermans, 2025). The sea ice-albedo positive feedback creates a loop where reduced sea ice concentration, especially in July and August, allow for increased sea surface temperatures, which reduce the thickness of the sea ice grown the following

winter, which in turn allow for increased open water areas in summer that absorb more solar insolation. Within this long-term trend toward thermodynamically reduced sea ice volume, 2018 experienced massive winter MYI loss in the Beaufort (285 000 $km^2$), similar to the amount of multiyear sea ice exported from the Arctic through Fram Strait (Babb et al., 2022). High western export from the Beaufort Sea in winter 2018 (Babb et al., 2022) was likely amplified by reduced concentrations downstream in the Chukchi Sea, which created space for sea ice from the Beaufort to move to as regional and hemispheric processes redistribute sea ice from the central Arctic pack through the Beaufort Sea before the sea ice is typically re-circulated into the eastern Arctic.

Fisheries and Oceans Canada (DFO) continues to help marine ecosystem-based approaches to marine measures (including spill response planning) and resource management through comprehensive assessment of the biology and habitats of the Beaufort Sea and Amundsen Gulf in the Inuvialuit Settlement Region. The Canadian Beaufort Sea – Marine Ecosystem Assessment (CBS-MEA) program (2017-present), seeks to provide an increasingly complete understanding of spatial and temporal processes affecting and controlling the regional ecosystem, following on from the Beaufort Regional Environmental Assessment - Marine Fishes Project (BREA-MFP) in 2012-2014 and earlier ArcticNet work in the region. The CBS-MEA program pursues understanding of linkages within the regional physical system, as well as physical-biological linkages inter-annually and in the long-term, and provides information relevant to the six Inuvialuit Settlement Region communities in the area, including variables related to elements of the regional marine food web, from phytoplankton to belugas and bowhead whales.

Here we present atmospheric and sea ice information over an annual cycle to provide context for physical oceanographic observations recorded in August and September 2018. We explain basic physical forcing and processes over one year in a study region that broadly encompasses the Canadian Beaufort Sea, the Mackenzie Shelf, and Amundsen Gulf (-145°E to -110°E, 68°N to 75°N). The study region includes water of the Inuvialuit Settlement Region, and the Anguniaqvia niqiqyuma (Niemi et al., 2020) and Tarium Niryutait (DFO, 2010) Marine Protected Areas (MPAs), as well as a number of ecologically and biologically significant areas (EBSAs, e.g. DFO, 2014), and the Cape Bathurst Flaw Lead Polynya Complex (see Stirling, 1980).

## 2 Data and Methods

This assessment of atmospheric, sea ice, and oceanographic conditions in the Inuvialuit Settlement Region during 2018 includes air temperature, sea level pressure, winds, and solar radiation at the ocean surface

using reanalysis products, remotely sensed sea ice concentration and motion, and data from ship-based oceanographic sampling. Climatological averages (1983-2010) have been calculated to determine anomalies for the conditions in 2018. CTD data collected between 3 August and 8 September 2018 are used to elucidate the surface salinity and temperature and the thickness of the ocean surface layer at sampling stations. The freshwater content and ocean heat content in the surface layer are calculated. Finally, cross-sectional oceanographic plots are presented in areas of the study region using CTD data.

### 2.1 Environmental Forcing

European Centre for Medium-range Weather Forecasts (ECMWF) Reanalysis v5 (ERA5) 2 m air temperature, sea level pressure, 10 m U- and V- winds, and surface solar radiation downwards (SSRD) data at six-hourly intervals from January 1, 1983 to December 31, 2021 (Hersbach et al., 2018) were obtained from the Copernicus Climate Change Service Climate Data Store (https://cds.climate.copernicus.eu/cdsapp#!/dataset/reanalysis-era5-pressure-levels?tab=overview). Monthly averaged 2-m air temperature, sea level pressure, and 10-m wind speed and direction were created for each of the 4089 grid cells in the study region for each month of 39 years (1983-2021) including 2018 presented here. Monthly climatological standard normals (i.e. averages) for 2-m air temperature, sea level pressure, 10-m winds were produced from all the available data in each month in 1983-2010 (28 years; note we use 28 for this period beginning in 1983 in order to maintain consistency with the sea ice data which begins in 1983). Monthly anomalies in 2018 were calculated using the monthly climatological standard normal, for example:

$$T_{a\ anomaly} = T_a - T_{a\ clim} \quad (1)$$

Where $T_{a\ anomaly}$ is the air temperature anomaly in a month in 2018, $T_a$ is the average air temperature in a month in 2018, and $T_{a\ clim}$ is the climatological average air temperature (1983-2010) for the month. Positive anomalies occur when the monthly average air temperature is greater than the climatological standard normal for that month; negative anomalies occur when the monthly average is less than the climatological standard normal for the month.

### 2.2 Sea Ice Concentration and Motion

Average sea ice concentration maps for each month between 1983 and 2021 were created by downloading and gridding regional Canadian Ice Service (CIS) digital archive data for the western Arctic (https://iceweb1.cis.ec.gc.ca/Archive/page1.xhtml?lang=en) at 1 km resolution on the CIS Lambert

conformal conic projection. Analysis of the CIS data began in 1983 because the CIS data is broken down by consistent source data and preparation method eras, and the quality index prior to 1983 is reduced (please see Tivy et al., 2011 for detailed information on the CIS data quality indices). Using all the available CIS charts in each month in each year, the monthly mean total sea ice concentration (in tenths) and mean partial concentrations (in tenths) for old ice (superset of multiyear and second-year ice), first-year sea ice, and new-plus-young sea ice (< 30 cm thick, Fequet, 2005) stages of development were computed at 1 km resolution. Monthly climatological averages for total sea ice concentration as well as old sea ice, first-year sea ice, and new-plus-young sea ice were calculated by averaging all the data each month between 1983 and 2010 (inclusive). Monthly concentration anomalies in 2019 for total, old, first-year, and new-plus-young ice concentrations were created by subtracting the months' climatological (1983-2010) average sea ice concentration from the corresponding monthly average concentration for each stage of development. Positive sea ice anomalies occur when the monthly average concentration is greater than the climatological standard normal (1983-2010) in that month.

Monthly average sea ice velocity and direction in the Beaufort Sea from 1983 to 2021 were calculated from the National Snow and Ice Data Centre Polar Pathfinder Daily 25 km EASE-grid sea ice motion vector data (Version 4) for the northern hemisphere, freely available at https://nsidc.org/data/NSIDC-0116 (Tschudi et al., 2019). Climatological monthly averages for each month were created using the u- and v-vector components for each month between 1983 and 2010 (inclusive). Monthly anomalies for 2018 were created by subtracting the monthly climatological standard normal u- and v- components of the sea ice motion from the monthly average sea ice motion u- and v- components each year.

**2.3 Sea ice-adjusted Surface Solar Radiation Downwards**

ECMWF ERA5 surface solar radiation downwards (SSRD, in J $m^{-2}$) data were also downloaded from the Copernicus Climate Change Service Climate Data Store at six-hourly intervals between 1983 and 2021 (inclusive). SSRD is the amount of shortwave radiation (including both diffuse and direct radiation) that reaches a horizontal plane at the surface of the earth; it is the model equivalent of the shortwave radiation a pyranometer would measure at the surface. For the purposes of this work, SSRD may be thought of as light energy from the sun that may be converted to heat energy if it is absorbed by the surface of the ocean, either melting surrounding sea ice, or contributing to increased water temperatures. The SSRD must be adjusted for sea ice cover to approximate the amount of solar radiation incident on the ocean surface in the Arctic marine environment. In each month of each year between 1983-2021, the CIS monthly mean total sea ice concentration grid was downscaled to the ERA5 grid resolution, divided by 10

to obtain a fractional coverage, and then subtracted from unity to obtain the monthly fractional open water area in each grid cell. The fractional open water area in a month was multiplied by the mean SSRD for the month in each SSRD grid cell to obtain the sea-ice adjusted SSRD (J $m^{-2}$) incident on the ocean surface in each grid cell. Monthly climatological averages over the period 1983-2010 were calculated using the sea ice-adjusted monthly SSRD means, and monthly anomalies of sea ice-adjusted SSRD were calculated for each month in each year between 1983 and 2021.

**2.4 CBS-MEA sampling**

Physical oceanographic sampling during CBS-MEA (3 August-8 September 2018) was undertaken from *FV Frosti* at stations across the shelf break north of Kugmallit Bay and the Tuktoyaktuk Peninsula, east of Cape Bathurst, in Franklin and Darnley Bays, across Dolphin and Union Strait, and in Minto Inlet on western Victoria Island. Conductivity, temperature, and depth (CTD) measurements were made using a Seabird SBE 911plus deployed as part of the CTD-Rosette system. Average salinity (PSS-78) and temperature (ITS-90, °C) over 1 decibar (approximately one meter) increments were output after the CTD data underwent quality control (bottle salinity samples were collected with the rosette and used as part of data quality assurance and control processes, and salinity is considered to be accurate within ±0.003). An altimeter was employed for water depth measurements, and the noted depth at each station was the median of the deepest two meters recorded. In the absence of altimetric measurements at a station, the deepest depth measured by the CTD was used.

Potential density referenced to the surface ((σ, θ), minus 1000 kg $m^{-3}$) and $N^2$ (the square of the buoyancy frequency, ($s^{-2}$)), were calculated for each depth using the OCE package (Kelley, 2018) for R (R Core Team, 2022). The topmost surface value of temperature and salinity at each station in 2018 was mapped. The depth of maximum $N^2$ was identified in each profile, and that value was used to connote the bottom of the surface layer of the ocean column. The $N^2$-maximum surface layer depth at each station was used to integrate the total freshwater content (FWC, in meters) and the total ocean heat content (OHC, in kilojoules), in a 1 $m^2$ column of water to the depth of the surface layer. The FWC was calculated at each decibar depth interval of the column specified by the maximum $N^2$ depth:

$$FWC = \frac{S_o - S}{S_o} \qquad (2)$$

where $S_o$ is the reference salinity of 34.8, and $S$ is the salinity at each depth interval and the FWC at each depth were summed. The OHC relative to 0°C was calculated at each decibar depth interval of the column specified by the maximum $N^2$ depth:

$$OHC = c_{sw} \times \rho \times \Theta \quad (3)$$

where $c_{sw}$ is the specific heat capacity of seawater (set to 4 kJ $kg^{-1}K^{-1}$ for the observed temperature and salinity ranges after Sharqawy et al., 2010), ρ is seawater density (kg $m^{-3}$) calculated using absolute salinity and conservative temperature, and Θ is conservative temperature (°C). The OHC at each depth interval in the surface layer was then summed.

## 3 Results and Discussion

Air temperature, sea level pressure (SLP), wind, sea ice concentration and motion, and sea-ice-adjusted surface solar radiation downward (SSRD) results and discussion are presented by season with winter (January February, March), spring (April, May, June), and summer (July, August, September), summarizing key processes and physical drivers prior to and during the CBS-MEA cruise, 3 August - 8 September 2018. Finally, autumn (October, November, December) conditions are presented to provide the full annual perspective of temperature, SLP, sea ice concentration and motion, and solar radiation during freeze up and consolidation of the ice pack.

### 3.1 Winter 2018

In January, February, and March 2018 air temperature over the marine portion of the study area was warmer than -25°C, surrounded by colder terrestrial areas (Figure 1). The 2-m air temperature anomalies for January, February and March 2018 indicate the region was much warmer than the climatological average (1983-2010) in all three winter months (Figure 2). Winter in the region is typically characterized by low sea level pressure (SLP) in the southwest as one advances towards the Aleutian Low, and high SLP in the northwest (i.e. the Beaufort High), and high SLP over the north continental coast. In January and February 2018, high SLP resided over the continental land mass to the south of the marine region, while lower SLP occurred in Viscount Melville Sound north of Victoria Island (Figure 3). Compared to the climatology (1983-2010), SLP over the entire region was higher than average in January and February (Figure 4). In March, the SLP pattern shifted, and the Beaufort High was observed in its more typical location northwest of Banks Island (Figure 3). Owing to the SLP pattern in the winter months, the wind speed and direction in January, February, and March 2018 (Figure 5) departed slightly from the

climatological average (Figure 6). Reversal in the wind direction to anticyclonic, and therefore export-friendly winds (Figure 5) occurred in March 2018 with the return of the Beaufort High (Figure 3).

In winter 2018 the study region was completely covered with mobile sea ice, with almost no landfast sea ice (10/10ths total sea ice concentration) in the ice chart averages for January, February and March (Figure 7, top panels). Further, evidence of reduced sea ice concentration exists in the western Mackenzie delta area in January (Figure 7, 8), and Amundsen Gulf and much of M'Clure Strait as the sea ice in those areas remained mobile all winter. As winter progressed, the proportion of old sea ice increased in the region by import from the north (Figure 7), which showed up as the increasing spatial extent of positive old ice anomalies (Figure 8), while high proportions of the total sea ice concentration were made up of first-year sea ice and new-plus-young sea ice in the southern half of the Beaufort Sea, in M'Clure Strait, and in Amundsen Gulf (Figure 7). New-plus-young sea ice (< 30 cm thick), represents divergence in the regional sea ice cover in winter, and largely delineates the Cape Bathurst Flaw Lead Polynya complex (Figure 7). Despite cold winter air temperatures, the Cape Bathurst flaw lead polynya complex contained anomalously high concentrations of new-plus-young sea ice in all three winter months (Figure 8), indicating the consistency of dynamic removal (divergence) of sea ice from the flaw lead polynya in 2018.

Winter sea ice motion in the study region (Figure 15) was anomalous in all three months (January, February and March) 2018 (Figure 16). In January and March, the regional SLP pattern, and more specifically the position of the Beaufort High, along with reduced sea ice concentrations downstream in the Bering and Chukchi Sea created anomalous, high velocity anticyclonic sea ice motion (Figure 15, 16). Anticyclonic sea ice motion in the study region is important as it allows for the export of sea ice out of the region to the western Beaufort Sea and eventually the Chukchi Sea, as well as old ice re-supply (import) to the region from the north along the west coast of the Canadian Arctic Archipelago. Critically for the biological system, this anticyclonic sea ice motion created and maintained a convincing Cape Bathurst flaw lead polynya complex in both January and March (Figure 7). In March 2018, sea ice export from M'Clure Strait actually produced positive sea-ice adjusted SSRD (Figure 17) anomalies (Figure 18) in that area. In contrast, and very instructive of the end-ranges of the sea ice system in the region, February 2018 exhibited sea ice motion from the northwest across the study region directed into Amundsen Gulf and onto the Mackenzie Shelf (Figure 15, 16) due to the anomalous nature of the mean SLP field over the region during February (Figure 3, 4). Arguably this kept sea ice within Amundsen Gulf mobile (Figure 7) due to convergence in the region (rather than by divergence in January and March) while also limiting the occurrence of new-plus-young sea ice to the southern coasts of Banks Island, moving sea ice away from the lee of Banks Island given the sea ice motion direction in the region (Figure 7).

### 3.2 Spring 2018

The study region warmed in spring (April-June) 2018 (Figure 1), and April and May air temperatures were warmer than climatological averages for those months (Figure 2). In June, the marine areas of the study region warmed very little compared to May (Figure 1) and June was largely cooler than average save for a band of slightly warmer than average air over the shelf and western Amundsen Gulf (Figure 2). In April, and to a lesser extent in May 2018, a ridge of high pressure extended from the Beaufort High in the Canada Basin with lower pressure over the Brooks Range and northeast Alaska (Figure 3). As a result of the strength and position of the Beaufort High in April, and to a lesser extent in May, the wind speed and direction was anticyclonic over the marine region (Figure 5). In April, the wind speed was higher than average (Figure 6) while in May the wind speed was close to the climatological average (Figure 6). In June, the high-pressure center shifted south (Figure 3) and was reduced in strength compared to the climatological average for that month (Figure 4). The position of the high-pressure center in June (Figure 4) slowed the wind speed in the south half of the region, and increased it in the north half of the region compared to the long-term average (Figure 6). The June wind direction was largely westward, with the exception of east winds in eastern Amundsen Gulf (Figure 5).

The regional sea ice cover was complete in April 2018 with the mobile sea ice clearly delineable from the landfast (10/10ths) sea ice in the region (Figure 9). Beyond the landfast ice, the regional sea ice had now remained mobile for four months in a row. The sea ice motion in April was congruous where positively anomalous sea ice motion velocities (figure 15, 16), especially across the Mackenzie Delta, indicated anticyclonic sea ice motion west out of the study region while simultaneously showing sea ice import from the north. New-plus-young ice was present in April on the Mackenzie Shelf along the landfast sea ice edge, north of Cape Bathurst, and along the southwest coast of Banks Island (Figure 9). Very small sea ice adjusted SSRD anomalies in April 2018 (Figures 17, 18), positive in Amundsen Gulf and M'Clure Strait, and negative in the flaw lead areas along the Mackenzie Shelf and western Banks Island. In May 2018, the Cape Bathurst flaw lead polynya complex began to reappear in the monthly mean total sea ice concentration (Figure 9), when air and water temperatures promoted formation of new-plus-young sea ice in the flaw lead polynya region (Figure 9) which were observed to be positively anomalous (Figure 10). Continuing from April, sea ice motion in May 2018 was even more strongly anticyclonic, moving sea ice out of the region westward while importing sea ice from the north (Figure 15, 16). In May, positively anomalous sea ice-adjusted SSRD were observed within the Cape Bathurst flaw lead along the continental coast west of Cape Bathurst and along the southern coast of Banks Island, along with western Amundsen Gulf (Figure 7, 18) due to divergence created by the ice motion regime. In June, the total sea ice

concentration indicated the further opening of the Cape Bathurst flaw lead polynya complex (Figure 9) as a result of continued anticyclonic sea ice motion (Figure 15) at higher velocities than the climatological average for the month (Figure 16). This resulted in substantial sea ice-adjusted SSRD in the whole of the polynya complex (Figure 17) which was greater than the climatological average for June (Figure 18). In all three spring months, opposing anomalies in both the old sea ice and first-year sea ice concentration were observed (Figure 10) as the total sea ice concentration remained high.

**3.3 Summer 2018**

The July and August 2018 2-m air temperatures over the study region are similar in magnitude and spatially consistent, with cool temperatures coincident with the highest sea ice concentrations, warmer marine area in the absence of sea ice, and the warmest temperatures over terrestrial areas (Figure 1). Much of the marine region experienced positively anomalous 2-m air temperatures in July, August and September 2018 (Figure 2). The general mean SLP pattern over the study region in summer 2018 was that of higher pressure in the north, and lower pressure in the south (Figure 3). In July, the high SLP was northwest and northeast of the study region, and the isobars indicated zonal flow, while in August anomalously high SLP was east of the study domain (Figure 4), resulting in August isobars indicating a combination of zonal flow along the Mackenzie shelf, and meridional flow at the eastern edge of the study region (Figure 3). In September 2018, the high SLP pattern returned to zonal flow (Figure 3) with the highest SLP center over M'Clure Strait, while low SLP occurred over the continental landmass (Figure 3). The mean wind velocities in July and August 2018 (Figure 5) were not much different than the climatological averages for those months (Figure 6); the July and August mean wind direction was largely northerly (Figure 5). In September, the wind direction switched to a more export-favorable easterly direction across Amundsen Gulf with northeasterly winds in the Beaufort Sea (Figure 5). Easterly winds across Amundsen Gulf were anomalous for the month of September (Figure 6).

Regional sea ice break-up continued, and melt occurred in summer 2018 (Figure 11), but anomalously high total sea ice concentrations were present in the mouth of M'Clure Strait, along the western coast of Banks Island, at the mouth of Amundsen Gulf (Figure 12). In July, eastern Amundsen Gulf was anomalously all but ice-free while higher than average concentrations of old ice extended down the west coast of the archipelago and Banks Island blocking the mouth of Amundsen Gulf, and extended west along the Mackenzie shelf (Figure 11, 12). Sea ice motion in the region (Figure 15) was congruous, roughly zonal at above-average velocity (Figure 16) toward the west coast of Banks Island and Amundsen Gulf. Higher than average first-year sea ice concentrations occurred in M'Clure Strait and along the west coast of Banks

Island, while lower than average concentrations of first-year ice were coincident with high old ice concentrations along the Mackenzie shelf. The sea ice concentrations by stage of development and their anomalies were reflected in the July mean sea ice-adjusted SSRD in the region (Figure 17, 18). More than average sea ice-adjusted SSRD was incident on the ocean surface in eastern Amundsen Gulf in July, less than average was incident on the ocean surface along the continental coast west of Cape Bathurst, and much less than average occurred west of Banks Island (Figure 17, 18). In August, positive total sea ice concentration anomalies were composed entirely of positive old sea ice anomalies imported from the north along the west coast of the archipelago (Figure 15) at faster than average velocities (Figure 16). Negative total sea ice concentration anomalies in the western part of the study region were composed of a combination of negative old ice and negative first-year ice anomalies (Figure 11, 12) likely driven by a combination of melt and sea ice export out of the area west to the Chukchi Sea (Figure 15, 16). Much more first-year sea ice than average remained in eastern M'Clure Strait in August 2018 (Figure 12) having been pushed into M'Clure during winter 2018 (Figure 8). Moving away from the summer solstice in June, the sea ice-adjusted SSRD in August showed a decline from the previous two months (Figure 17). However, due to missing sea ice in the Beaufort Sea (Figure 11, 12), sea ice-adjusted SSRD was positively anomalous in the Canada Basin, and negatively anomalous along the coast of Banks Island (Figure 18) due to sea ice imported in August (Figure 11, 15). In September 2018, import-favorable sea ice motion continued at velocities much higher than average from the north (Figure 15, 16) and the total, old and first-year sea ice concentrations remained very similar to those of August (Figure 11), as did their respective anomaly maps (Figure 12). Because the September total sea ice concentrations and anomalies remained consistent from August, the September sea ice-adjusted SSRD anomalies were also similar to August, albeit with less total sea ice-adjusted SSRD (Figure 17) later in the year. New-plus-young sea ice was present around the periphery of the sea ice pack in September 2018 (Figure 11), at positively anomalous concentrations (Figure 12). In September, the high concentration ice pack in the region was in general control of both the 2-m air temperature (Figure 1) and the water temperature, keeping both around the freezing point and allowing for new and young ice production within the pack and around the periphery (Figure 11, 12).

To relate some indication of the potential for solar energy accumulation in the ocean surface prior to and during the physical oceanographic observations at the end of summer 2018, the (i) mean sea ice-adjusted SSRD in each month in 2018 from January to August (Figure 19a) and (ii) the anomaly of the accumulated sea ice-adjusted SSRD compared to the 1983-2010 period (Figure 19b) were calculated for each grid cell in the study region. Prior to September 2018, open water in the Beaufort Sea, in the southern arm of the Cape Bathurst flaw lead polynya complex, and the whole of Amundsen Gulf had the opportunity to

accumulate substantial amounts of solar energy (Figure 19a), melting sea ice or heating the upper ocean mixed layer which were greater than the long-term average (Figure 19b). Much of this solar energy was received by the ocean surface in June, July and August 2018 (Figure 17). However, these sea ice-adjusted SSRD accumulation results for the Jan-Aug 2018 period (Figure 19a) also indicate that the ocean surface west of Banks Island and in western Amundsen Gulf received less than the climatological amount of solar energy between January and August 2018 (Figure 19b). Ocean heat must be lost in the fall before ice formation can commence, which may delay the onset of freeze-up regionally, and may lead to thinner end-of-winter sea ice thickness the following spring.

### 3.3.1 Summer 2018 Ocean Conditions

Oceanographic sampling at the end of summer 2018 (3 August - 8 September) occurred at 51 stations in the study region (Figure 21, Table 1, Appendix A). The positive total sea ice concentration anomalies in August due to old ice influx from the north along Banks Island caused some planned stations to be inaccessible and cut off access to Darnley Bay where the crew change was expected to occur (Figure 21b, 21c). Sea ice on the Mackenzie Shelf and in Amundsen Gulf constrained sampling to stations <350 m in 2018 and priority stations (i.e., CPB1-6) usually sampled at the start of the cruise could not be accessed until the end of August after the ice had shifted offshore (Figure 21b, 21c). Opportunistic ice edge sampling was added which included areas where bowhead feeding had been observed. The surface temperature of the ocean is plotted for each station in Figure 22a, the surface salinity of the ocean at each station is plotted in Figure 22b. On-shelf stations KUG-01 and DAL-01 had the highest sea surface temperatures and the lowest sea surface salinity observed; likely riverine influence at those locations had an effect (Figure 22) rather than ice melt, which would have maintained sea surface temperatures at the freezing point coincident with reduced surface salinity. Warm ocean surface temperatures and high salinity was observed in the eastern end of the study region in Dolphin and Union Strait and Minto Inlet, while cooler surface temperatures and surface salinities in the mid-20s were found in Darnley Bay, Franklin Bay, and nearer the Mackenzie shelf break (Figure 22, Table 1). The mean sea surface temperature in the region in 2018 was 3.33 °C (standard deviation = 1.97). The mean surface salinity in 2018 was 24.51, (standard deviation = 3.26). Appendix A contains profile plots of salinity, temperature, potential density and $N^2$, along with T-S plots and locations for each of the stations in 2018.

The surface layer depth (the depth of the $N^2$ maximum) in the study region was variable at the end of summer 2018, ranging between 1.4 m near at the west end of Dolphin and Union Strait and adjacent to Cape Perry to 39 m at the south end of Franklin Bay (Figure 23a) (mean = 13.9 m, standard deviation =

10.2 m). Unsurprisingly, the stations with the thinnest surface layers contained the least ocean heat content in 2018 (Figure 23b, Table 1). The greatest ocean heat content in the defined surface layer, 458 kJ, occurred in Franklin Bay at FKN_01 where the surface layer was the thickest (36 m, Figure 23a, b, Table 1). The mean ocean heat content in the $N^2$-defined surface layer in the region in 2018 was 145 kJ, with a standard deviation of 132 kJ. The surface layer ocean heat content is important because that is the amount of heat the ocean must lose to the atmosphere prior to ice formation in the autumn, substantially affecting freeze-up timing and end-of-winter sea ice thickness in the following spring. Stations CPB_02 contained the least amount of freshwater in the defined surface layer (0.11 m, Figure 23c, Table 1) while FKN_07 contained the greatest freshwater content (12.5 m) in the defined surface layer (Figure 23c, Table 1), due to riverine influence and sea ice melt. The mean freshwater content in the defined surface layer in 2018 in the region was 3.44 m, with a standard deviation of 2.91 m.

Salinity and temperature across Dolphin and Union Strait (DUS) from west to east are presented in section view in Figure 24 for the full depth (Figure 24a, c) and for the top 50 m (Figure 24b, d). The mean $N^2$-defined surface layer across Dolphin and Union Strait is 11.7 m, though it is shallower at the continental coast (10 m at DUS_02) and deeper nearer Victoria Island (20 m at DUS_09). In the full depth section (Figure 24a, c), the summer surface mixed layer overlies Pacific Water (salinity 31 to 33.5), which overlies water of Atlantic origin (salinity > 33.8). Upon closer inspection of the near-surface (<50-m deep) waters (Figure 24 b, d), the surface layer was between 4-6 °C with a salinity around 29. The warm, fresh water at the surface is thickest near the coast of Victoria Island and thinnest at the continental coast, which may be due to local southwesterly winds prior to and/or during the oceanographic survey of the area.

In Minto Inlet, six stations (MTI_01, MTI_02, MTI_04, MTI_HC0, MTI_06, and MTI_07) composed a west-to-east section (Figure 25). The $N^2$-derived surface layer thickness ranged from 34 m on the west end to 12 m at the east end (Figure 25, Table 1). The $N^2$-derived surface layer thickness may be inaccurate at MTI_04 in the middle of the Inlet to due to the fact that the $N^2$ value is highest at the surface (the salinity increases rapidly with depth from the surface, and the temperature decreases rapidly with depth from the surface (see Appendix A page 69 for MTI_04 cast plot). In section view (W-E, Figure 25), the salinity and temperature indicate warm, low salinity water at the surface nearest Victoria Island which seems to spread thinly out towards the mouth on the Inlet, as well as mix downward in the water column. Four stations (MTI_05, MTI_04, MTI_03, BIN_01) composed a south-to-north section in Minto Inlet in 2018 (Figure 26). The $N^2$-derived surface layer thickness was 22 m at the south end of the section, thinning to 13 m at the north end at BIN_01 (Figure 26, Table 1). The surface mixed layer was fresher and warmer

and thicker in the south, and thinned, became more saline, and cooled at BIN_01 at the north end of the section (Figure 26). CTD data in Minto Inlet are presented with the caveat that some surface data are missing due to quality control/quality assurance (Figure 25, 26, profiles in Appendix A), which has created inaccuracies in the $N^2$-derived surface layer depths, which also affects the freshwater and ocean heat content calculations for the surface layer. Despite this limitation, it is obvious that Minto Inlet contained substantial heat down to 15-20 m depth that was relatively evenly distributed from south to north (Figure 26d) and contained some freshwater at the surface (salinity ~ 24) in the middle of the section (Figure 26b).

In Darnley Bay, there were three Bennett Point (BPT) stations sampled in 2018 (Figure 21) where the $N^2$-derived surface layer was 14-15 m thick at the western two stations, and 31 m thick at BPT_05 in the east (Figure 27). From west to east, the lower salinity surface layer (salinity ~24) thinned slightly in Darnley Bay before deepening substantially near the eastern coast (Figure 27). The high temperature surface layer (4 °C) was strongly stratified from cooler Pacific water below (0 °C) in the western half of Darnley Bay. The section across Darnley Bay cooled, became less strongly stratified, and deepened as the section approached the east coast (Figure 27).

In Franklin Bay, six stations (FKN_01 to FKN_06) were used to create a west-to-east oceanographic section (Figure 28). At the west end of the section (FKN_01), the $N^2$-derived surface layer was deepest (36 m), composed of relatively fresh, warm water (Figure 28). We note the likelihood of Horton River influence at this station (see Appendix one FKN_01 for cast profile). Moving eastward across Franklin Bay, the $N^2$-derived surface layer thinned gradually to 5 m at FKN_06 nearest Cape Parry (Table 1), and the fresh, warm surface water volume decreased eastward (Figure 28). The freshwater content in the surface layer decreased from west to east decreased across Franklin Bay from 12.4 m at FKN_01 to 1.6 m at FKN_06 (Table 1). The salinity sections present a low salinity surface layer that thins from west to east with the surface layer depth (Figure 28a, b). FKN_01 at the west coast of Franklin Bay contains the greatest amount of ocean heat content in the surface layer of all the stations sampled in 2018 (458 kJ) and the second most freshwater content (12.4 m) (Table 1) and corresponds with a location of bowhead feeding. The ocean heat content in the surface layer at FKN_06 at the east end of the section was only 26 kJ, while the surface layer freshwater content at that station was 1.6 m (Table 1, Figure 28).

CTD data were also collected at six stations (FKN_07, FEX-HC01, FKN_03, AMG_04, AMG_05, AMG_06) along a south-to-north transect in Franklin Bay (Figure 29) from about 83 m depth to 329 m depth (Table 1) towards the Cape Bathurst section (Figure 21). From the south end of Franklin Bay northward, the $N^2$-derived surface layer thickness was 38 m deep at FKN_07 and 39 m at FEX_HC01 and decreased to

between 16 and 22 m in the northern four stations (Table 1, Figure 29). The salinity section (Figure 29) presented a deep, warm (2-3 °C) and fresh (22-25) layer to the 38 m surface layer depth which was uniform above the Pacific water for more than 30 km northward until the surface layer thinned between stations FEX_HC01 and FKN_03 (Figure 29). The south end of Franklin Bay contained a great deal of ocean heat content (423 kJ at FKN_07 and 347 kJ at FEX_HC01) and freshwater (12.5 m at FKN_07 and 11.6 m at FEX_HC01). North of FKN_03 where the bathymetry was between 174-213 m, the water column changed substantially. Here, the $N^2$-derived surface layer depth decreased by about half, and both the ocean heat content and the freshwater content of the surface layer decreased substantially, as did the strength of the stratification above the Pacific water (Figure 29, Table 1 which may be an effect of the sea ice import into the region during the sampling period (Figure 21b, 21c).

Moving northeast from Cape Bathurst, five stations (CPB_01, CPB_02, CPB_03, CPB_04, CPB_HC01) were used to plot the Cape Bathurst oceanographic sections of temperature and salinity (Figure 30). This section exhibits marked increase in bathymetric depth, from 22 m at CPB_01 to 262 m at CPB_04 (Table 1, Figure 30) over a relatively short distance (total section length < 30 km). Sampling could not continue along this transect due to the persistence of sea ice in the mouth of Amundsen Gulf. Within the Cape Bathurst section, the $N^2$-derived surface layer depth was relatively shallow (range = 2 – 13 m). The ocean heat content observed in the section was low (mean = 63.8 kJ) with the maximum ocean heat content (176.8 kJ) occurring at CPB_04 (Table 1). The amount of freshwater residing in the $N^2$-derived surface layer in the Cape Bathurst section was also relatively small, ranging from 4.23 m at CPB_04 to 0.11 m at CPB_02 (Table 1) (mean = 1.58 m). The temperature and salinity sections (Figure 30) seem to indicate a zone of upwelling around station CPB_02, or perhaps the influence of sea ice melt at the surface. It should also be noted that the top 2-3 m of the water column are missing from the profiles due to quality control/assurance methodology, which likely somewhat affects the surface layer values for ocean heat content and freshwater content over the relatively thin surface layer.

In 2018 the Kugmallit (KUG) transect on the Mackenzie Shelf was conducted over five stations (KUG_01, KUG_01b, KUG_01c, KUG_03, KUG_04) sampled at the beginning of the cruise, from on-shelf in 24 m of water to the northernmost station (KUG-04) reached in 2018 in more than 346 m of water (Figure 21). The $N^2$-derived surface layer along the Kugmallit section was thinnest near the continental coast at KUG_01 (1.4 m) and deepened to 19 m at KUG_03 and KUG_04 (Table 1, Figure 31). At KUG_01, the effect of the Mackenzie River is obvious. Salinity in the surface along the Kugmallit section was < 16, and temperature in the surface layer was nearly 9 °C, where the $N^2$-derived surface layer depth was at the

surface due to steadily increasing salinity with depth away from the surface which affected the $N^2$ profile (see cast in Appendix 1, page 96) and the shallow (24 m) bathymetric depth. The surface layer depth affected both the ocean heat content and the freshwater content in the surface layer (Table 1), substantially underestimating both. Moving offshore over the Mackenzie shelf, the surface layer depth was accurately defined by the $N^2$-derivation at the northern four stations (Figure 31, Table 1), and the freshwater and heat diffused used away from the riverine source both meridionally and with depth from the ocean surface (Figure 31). Ocean heat content in the surface layer decreased from 138.3 kJ (KUG_01b) to 68.7 kJ (KUG_01c) to 5.7 and 8.3 kJ (KUG_03, KUG_04). Reflecting in part the distance from the Mackenzie River as a source of heat, and the sea ice which covered the north end of the Kugmallit section for much of August 2018 (Figure 21), so much so that sections out to 1300 m depth sampled in other years (see for e.g. Galley et al., 2023) were forgone in 2018. Interestingly, there is substantial heat below the surface mixed layer in 2018 in the Kugmallit section, with almost no decrease in salinity (Figure 31 and cast plots in Appendix A), which may be heat/Pacific water transported along the shelf at depth from the Bering Strait. Warm water along the continental coast of Alaska extending into the Inuvialuit Settlement Region seems to align with increased salmon catches in the region (Dunmall et al., 2024). Freshwater content in the surface layer from KUG_01b northward through the for stations on the other hand increases with the depth of the surface layer (2.75m, 3.06 m, 4.19 m, 4.24 m).

**3.4 Autumn 2018**

In October, November and December 2018, the study region cooled steadily month-over-month (Figure 1), with October 2018 air temperatures warmer than the climatological average in the western and southwestern area of the Beaufort Sea (Figure 2) where negative summer sea ice anomalies occurred (Figure 12). November and December 2018 were anomalously cool (Figure 2). In November 2018 warm air extended north from the continental landmass, with air temperatures warmer than -16 °C on the Mackenzie shelf and slope, and within Amundsen Gulf and Dolphin and Union Strait (Figure 1). These temperatures over the open ocean were up to 10 °C warmer than the long-term (1983-2010) climatological average (Figure 2) for the month. In December, the continental landmass and southern half of the marine region were much warmer than Banks Island, Victoria Island, and the regional 2-m air temperature anomalies had switched to small and negative, meaning much of the region was cooler than the climatological average for December (Figure 2).

The SLP pattern in autumn 2018 began with the Beaufort High in the northwest corner of the study region and lower SLP over the Brooks Range and in the northeast (Figure 3). This SLP pattern changed in

November, as higher SLP broadened over much of the north half of the study region. In December 2018 the SLP pattern changed again with higher pressure over the north and east portion of the study region, and low pressure over the Brooks Range in the southwest (Figure 3). In November and December, the entire regions' SLP was lower than the climatological average in both months (Figure 4). The positions of the high and low pressure and zonal isobars in the region enable northeasterly and easterly winds in Autumn 2018 (Figure 5) which were close to the long-term average velocity (Figure 6).

Sea ice formation continued in the region in October 2018 (Figure 13), having begun in September (Figure 11). October total sea ice concentration in the region (Figure 13) was more complete than average (Figure 14) due to substantial positive old sea ice anomalies which were circulated anticyclonically into the region from the north and across the Mackenzie slope to the west (Figure 13, 15). In addition, sea ice that had largely stuck around all summer in the Beaufort Sea (e.g. Figure 21) remained in October to "seed" the growth of new-plus-young sea ice in October within the periphery of the Beaufort Sea ice pack and in Amundsen Gulf (Figure 13) by maintaining the ocean surface temperature at the freezing point; this new-plus-young ice growth was highly positively anomalous for October (Figure 14). October was the last month in 2018 with appreciable sea ice-adjusted SSRD to open water in the region (Figure 17); negative sea ice-adjusted SSRD anomalies were present across the Mackenzie shelf and slope, in western Amundsen Gulf and Franklin Bay, and along the west coast of Banks Island (Figure 18). With the increased velocity of regional anticyclonic sea ice motion in November (Figure 15) and complete regional sea ice cover (Figure 13), the old sea ice concentrations in the north were redistributed clockwise south and then west across the Mackenzie slope all the while being augmented with first-year sea ice growth (Figure 13) which was negatively anomalous (Figure 14). Finally, the western periphery of the old ice pack, the southern reaches of the Mackenzie shelf and much of Amundsen Gulf generated substantial concentrations of new-plus-young sea ice (Figure 13) which were largely positively anomalous for November (Figure 14) because that area has historically been covered with old and first-year sea ice at that time of year. In December, the total sea ice concentration in the study region remained complete but almost entirely mobile (Figure 15) save for thin bands of landfast sea ice at the continental coast, and surrounding Banks Island and Victoria Island (Figure 13). The December sea ice was composed of mostly old sea ice in the northwest, including in M'Clure Strait, and mostly first-year sea ice in the south and east, including in Amundsen Gulf (Figure 13), while ice motion in the region was predominantly to the west (Figure 15). The mean accumulated sea ice adjusted SSRD in 2018 (Figure 20) increased when the September – December period was added compared to Figure 19. The addition of September and October SSRD amplified the positive and negative SSRD anomalies in 2018 (Figure 20b).

## 4 Conclusions

Winter 2018 was warmer than the long-term climatological average. The Beaufort High pressure center was displaced from its typical position in January and February, leading to anomalous westerly and southwesterly winds in those months. Old sea ice positive anomalies were present in winter 2018 extending meridionally along the coast of the Canadian Arctic Archipelago, largely due to import from the north, while first year sea ice positive anomalies occurred in the western reaches of the Beaufort Sea and M'Clure Strait as first year sea ice continues to replace old ice in the region over time. Sea ice in the study region was almost entirely mobile in winter 2018, and high concentrations of new-plus-young sea ice occurred in the Cape Bathurst flaw lead polynya in January and March, while the lead closed in February due to sea ice motion toward the southeast.

In spring 2018, the anomalously warm air temperatures continued to persist into May, before the region exhibited slightly cooler than average air temperatures in June. The Beaufort High occupied its more typical location in April and May enabling anticyclonic sea ice motion in the region in spring. The sea ice in the study region remained mobile in April and began to dynamically breakup in May. Dynamic breakup continued into June via anticyclonic ice motion. Dynamic breakup in May combined with cool air temperatures produce anomalous new-plus-young sea ice in the flaw lead, western Amundsen Gulf, and in the diverging pack ice, which contained less than average concentrations of first-year ice due to breakup. Dynamic breakup slowed in June due to a shift in the SLP which reduced the ice motion velocities in the Beaufort Sea.

Summer 2018 was characterized by slightly warmer than average 2-m air temperatures over the Mackenzie shelf and slope, in Amundsen Gulf, and across the northeast corner of the study region in July and August, before the entire region was anomalously warm in September. The position of the high SLP center changed in each of the summer months, and the wind direction in the region was predominantly northerly in July and August, and northeasterly in September. The sea ice motion in summer 2018 also varied, moving sea ice into the region from the west in July, and from the north in August and September. The sea ice concentration in summer 2018 was higher than average along the coast of the Archipelago where positively anomalous concentrations of old sea ice were imported from the north, and lower than average in the western Beaufort Sea as sea ice was advected west and melted. In September 2018, as old ice continued to be imported from the north down the coast of the Archipelago and into the mouth of Amundsen Gulf, positively anomalous concentrations of new-plus-young sea ice grew around the periphery of the September old ice pack. As a result, negative sea ice-adjusted SSRD anomalies occurred

coincident to old ice, while positive sea ice-adjusted SSRD anomalies occurred in the relatively ice-free western Beaufort Sea over summer. The accumulated sea ice-adjusted SSRD in the region from January to August 2018 was concentrated on the Mackenzie shelf and slope, in Amundsen Gulf and its embayments, and in eastern Amundsen Gulf due to dynamic breakup in May.

Using CTD stations sampled in the region in August and September 2018, the sea surface temperature ranged from -0.2 °C in Franklin Bay to 8.97 °C north of Kugmallit Bay in the Mackenzie River plume, and the surface salinity ranged from 15.8 north of Kugmallit Bay in the Mackenzie River plume to 30.8 at Cape Bathurst where upwelling may have been observed. The thinnest $N^2$-derived surface layer depth was 1.4 m, and the deepest $N^2$-derived surface layer depth was 39 m. The maximum ocean heat content in the surface layer was 457.9 kJ in southern Franklin Bay. Freshwater content in the surface layer was only 0.11 m at Cape Bathurst likely due to upwelling, and 12.5 m at the western shore of Franklin Bay, likely due to the influence of the Horton River and some sea ice melt. Oceanographic sections presented here include those sampled in close proximity to remaining sea ice in August (i.e., Kugmallit Bay, Cape Bathurst, Franklin and Darnley Bay transects) and inner Amundsen Gulf oceanographic sections across Dolphin and Union Strait and in Minto Inlet which were clear of sea ice.

October exhibited warmer than average air temperatures over ice-free southern and western reaches of the marine region, while November was especially warm in the south half of the study area. Air temperatures over the entire region were slightly below average in December 2018. The Beaufort High resided northwest of the study region in October and November, and in the northeast of the study region in December, creating anticyclonic winds and sea ice motion in all three autumn months. Sea ice formation and growth that had begun in September 2018 continued in earnest in autumn, producing new-plus-young sea ice around and within the periphery of the Beaufort sea ice pack in October, and filling the flaw lead and Amundsen Gulf with new-plus-young sea ice in November. New-plus-young sea ice formed in October and November thickened to become first-year sea ice in December. Finally, the Cape Bathurst flaw lead polynya complex was still well-established in December 2018 with higher-than-average concentrations of new-plus-young sea ice indicating consistent divergence in the pack, and the sea ice in the region was almost completely mobile save for a very thin band of landfast sea ice along the coasts of the continent and Banks and Victoria Islands.

## 5 Acknowledgements

We thank the Inuvialuit Game Council, the Fisheries Joint Management Committee, and the Western Arctic Marine Protected Area steering committee for supporting this work and providing valuable input into study objectives. We especially thank the Olohaktomiut Hunters and Trappers Committee for their support of an unexpected crew change. We acknowledge the invaluable support of the *CCGS Sir Wilfred Laurier*, for providing ice escorts to and from the study area and during two occasions during scientific work, and for kindly agreeing to a rendezvous to transfer a replacement CTD deck unit provided by Dr. Humfrey Melling. And finally, thanks to the crew and management team of the *F/V Frosti* for their support and effort to navigate a very challenging field program.

Funding for the 2018 field year was provided by various DFO sources including the National Conservation Plan, and the International Governance Strategy. External funds were received from the Beaufort Regional Strategic Environmental Assessment (RSEA), administered through Crown Indigenous Relations and Northern Affairs Canada.

## 6 References


Babb, D. G., Galley, R. J., Howell, S. E. L., Landy, J. C., Stroeve, J. C., Barber, D. G. 2022. Increasing multiyear sea ice loss in the Beaufort Sea: A new export pathway for the diminishing multiyear ice cover of the Arctic Ocean, Geophysical Research Letters, 49, doi: 10.1029/2021GL097595.

Bailey, E., & Timmermans, M.-L. 2025. Investigating the relative roles of dynamics and thermodynamics in sea-ice volume changes in the Canada basin. Journal of Geophysical Research: Oceans, 130, e2024JC022075. https://doi.org/10.1029/2024JC022075

Barton, B. I., Lenn, Y.-D., Lique, C. 2018. Observed Atlantification of the Barents Sea causes the polar front to limit the expansion of winter sea ice. Journal of Physical Oceanography, 48(8), doi: https://doi.org/10.1175/JPO-D-18-0003.1

DFO. 2010. Monitoring indicators for the Tarium Niryutait Marine Protected Area (TNMPA). DFO Can. Sci. Advis. Sec. Sci. Advis. Rep. 2010/059.

DFO. 2014. Re-evaluation of Ecologically and Biologically Significant Areas (EBSAs) in the Beaufort Sea. DFO Can. Sci. Advis. Sec. Sci. Advis. Rep. 2014/052.

DFO. 2015. Angunniaqvia Naiqiqyuam Area of interest: monitoring indicators, protocols and strategies. DFO Can. Sci. Advis. Sec. Sci. Advis. Rep. 2015/025.

DFO. 2022. Science Advice to Assist in the Development of an Ecological Monitoring Plan for the Anguniaqvia Niqiqyuam Marine Protected Area. DFO Can. Sci. Advis. Sec. Sci. Advis. Rep. 2022/015.

Dunmall, K. M., Langan, J. A., Cunningham, C. J., Reist, J. D., Melling, H. 2024. Pacific salmon in the Canadian Arctic highlight a range-expansion pathway for sub-Arctic fishes. *Global Change Biology*, 30, e17353, https://doi.org/10.1111/gcb.17353.

Fequet, D. (ed). 2005. Manual of standard procedures for observing and reporting ice conditions, Canadian Ice Service - Environment Canada, Catalogue No. En56-175/2005, ISBN 0-660-62858-9.

Galley, R. J., Babb, D., Ogi, M., Else, B. T. G., Geilfus, N.-X., Crabeck, O., Barber, D. G., Rysgaard, S. 2016. Replacement of multiyear sea ice and changes in the open water season duration in the Beaufort Sea since 2004. Journal of Geophysical Research – Oceans, 121, doi: 10.1002/2015JC011583.

Galley, R., Niemi, A., Eert, J., Majewski, A., and Williams, W. 2023. Canadian Beaufort Sea - Marine Ecosystem Assessment (CBS-MEA) report on the physical system - 2019. Can. Tech. Rep. Hydrogr. Ocean Sci. 364: ix + 115 p.

Halliday, W. D., Brittain, S. A., Niemi, A., Majewski, A. R., Mouy, X., Insley. S. J. 2022. The underwater soundscape of Minto Inlet, Northwest Territories, Canada. Arctic 75: 462-479. doi: 10.14430/arctic76400

Hersbach, H., Bell, B., Berrisford, P., Biavati, G., Horányi, A., Muñoz Sabater, J., Nicolas, J., Peubey, C., Radu, R., Rozum, I., Schepers, D., Simmons, A., Soci, C., Dee, D., Thépaut, J-N. 2018. ERA5 hourly data on single levels from 1959 to present. Copernicus Climate Change Service (C3S) Climate Data Store (CDS). (Accessed June 2022), 10.24381/cds.adbb2d47

Insley, S. J., Halliday, W. D., Mouy, X., Diogou, N. 2021. Bowhead whales overwinter in the Amundsen Gulf and Eastern Beaufort Sea. Royal Society Open Science, 8:202268. doi: 10.1098/rsos.202268

Kelley, D. E. 2018. Oceanographic analysis with R. Springer, New York, NY. ISBN: 978-1-4939-8844-0, doi: 10.1007/978-1-4939-8844-0, 290pp+xxi.

Niemi, A., Majewski, A., Eert, J., Ehrman, A., Michel, C., Archambault, P., Atchison, S., Cypihot, V., Dempsey, M., de Montety, L., Dunn, M., Geoffroy, M., Hussherr, R., MacPhee, S., Mehdipour, N., Power, M., Swanson, H., Treau de Coeli, L., Walkusz, W., Williams, W., Woodard, K., Zimmerman, S., Reist, J. 2020. Data from the BREA-MFP and CBS-MEA research programs describing the Anguniaqvia niqiqyuam Marine Protected Area (ANMPA) ecosystem. Can. Data Rep. Fish. Aquat. Sci. 1316: ix + 90 p.

NOAA, 2018. Assessing the global climate in 2017, https://www.ncei.noaa.gov/news/global-climate-201712, accessed 15 July 2026.

NSIDC, 2026. 2018 winter Arctic sea ice: Bering down, https://nsidc.org/sea-ice-today/analyses/2018-winter-arctic-sea-ice-bering-down, accessed 15 July 2026.

Osborne, E., Richter-Menge, J., Jeffries, M., Eds., 2018. Arctic Report Card 2018, https://www.arctic.noaa.gov/Report-Card

Perovich, D., Meier, W., Tschudi, M., Farrell, S., Hendricks, S., Gerland, S., Haas, C., Krumpen, T., Polashenski, C., Ricker, R., Webster, M. 2018. Sea ice [in Arctic Report Card 2018], https://www.arctic.noaa.gov/Report-Card

R Core Team, 2022. R: A language and environment for statistical computing. R Foundation for Statistical Computing, Vienna, Austria. https://ww.R-project.org/

Sharqawy, M. H., Lienhard V, J., H., Zubair, S. M. 2010. Thermophysical properties of seawater: a review of existing correlations and data, Desalination and Water Treatment, 16: 354-380, doi: 10.5004/dwt.2010.1079.

Stabeno, P. J. and Bell, S. W. 2019. Extreme conditions in the Bering Sea (2017-2018): Record breaking low sea-ice extent. Geophysical Research Letters, 46, 8952-8959, http://doi.org/10.1029/2019GL083816.

Stirling, I. 1980. The biological importance of Polynyas in the Canadian Arctic. Arctic, 33: 303-315.

Sumata, H., de Steur, L., Gerland, S., Divine, D. V., Pavlova, O. 2022. Unprecedented decline of Arctic sea ice outflow in 2018. Nature Communications, 13, doi: 10.1038/s41467-022-29470-7.

Tivy, A., Howell, S. E. L., Alt, B., McCourt, S., Chagnon, R., Crocker, G., Carrieres, T., Yackel, J. J. 2011. Trends and variability in summer sea ice cover in the Canadian Arctic based on the Canadian Ice Service Digital Archive, 1960-2008, and 1968-2008. Journal of Geophysical Research, Oceans, 116(C3), doi: 10.1029/2009JC005855.

Wang, Y., Liu, N., and Zhang, Z. 2021. Sea Ice Reduction During Winter of 2017 Due to Oceanic Heat Supplied by Pacific Water in the Chukchi Sea, West Arctic Ocean. Front. Mar. Sci. 8:650909. doi: 10.3389/fmars.2021.650909

Tschudi, M., Meier, W. N., Stewart, J. S., Fowler, C., Maslanik, J. 2019. *Polar Pathfinder Daily 25 km EASE-Grid Sea Ice Motion Vectors, Version 4.* [1983-2021]. Boulder, Colorado USA. NASA National Snow and Ice Data Center Distributed Active Archive Center. doi: https://doi.org/10.5067/INAWUWO7QH7B. [June 2022].

Woodgate, R. A., Weingartner, T., Lindsay, R. 2010. The 2007 Bering Strait oceanic heat flux and anomalous Arctic sea-ice retreat. Geophysical Research Letters, 37, L01602, doi: 10.1029/2009GL041621.

# 7 Figures

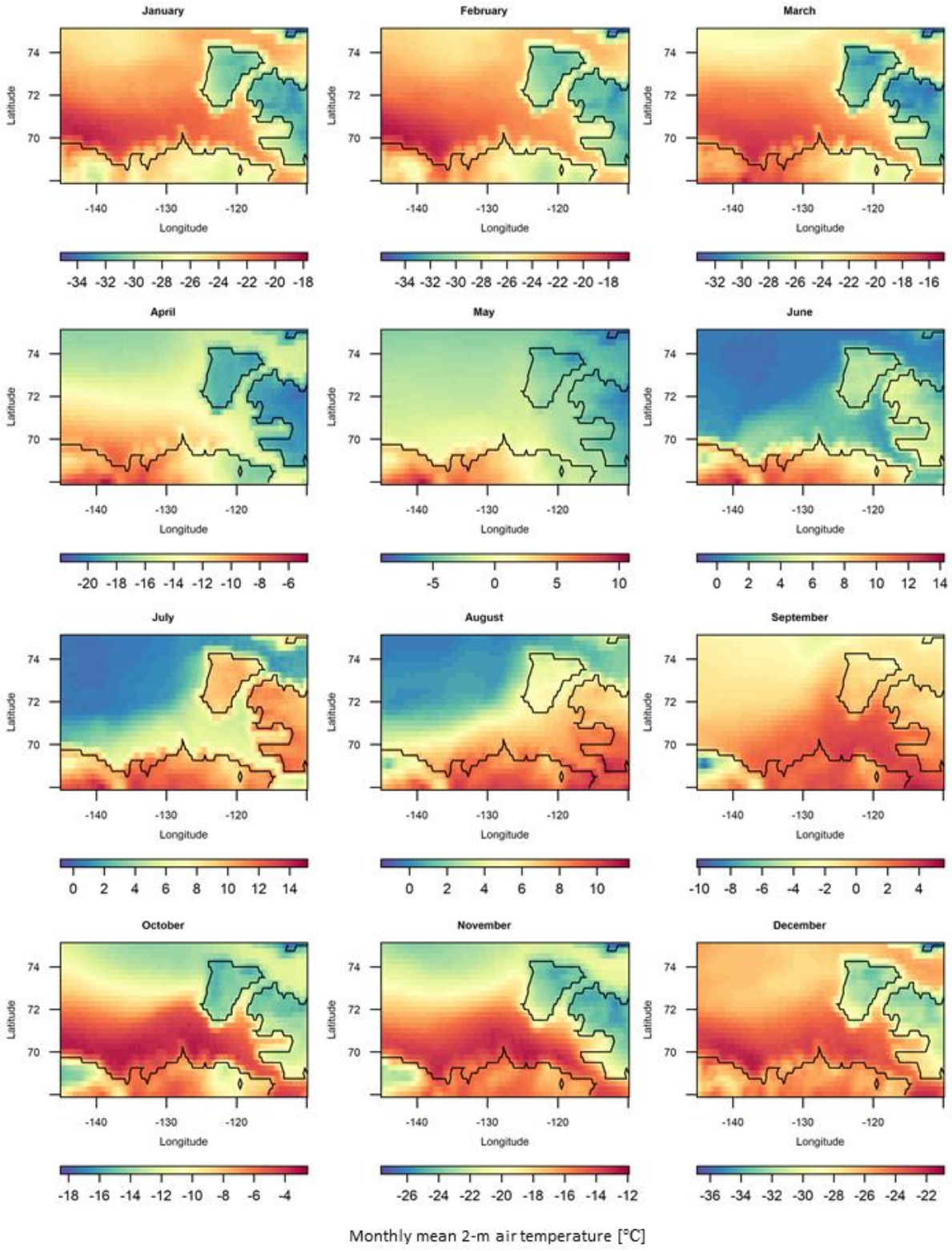



Figure 1. Monthly mean 2-m air temperature (°C) in 2018 over the Beaufort Sea and Amundsen Gulf.

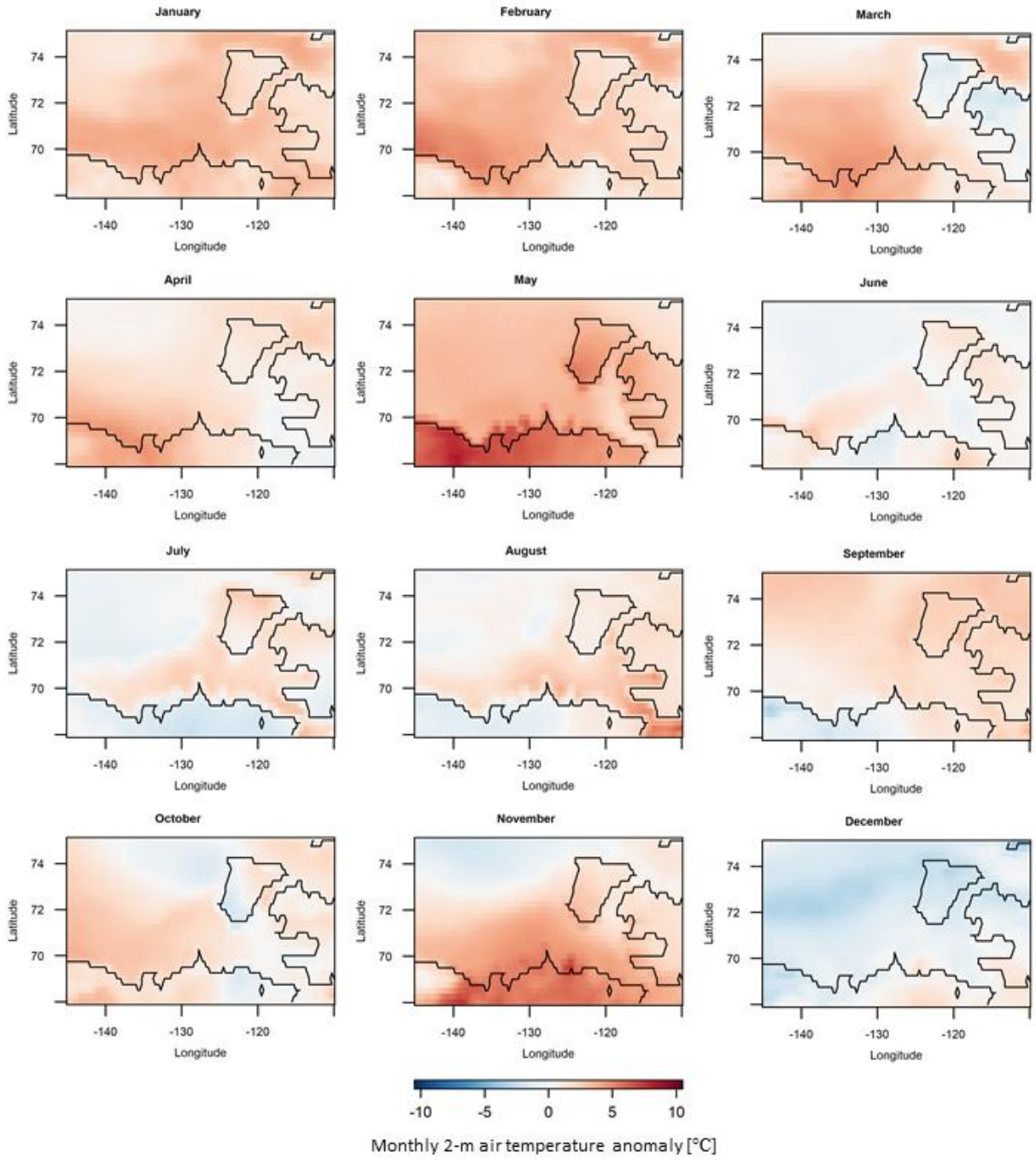



Figure 2. Monthly 2-m air temperature anomalies (°C) in 2018 from the climatological average period 1983-2010 in the Beaufort Sea and Amundsen Gulf.

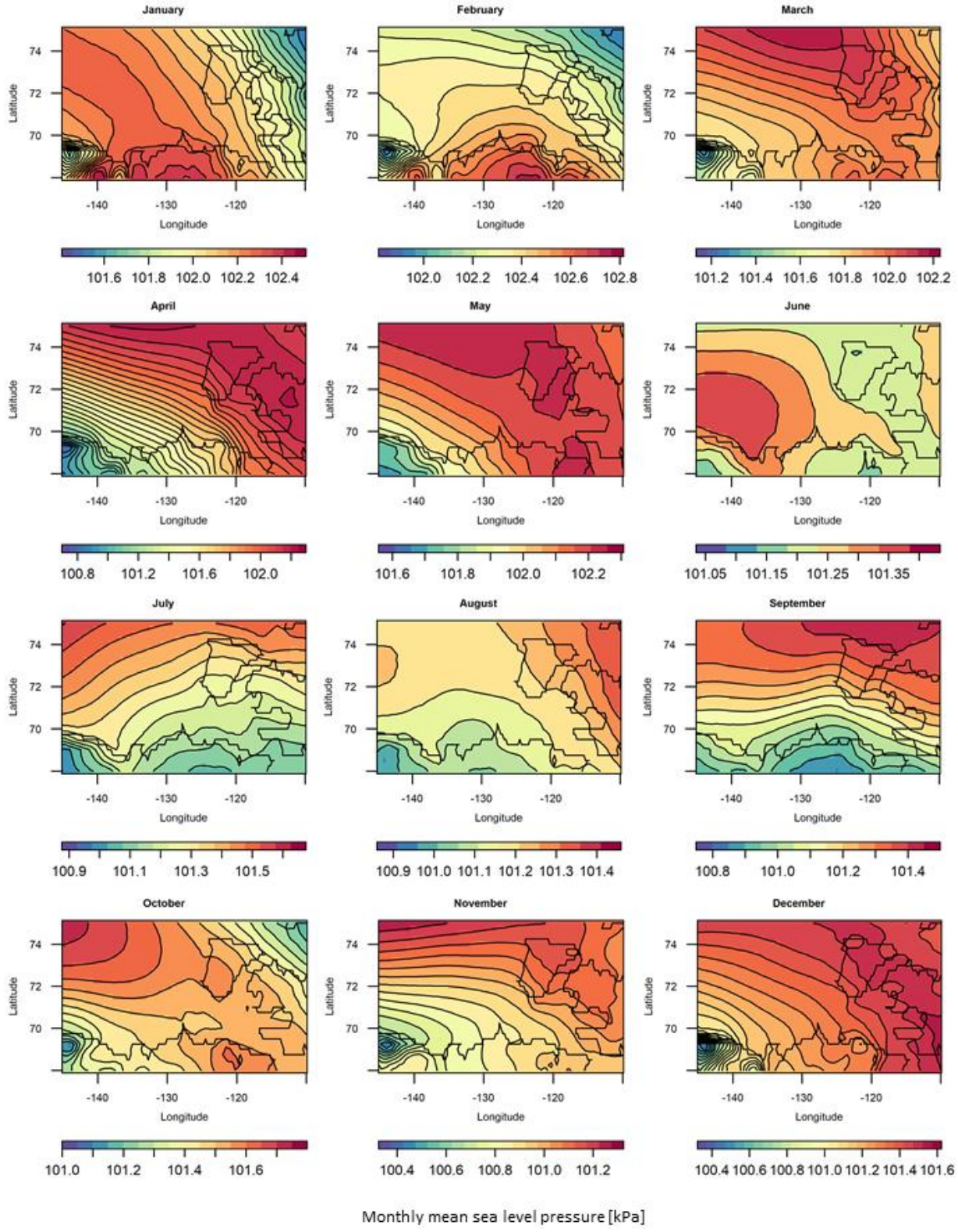



Figure 3. Monthly sea level pressure (kPa) over the Beaufort Sea and Amundsen Gulf in 2018.

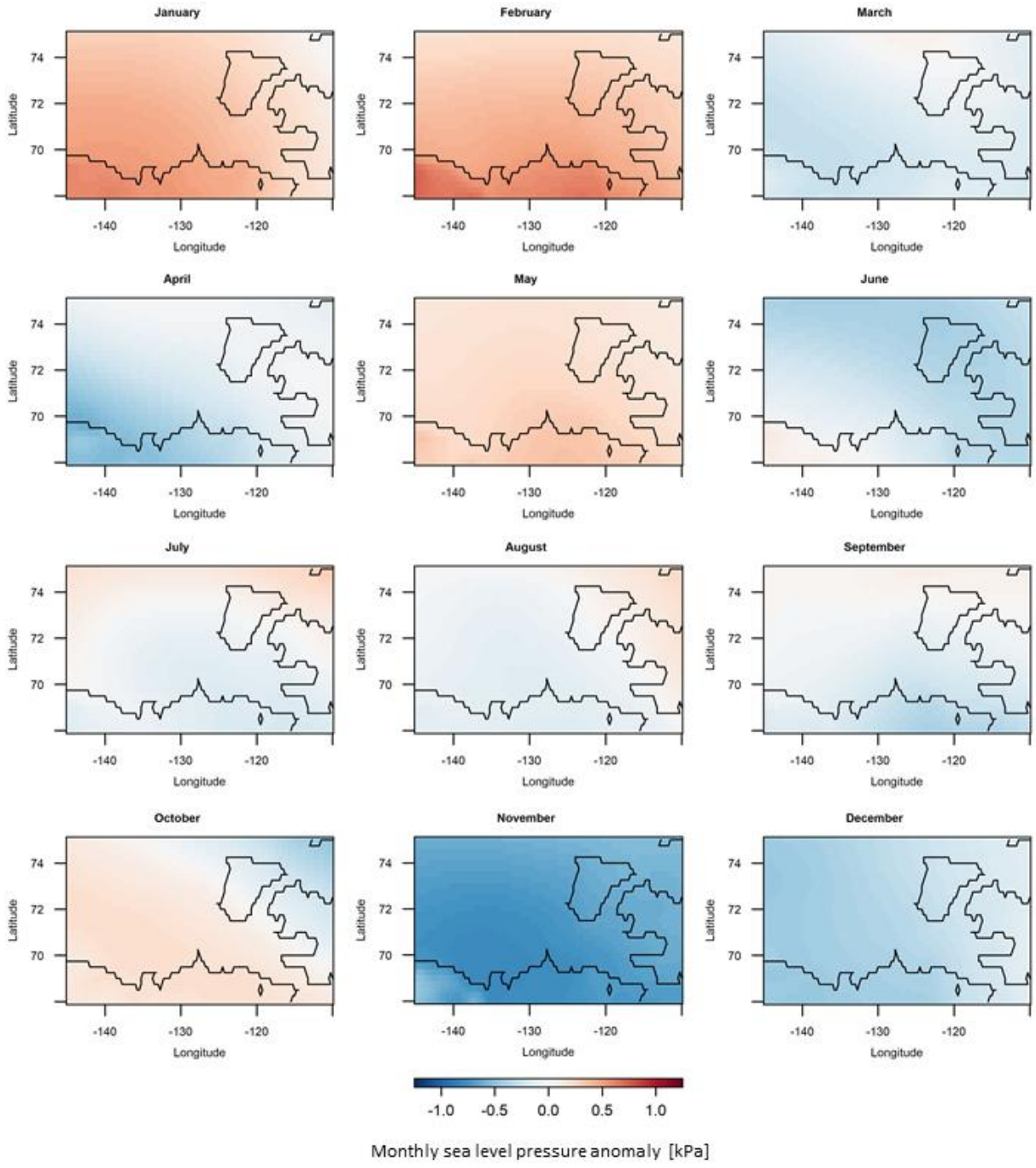



Figure 4. Monthly sea level pressure anomalies (kPa) in 2018 from the climatological average period 1983-2010 in the Beaufort Sea and Amundsen Gulf.

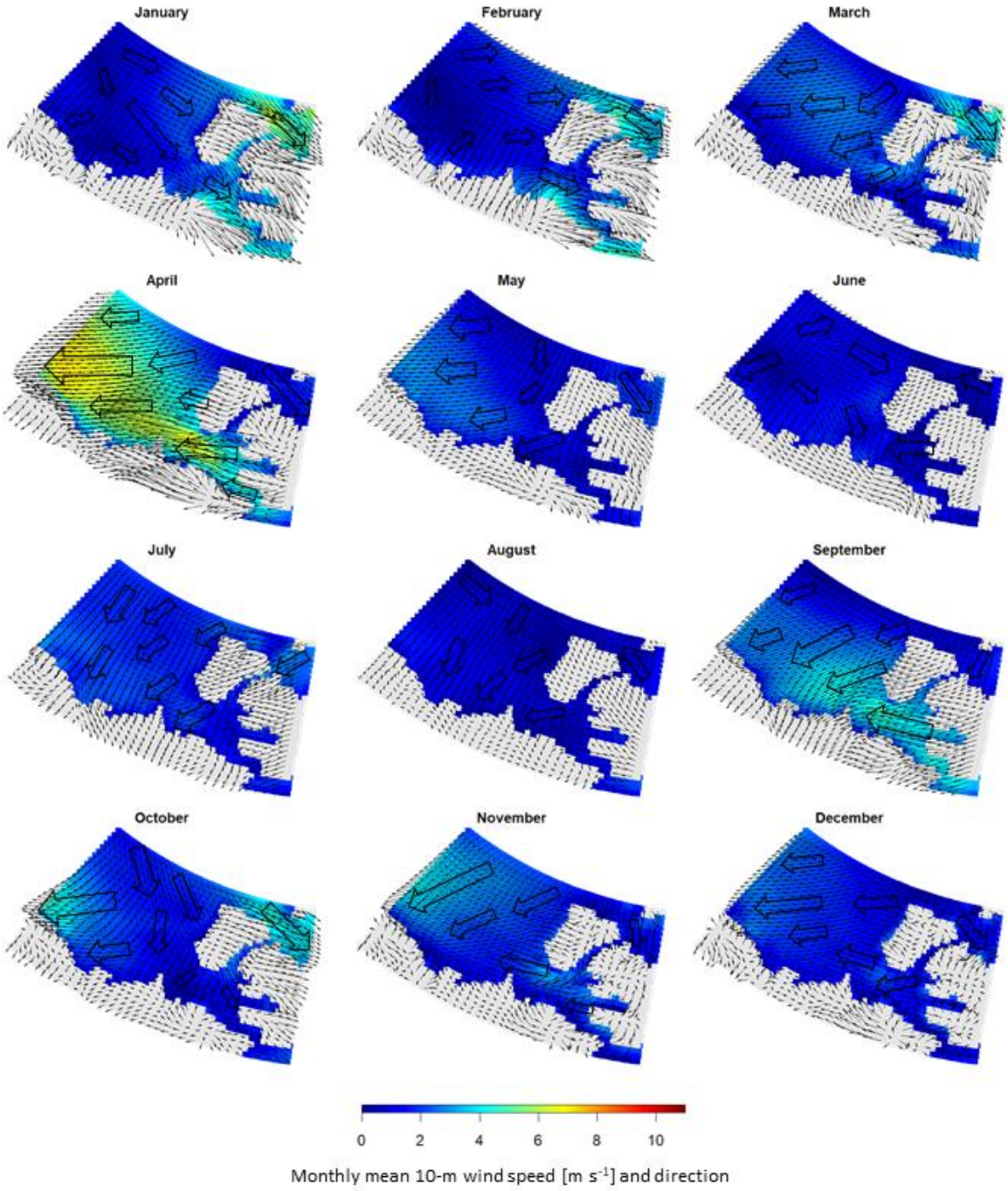



Figure 5. Monthly mean 10-m wind speed (m $s^{-1}$) and direction in 2018 in the Beaufort Sea and Amundsen Gulf.

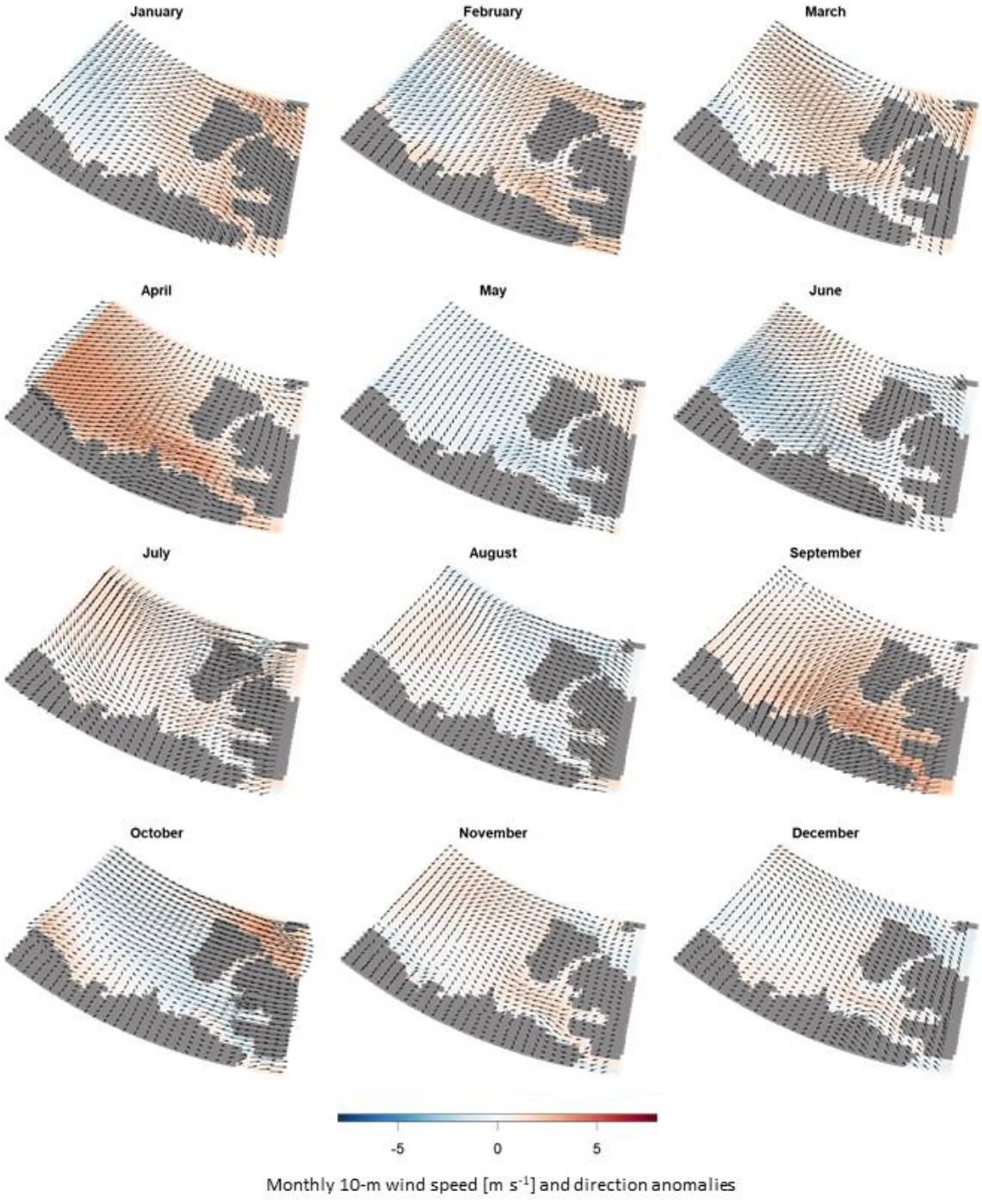



Figure 6. Monthly 10-m wind speed (m $s^{-1}$) and direction anomalies from the climatological average period 1983-2010 in the Beaufort Sea and Amundsen Gulf in 2018.

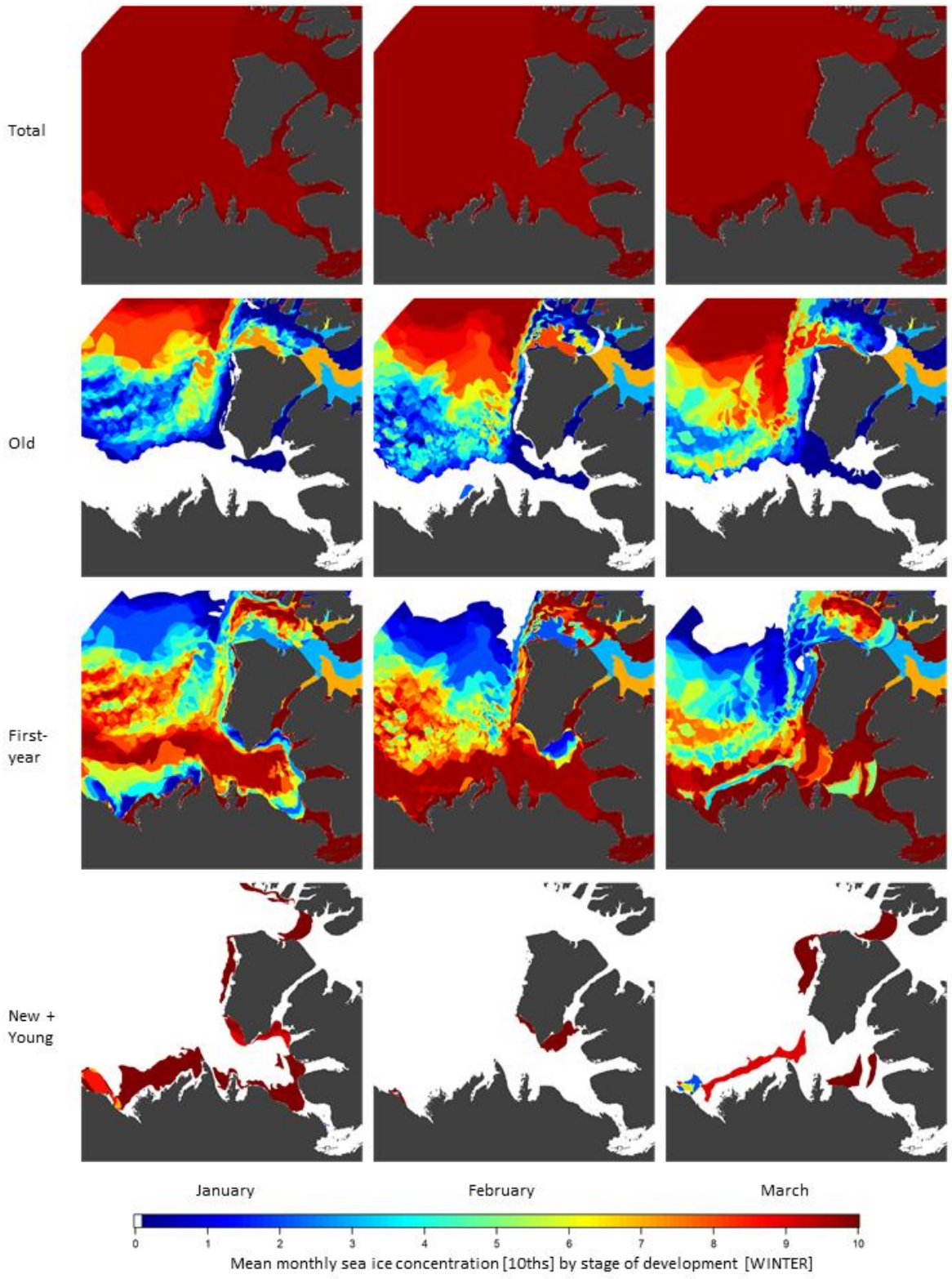



Figure 7. Mean monthly sea ice concentration ($10^{ths}$) for total sea ice and three stages of development (old, first-year, and young + new ice) for January, February, and March [winter] 2018.

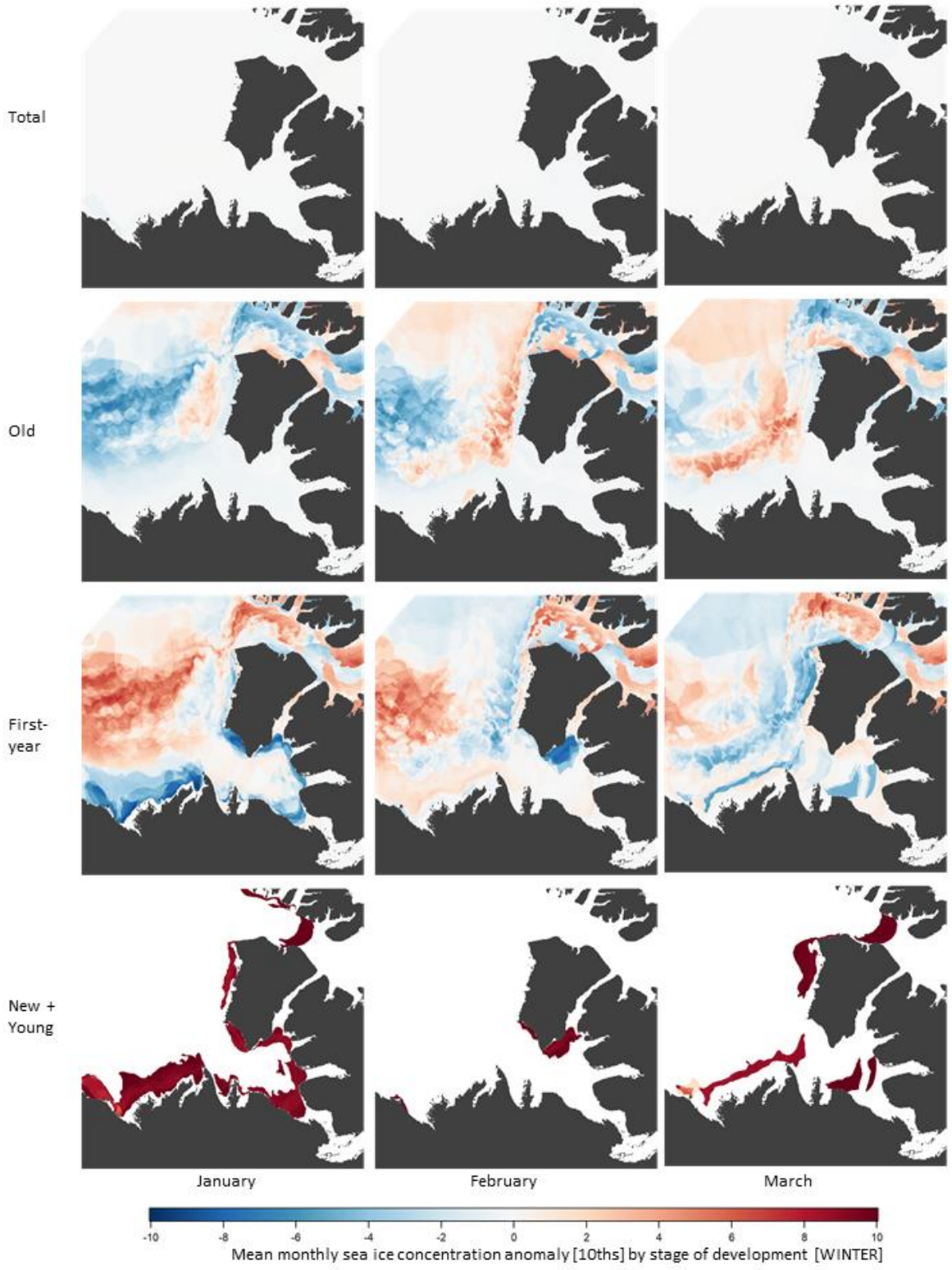



Figure 8. Mean monthly sea ice concentration anomalies ($10^{ths}$) for total sea ice and three stages of development (old, first-year, and young + new ice) for January, February, and March [winter] 2018.

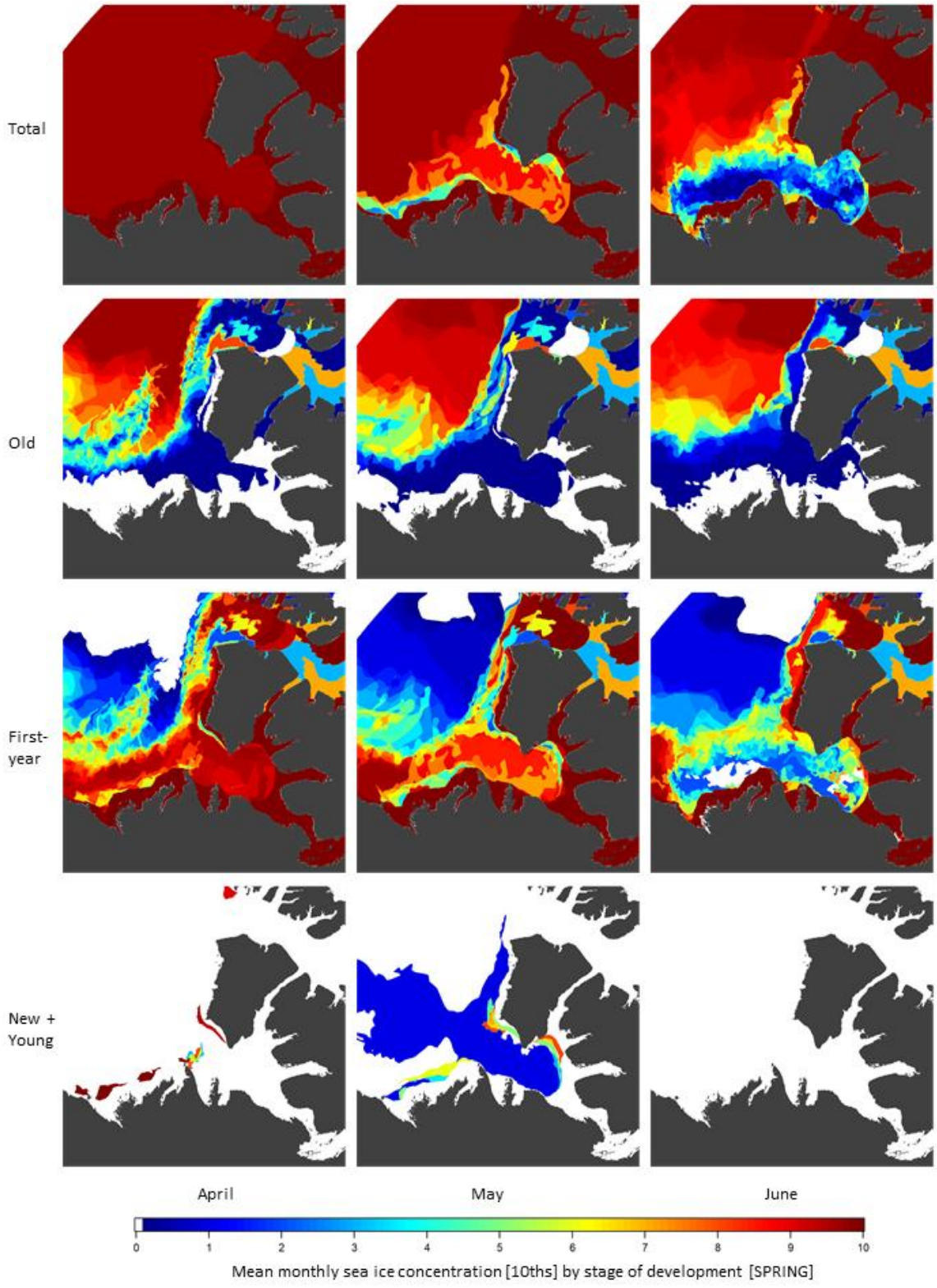



Figure 9. Mean monthly sea ice concentration ($10^{ths}$) for total sea ice and three stages of development (old, first-year, and young + new ice) for April, May, and June [spring] 2018.

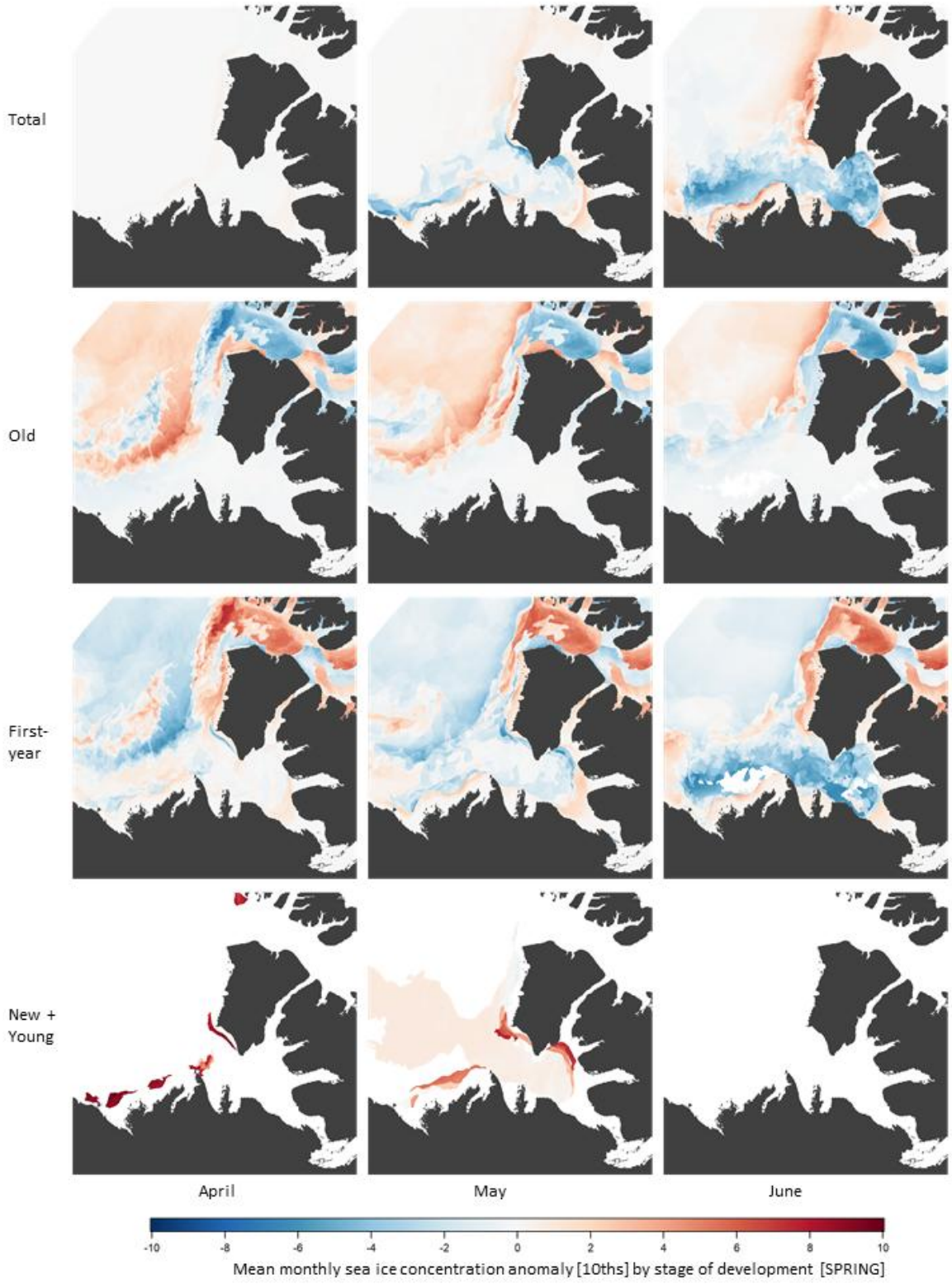



Figure 10. Mean monthly sea ice concentration anomalies ($10^{ths}$) for total sea ice and three stages of development (old, first-year, and young + new ice) for April, May, and June [spring] 2018.

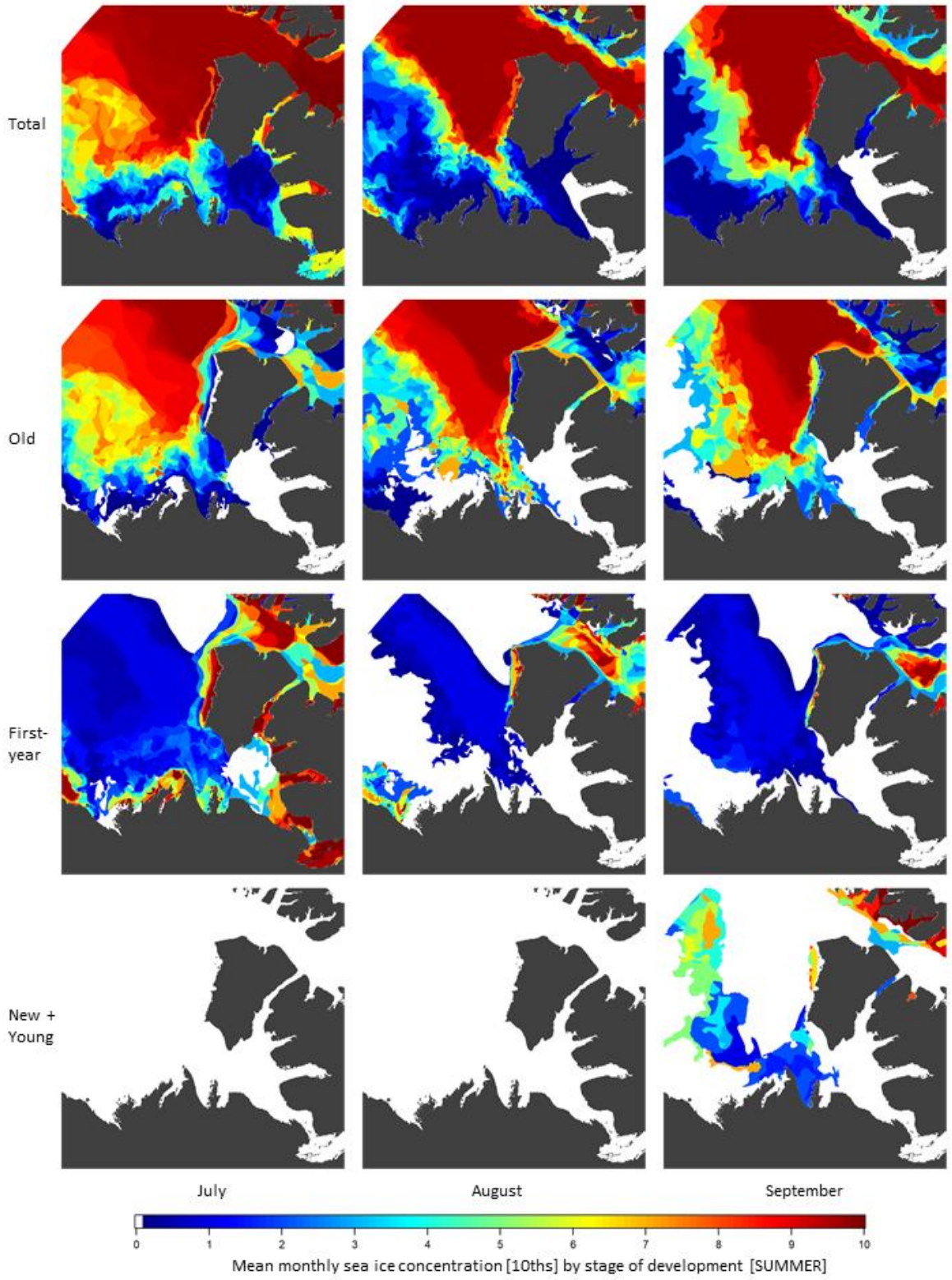



Figure 11. Mean monthly sea ice concentration ($10^{ths}$) for total sea ice and three stages of development (old, first-year, and young + new ice) for July, August, and September [summer] 2018.

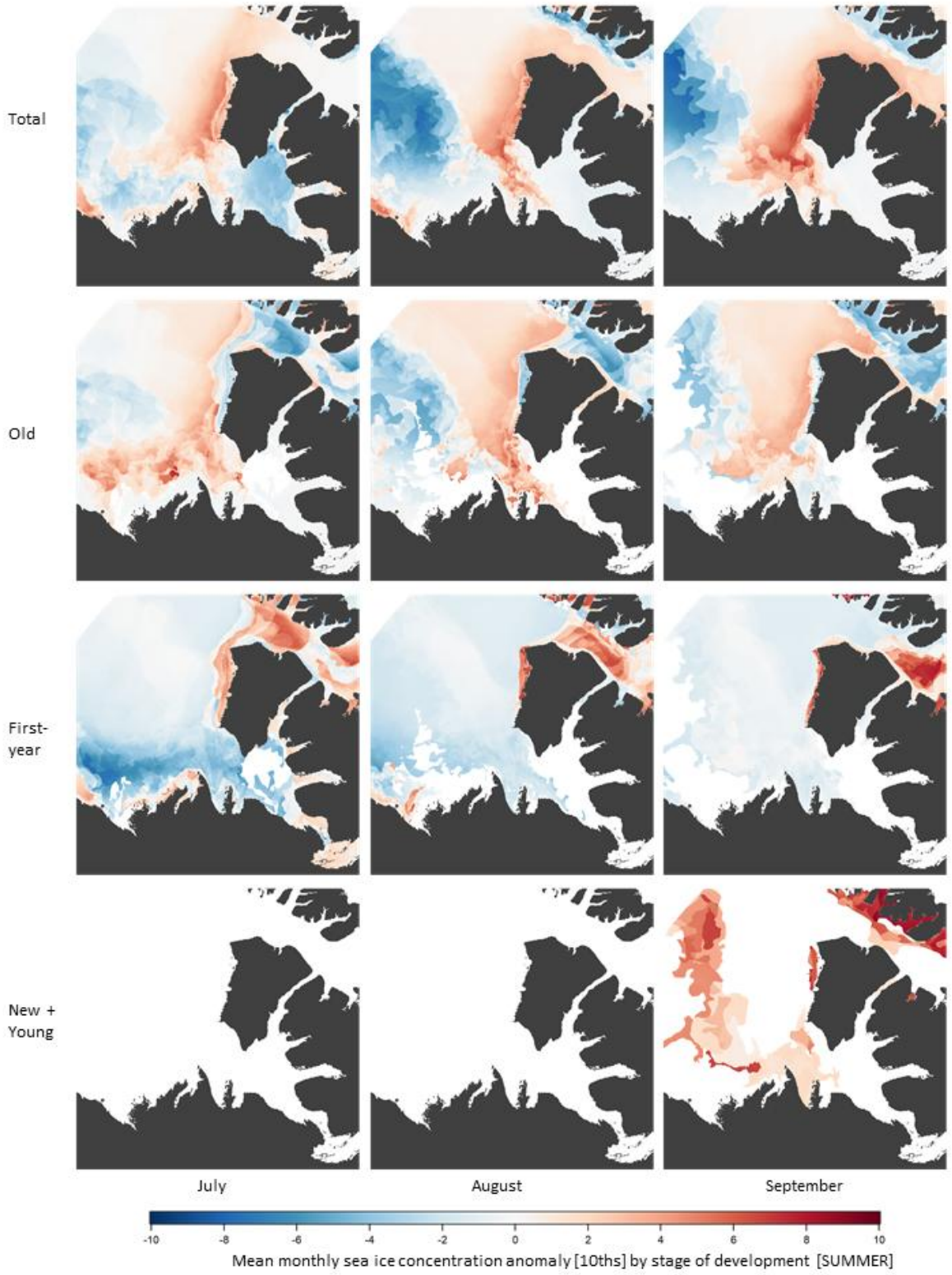



Figure 12. Mean monthly sea ice concentration anomalies ($10^{ths}$) for total sea ice and three stages of development (old, first-year, and young + new ice) for July, August, and September [summer] 2018.

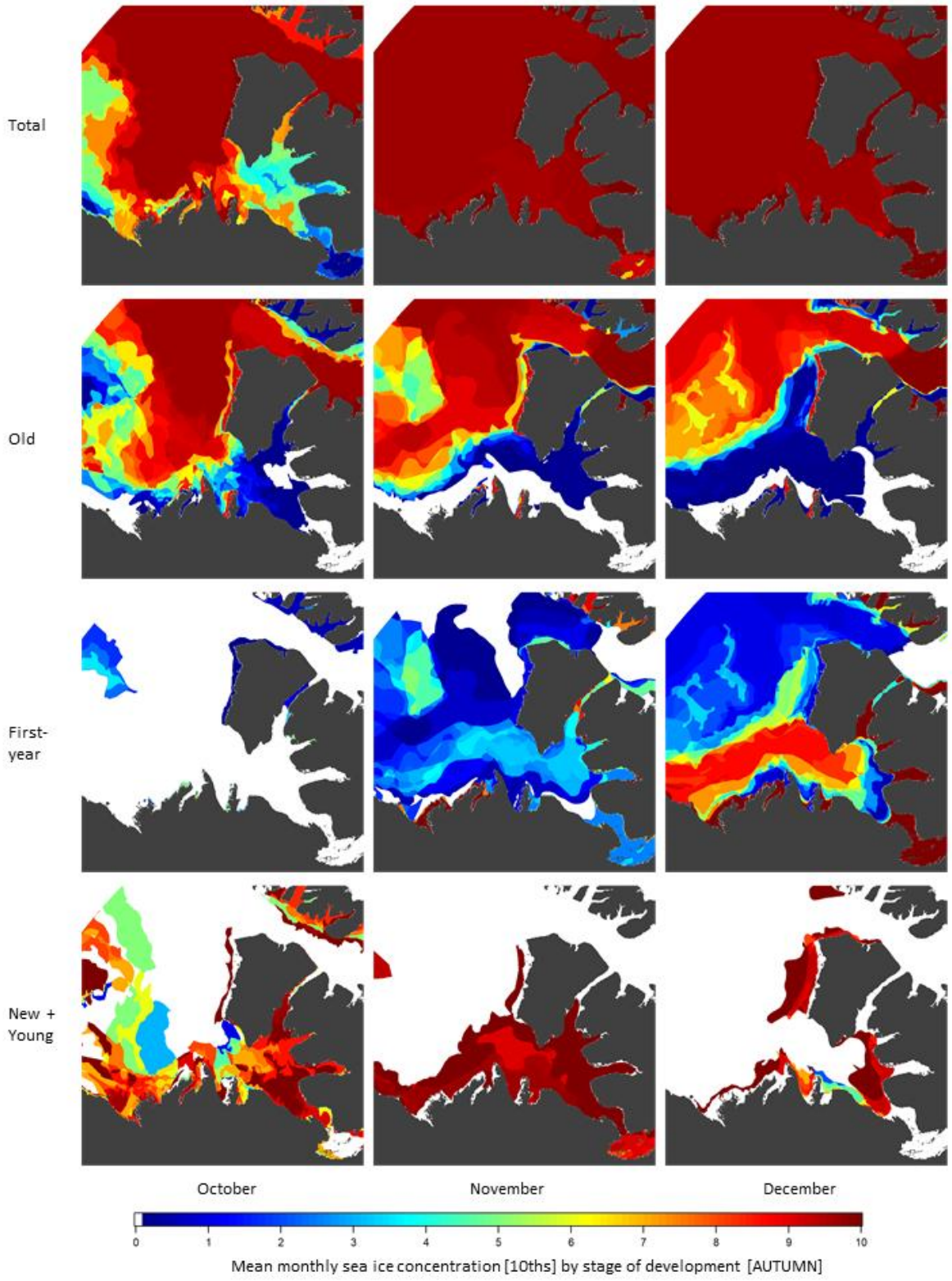



Figure 13. Mean monthly sea ice concentration ($10^{ths}$) for total sea ice and three stages of development (old, first-year, and young + new ice) for October, November, and December [autumn] 2018.

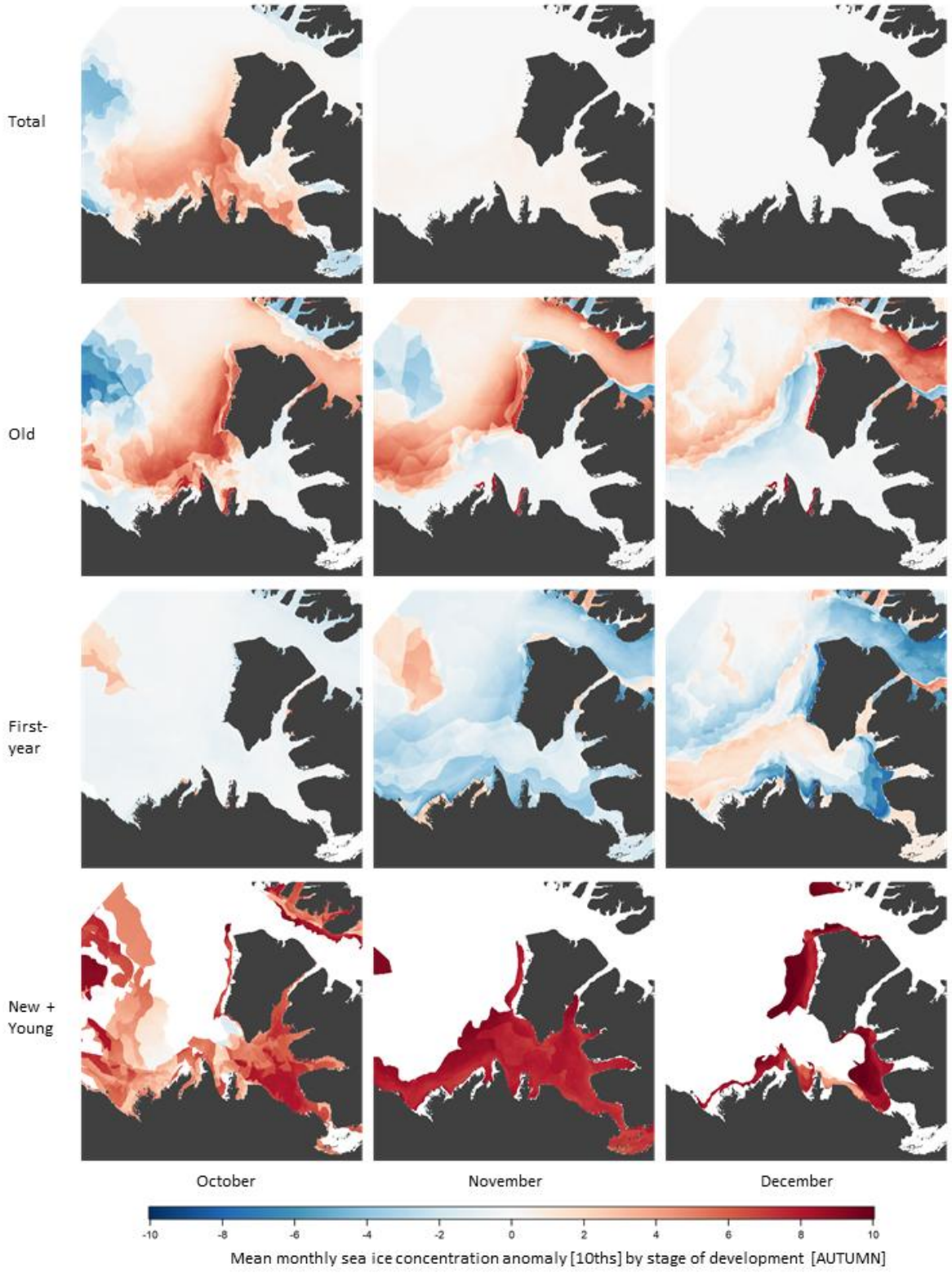



Figure 14. Mean monthly sea ice concentration anomalies ($10^{ths}$) for total sea ice and three stages of development (old, first-year, and young + new ice) for October, November, and December [autumn] 2018.

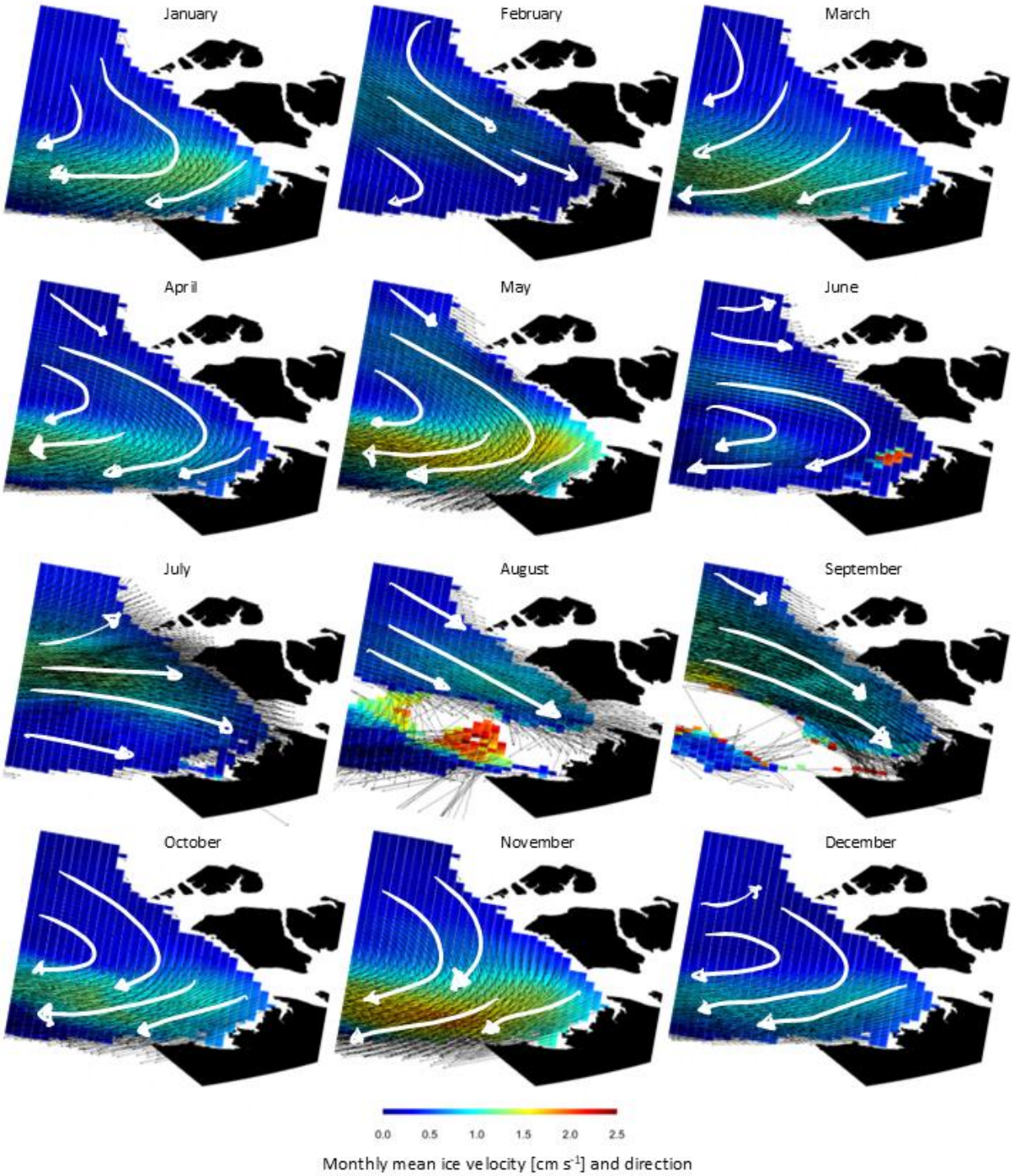



Figure 15. Monthly mean sea ice velocity (cm $s^{-1}$) and direction in 2018 in the Beaufort Sea and Amundsen Gulf.

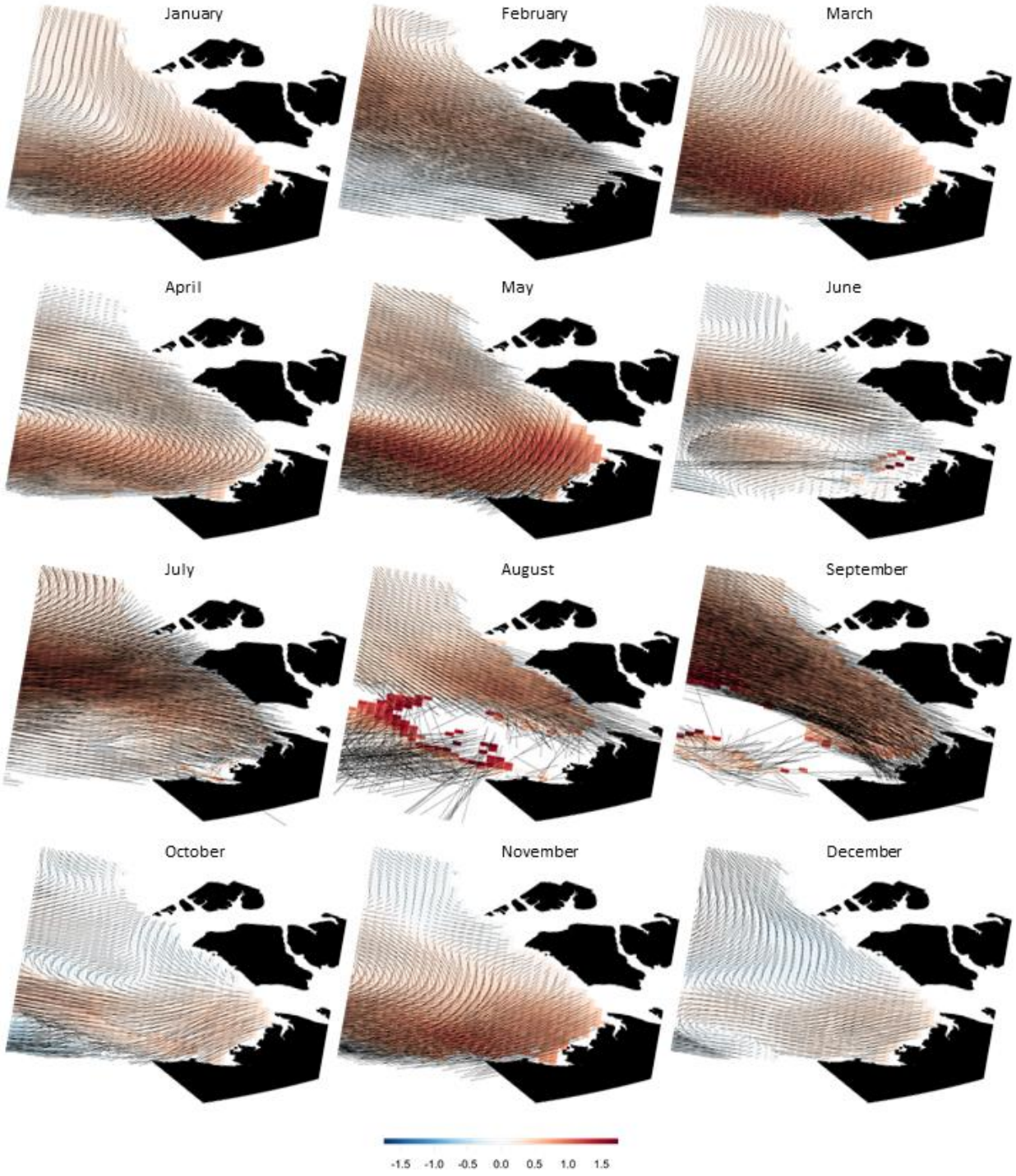



Figure 16. Monthly sea ice velocity (cm $s^{-1}$) and direction anomalies in 2018 from the climatological mean period 1983-2010 in the Beaufort Sea and Amundsen Gulf.

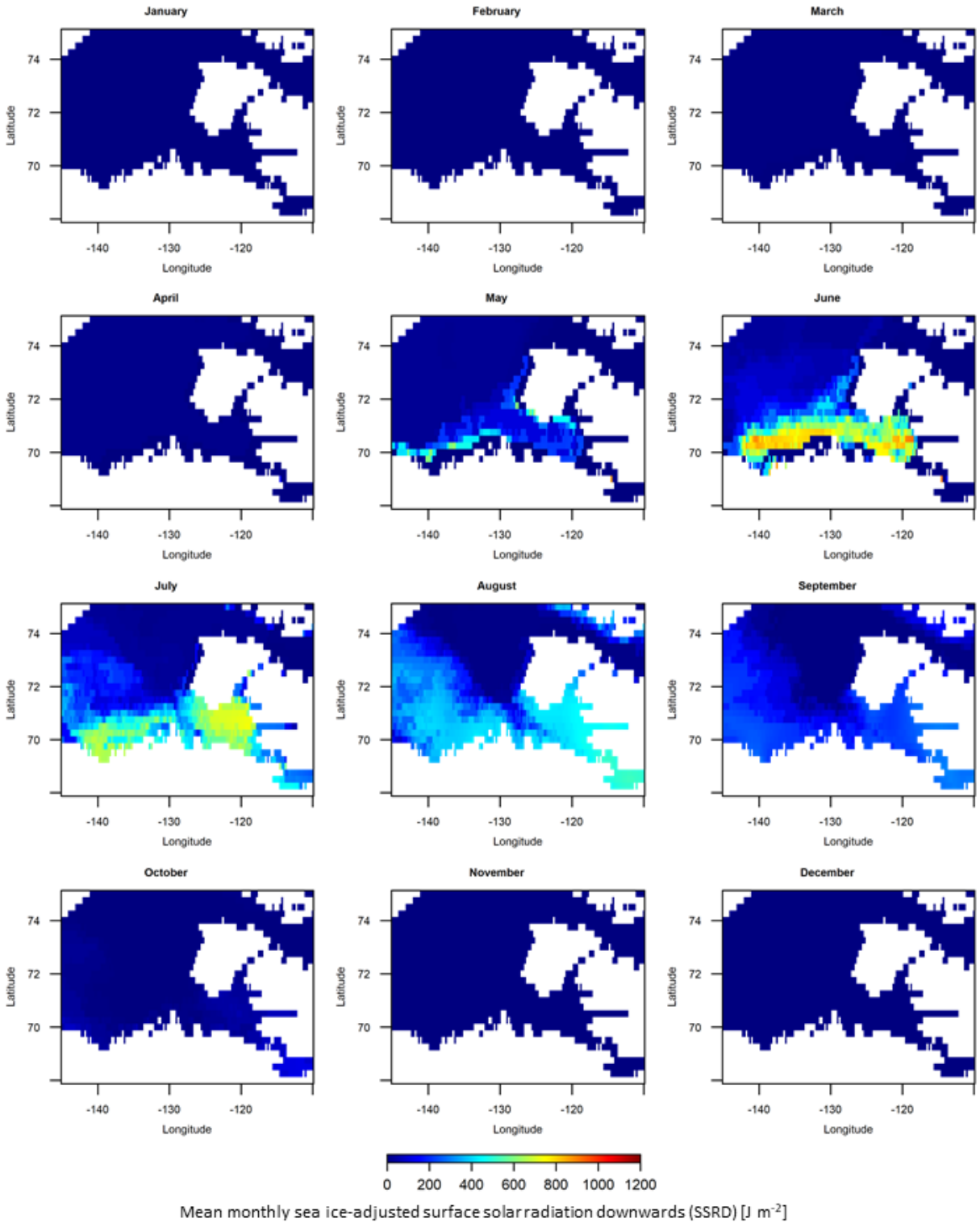



Figure 17. Mean monthly sea ice-adjusted surface solar radiation downwards (J $m^{-2}$) in 2018 in the Beaufort Sea and Amundsen Gulf.

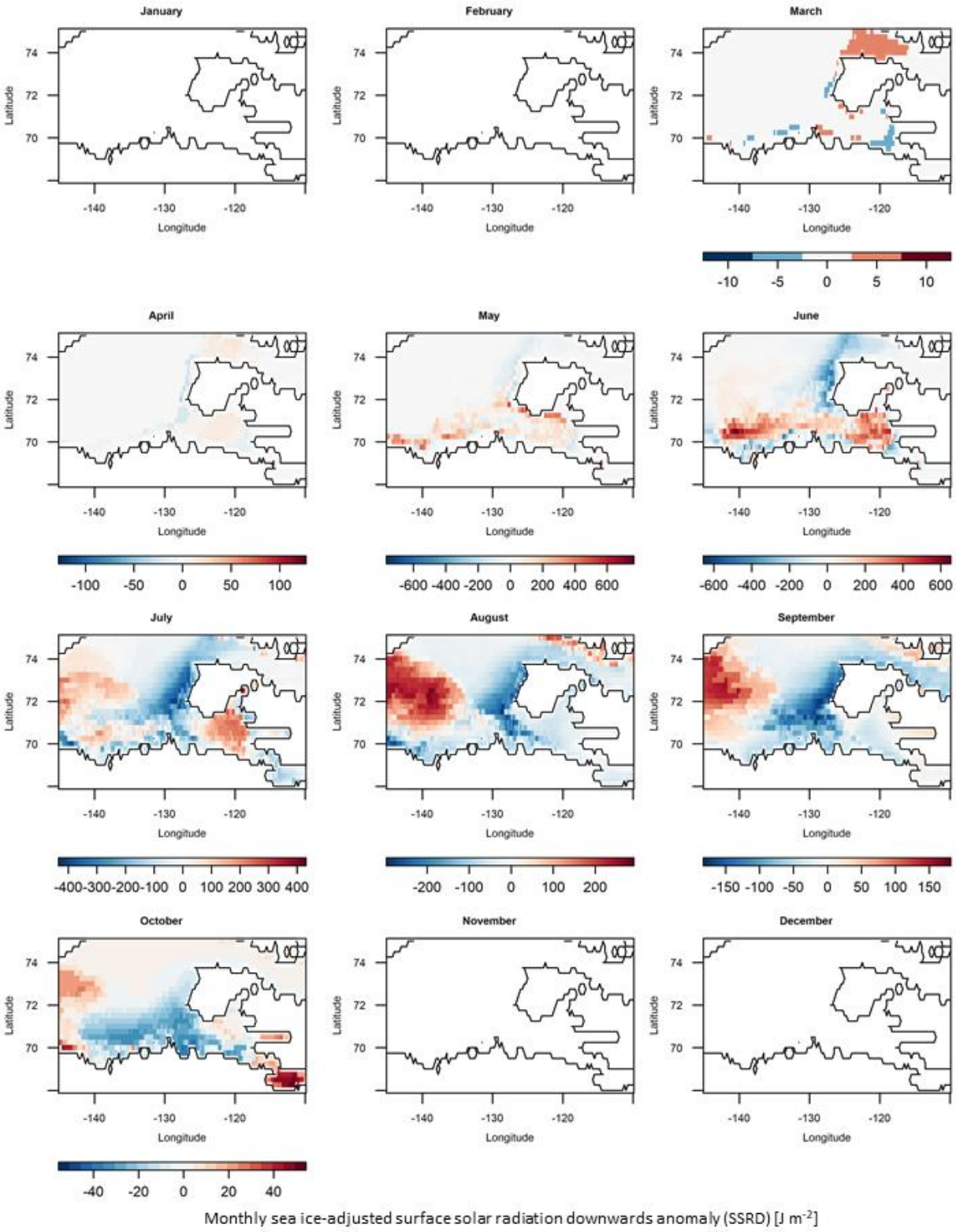



Figure 18. Monthly sea ice-adjusted surface solar radiation downwards anomalies (J $m^{-2}$) in 2018 compared to the climatological average period 1983-2010 in the Beaufort Sea and Amundsen Gulf.

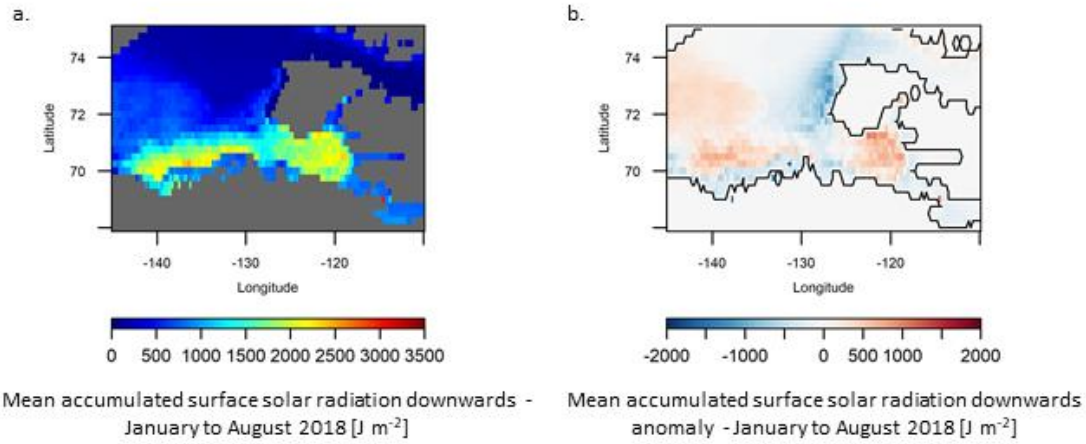



Figure 19. (a) Mean accumulated sea ice-adjusted surface solar radiation downwards (J $m^{-2}$) between January and August in 2018 (inclusive), and (b) accumulated sea ice-adjusted surface solar radiation downwards anomaly (J $m^{-2}$) between January and August 2018 (inclusive) compared to the climatological average over the period 1983-2010.

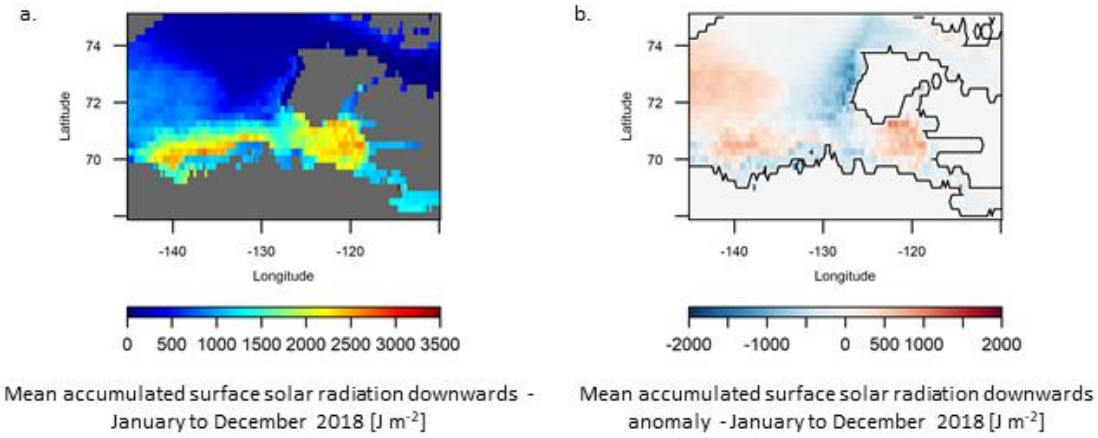



Figure 20. (a) Mean accumulated sea ice-adjusted surface solar radiation downwards (J $m^{-2}$) between January and December in 2018 (inclusive), and (b) accumulated sea ice-adjusted surface solar radiation downwards anomaly (J $m^{-2}$) between January and December 2018 (inclusive) compared to the climatological average over the period 1983-2010.

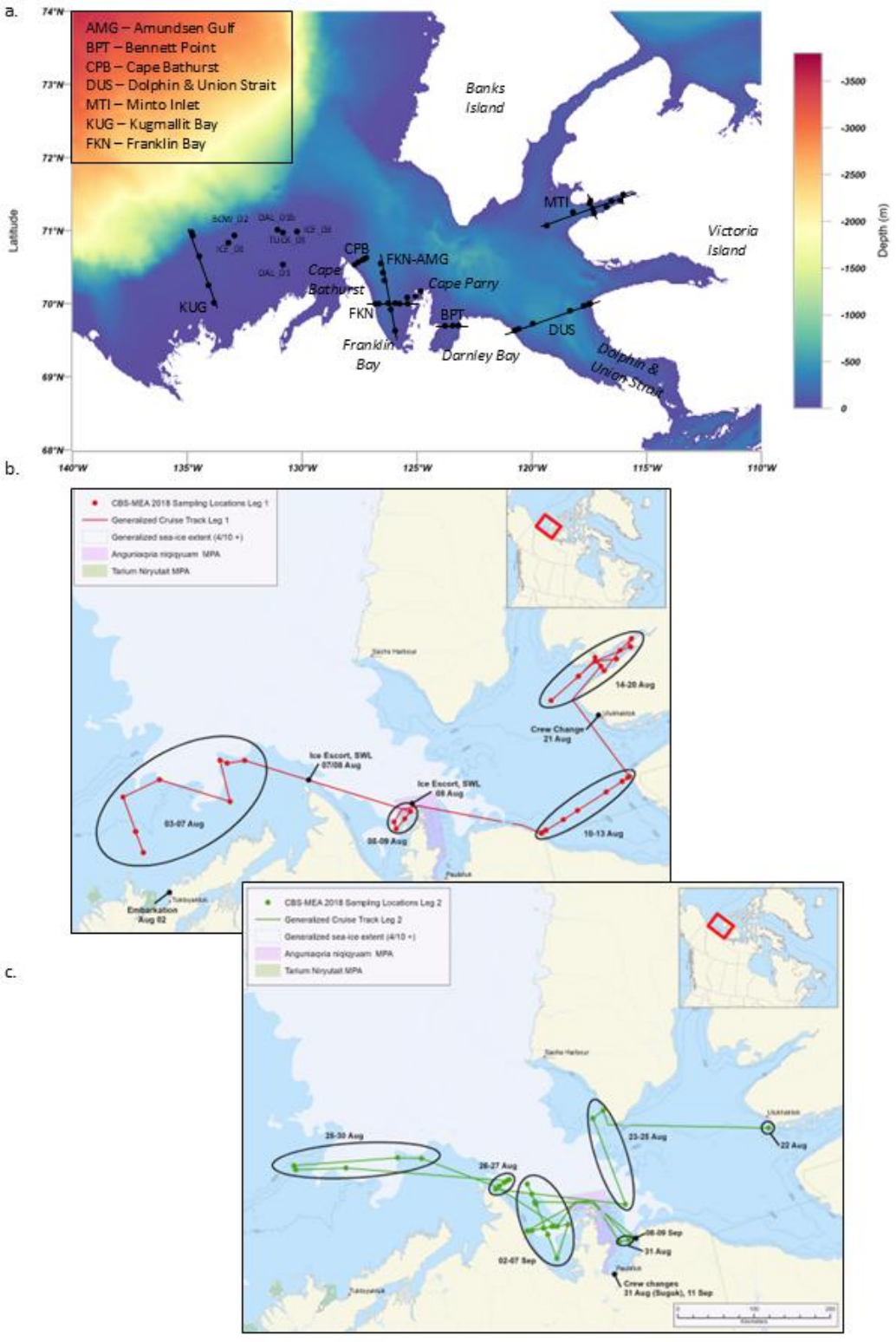



Figure 21. (a) CBS-MEA CTD station and section locations in the 2018 study region, overlain on ETOPO1 bathymetry data, (b) leg 1 stations and generalized ice conditions, (c) leg 2 stations and generalized ice conditions..

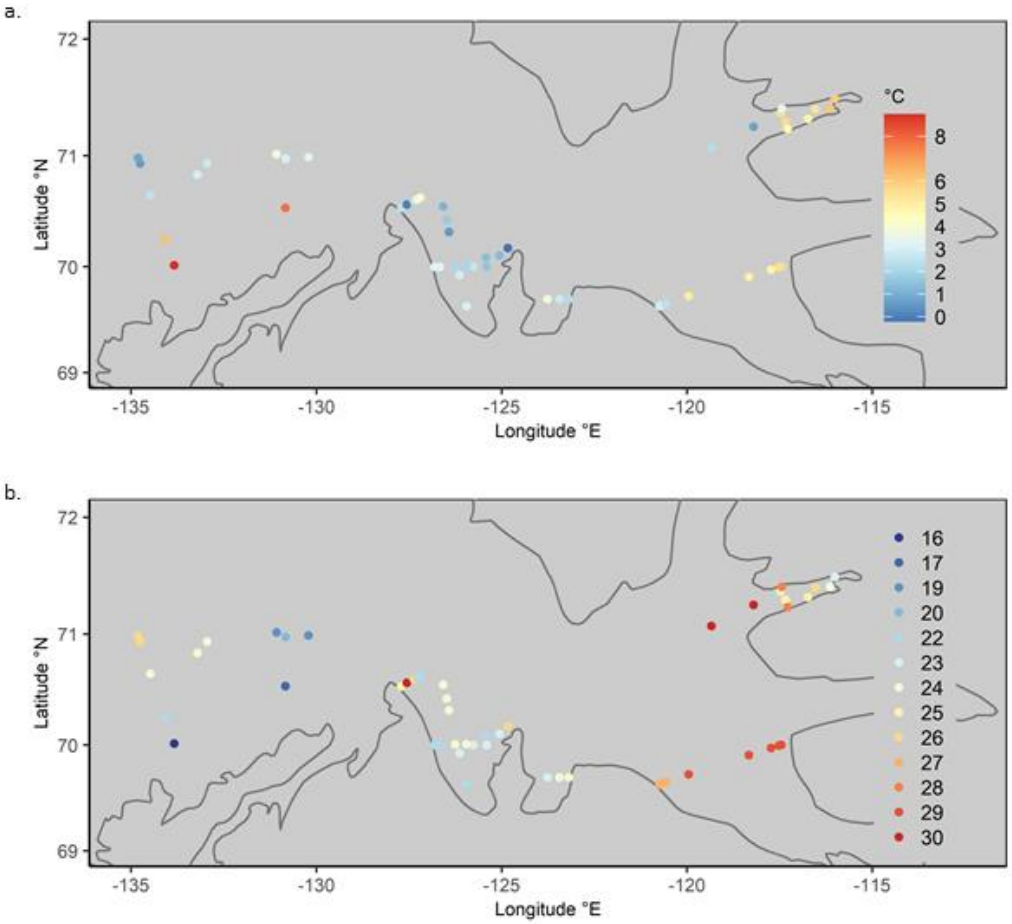



Figure 22. (a) Surface temperature (°C), and (b) surface salinity at each CBS-MEA station in 2018.

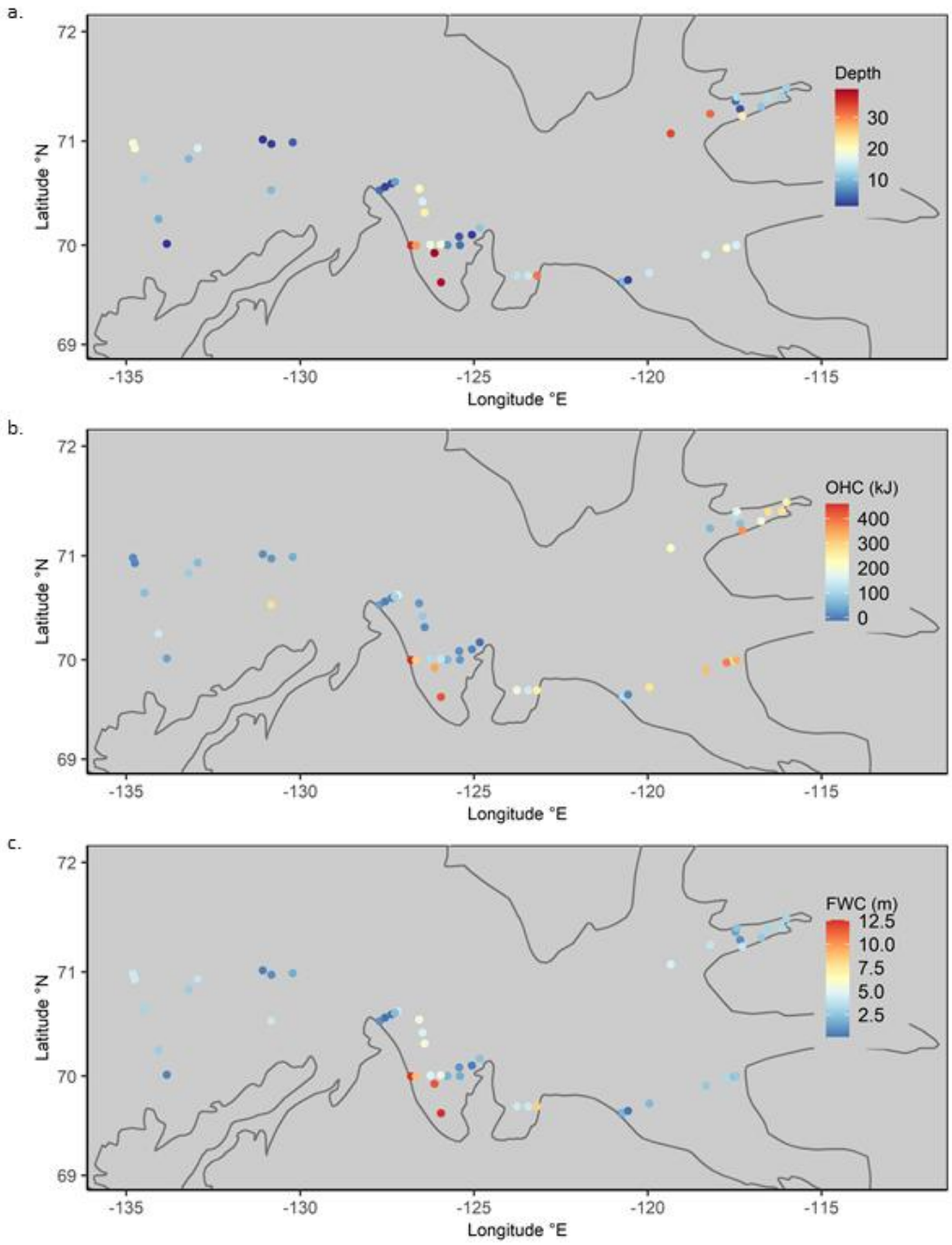



Figure 23. (a) Depth of the maximum $N^2$ in meters, (b) Integrated ocean heat content (OHC) relative to 0°C above the depth of the $N^2$ max (kJ), and (c) Freshwater content (FWC) relative to S = 34.8 integrated above the depth of the $N^2$ maximum; at each CBS-MEA station in 2018.

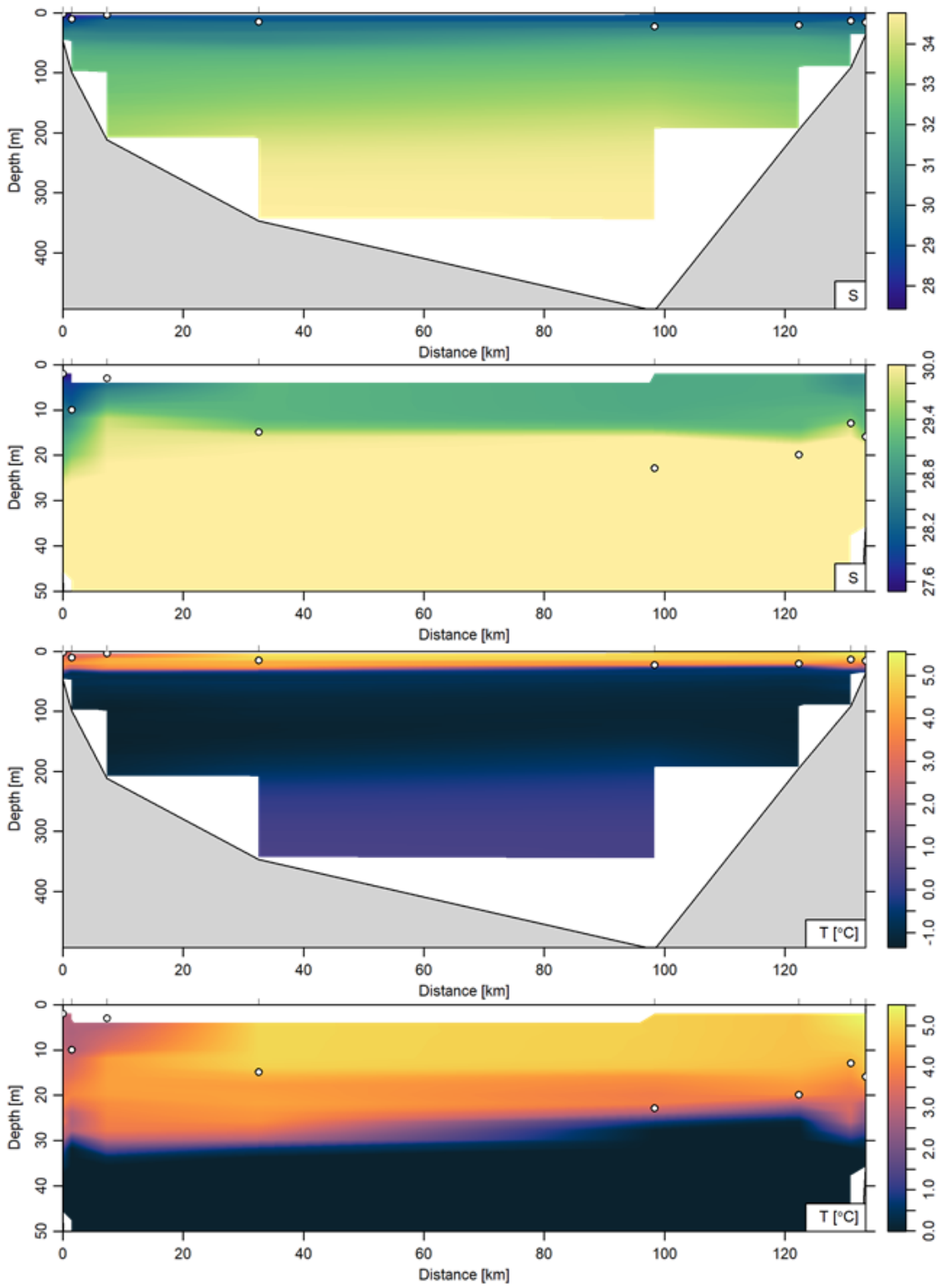



Figure 24. Sections from west to east across Dolphin and Union Strait in 2018: salinity (a, b) and temperature (c, d). Full depth is shown in (a, c) and enlarged to show only the top 50 m in (b, d). $N^2$-derived surface layer depths at each station are denoted by white dots.

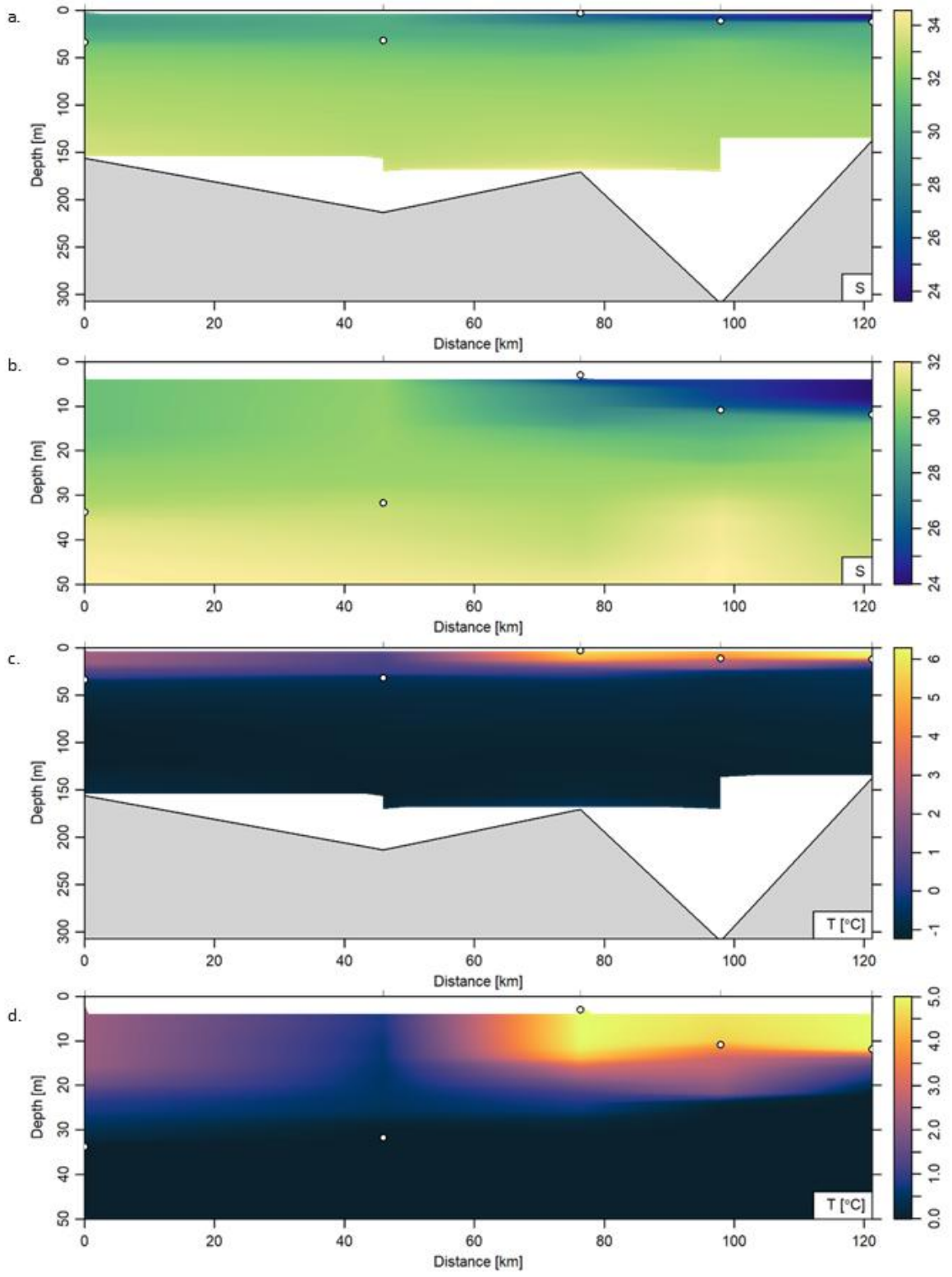



Figure 25. Sections from west to east along Minto Inlet in 2018: salinity (a, b) and temperature (c, d). Full depth (a, c) and enlarged to show only the top 50 m (b, d). $N^2$-derived surface layer depths at each station are denoted by white dots.

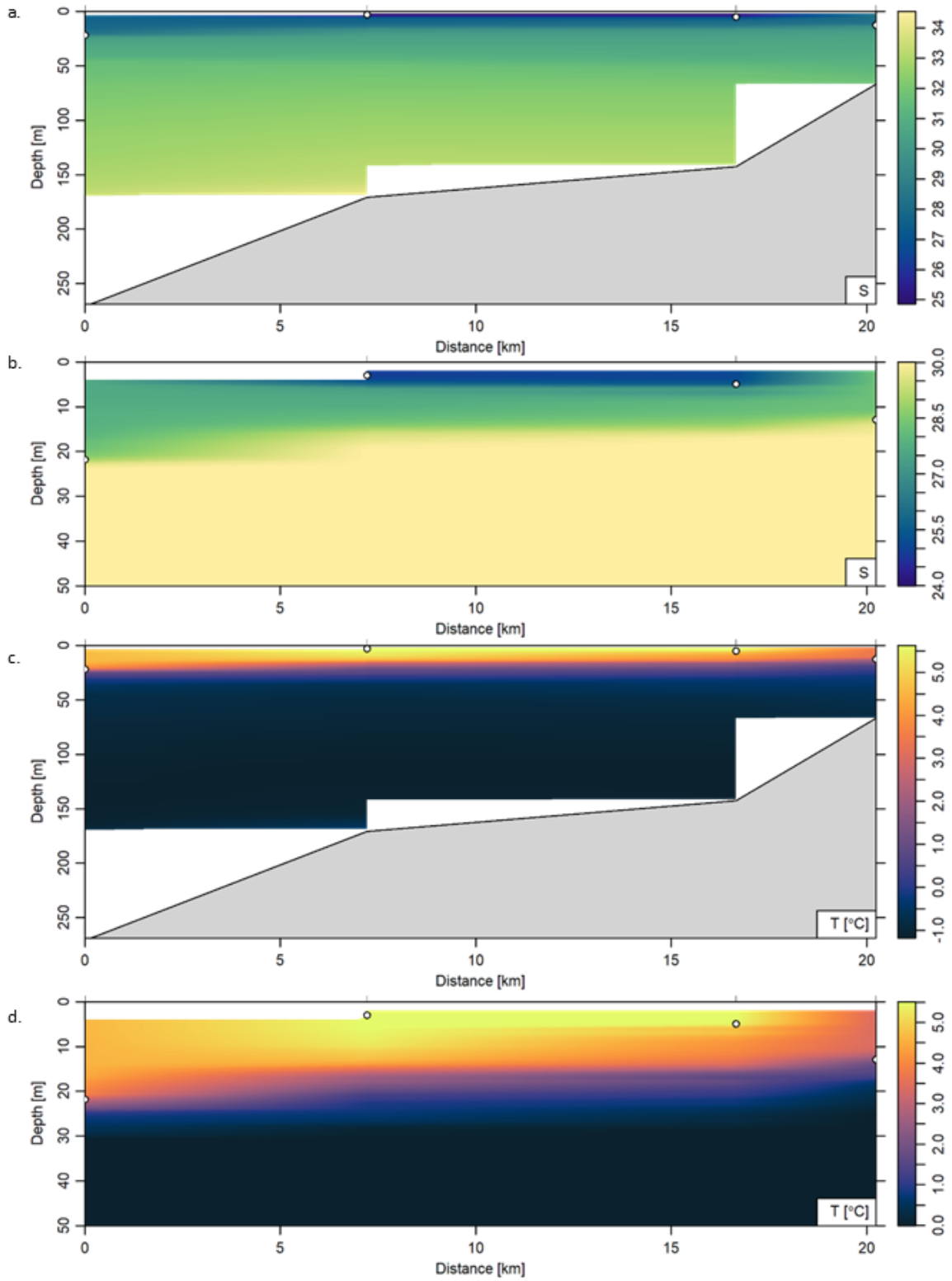



Figure 26. Sections from south to north across Minto Inlet in 2018: salinity (a, b) and temperature (c, d). Full depth (a, c) and enlarged to show only the top 50 m (b, d). $N^2$-derived surface layer depths at each station are denoted by white dots.

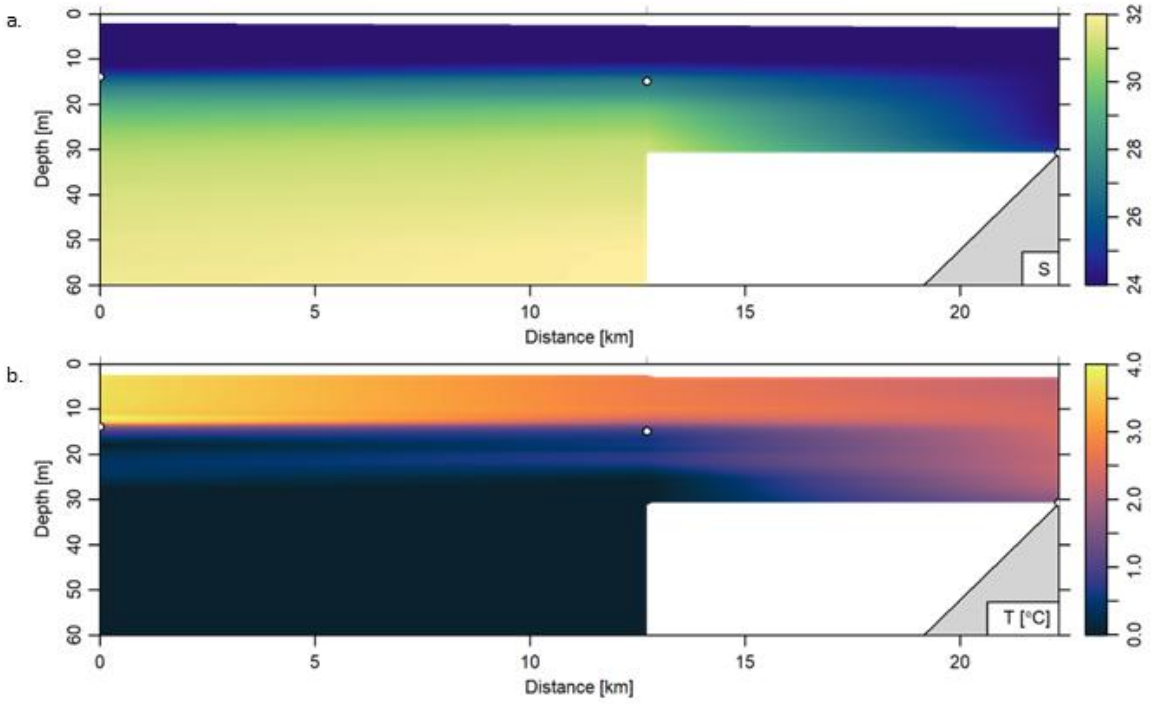



Figure 27. Sections from west to east across Darnley Bay using the Bennett Point (BPT) stations in 2018: salinity (top) and temperature (bottom). $N^2$-derived surface layer depths at each station are denoted by white dots.

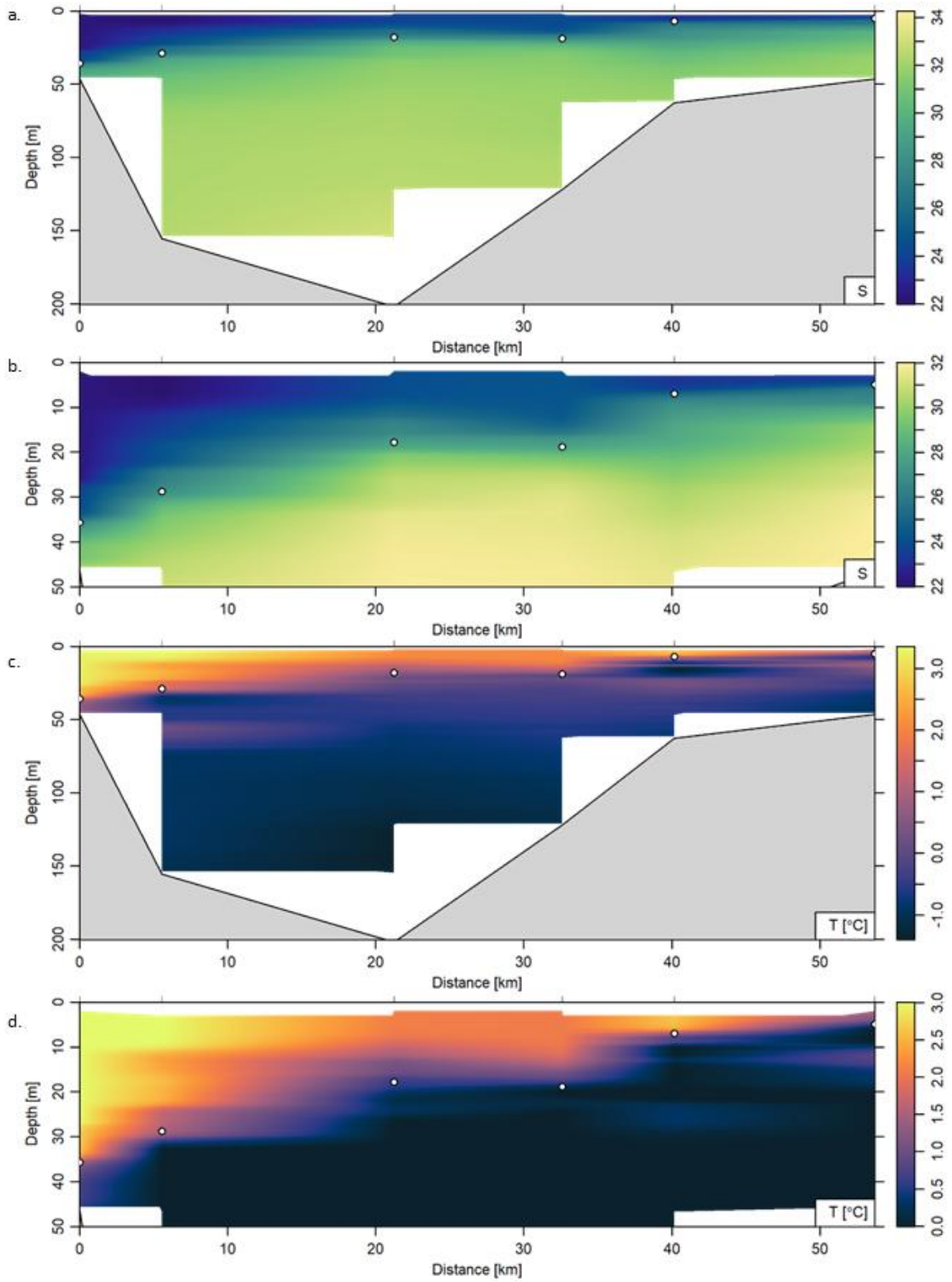



Figure 28. Sections from west to east across Franklin Bay in 2018: salinity (a, b) and temperature (c, d). Full depth (a, c) and enlarged to show only the top 50 m (b, d). $N^2$-derived surface layer depths at each station are denoted by white dots.

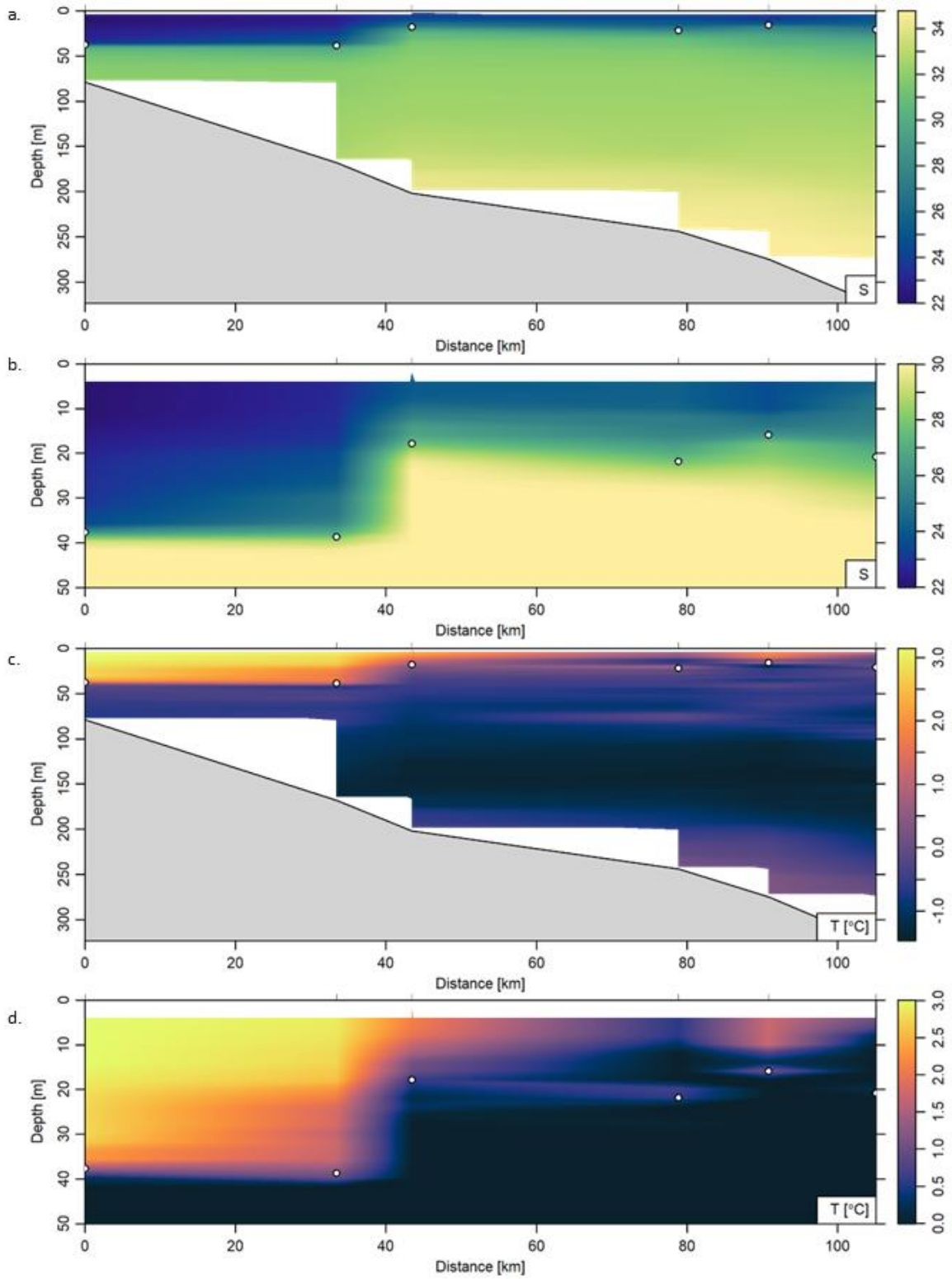



Figure 29. Sections from south to north across Franklin Bay and southern Amundsen Gulf in 2018: salinity (a, b) and temperature (c, d). Full depth (a, c) and enlarged to show only the top 50 m (b, d). $N^2$-derived surface layer depths at each station are denoted by white dots.

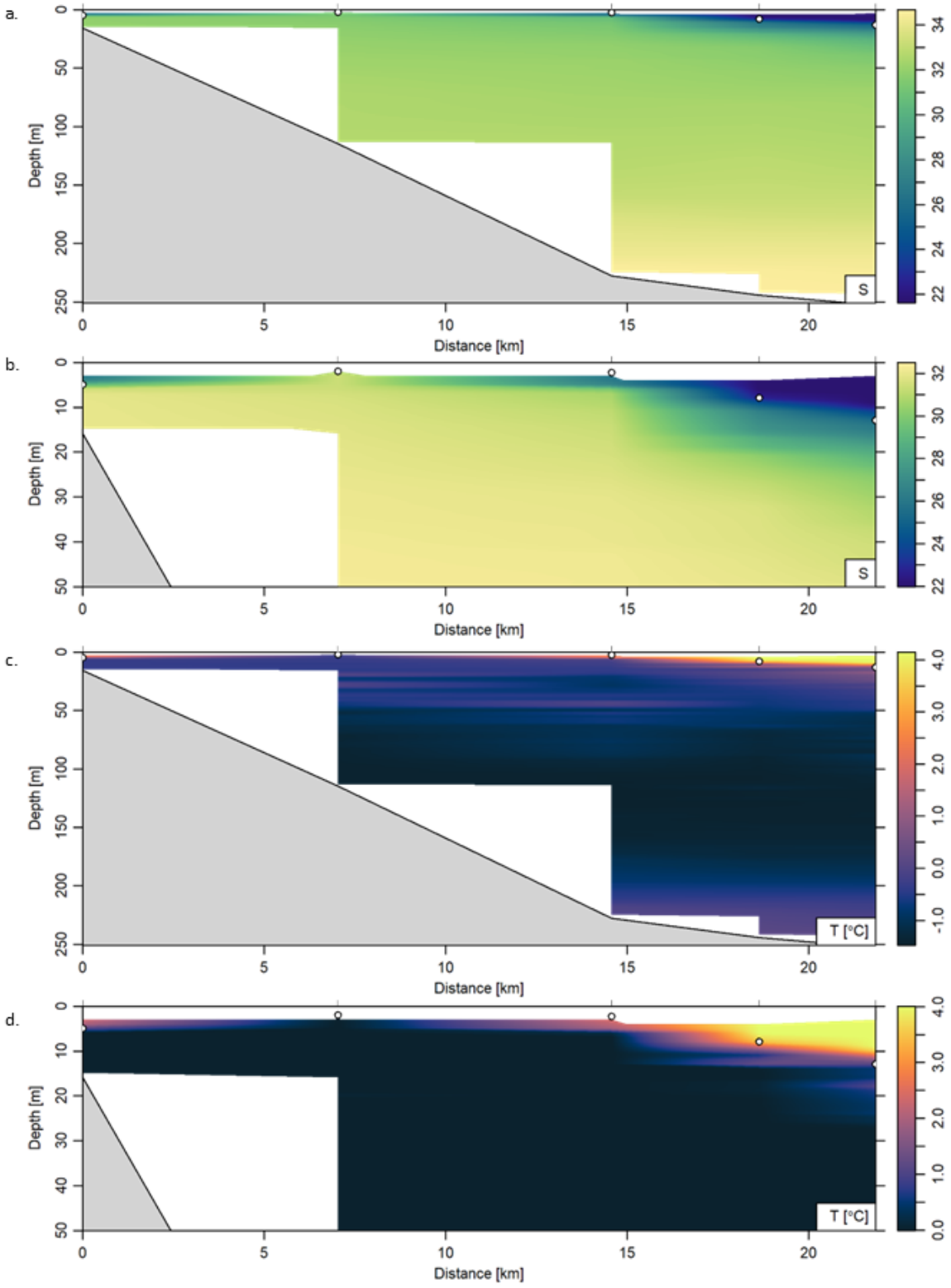



Figure 30. Sections from south to north using the Cape Bathurst (CPB) stations in 2018: salinity (a, b) and temperature (c, d). Full depth (a, c) and enlarged to show only the top 50 m (b, d). $N^2$-derived surface layer depths at each station are denoted by white dots.

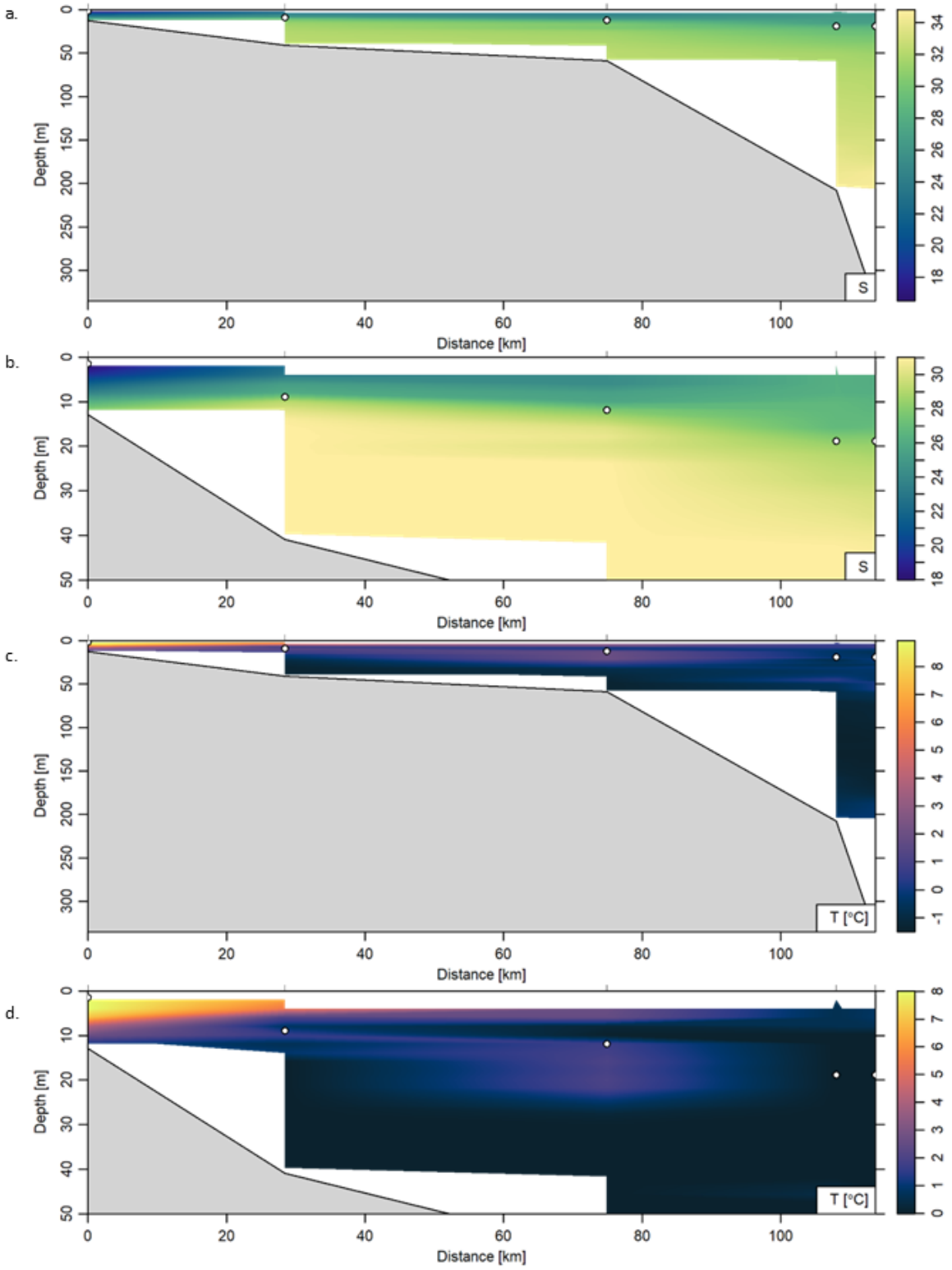



Figure 31. Sections from south to north using the Kugmallit Bay (KUG) stations in 2018: salinity (a, b) and temperature (c, d). Full depth (a, c) and enlarged to show only the top 50 m (b, d). $N^2$-derived surface layer depths at each station are denoted by white dots.

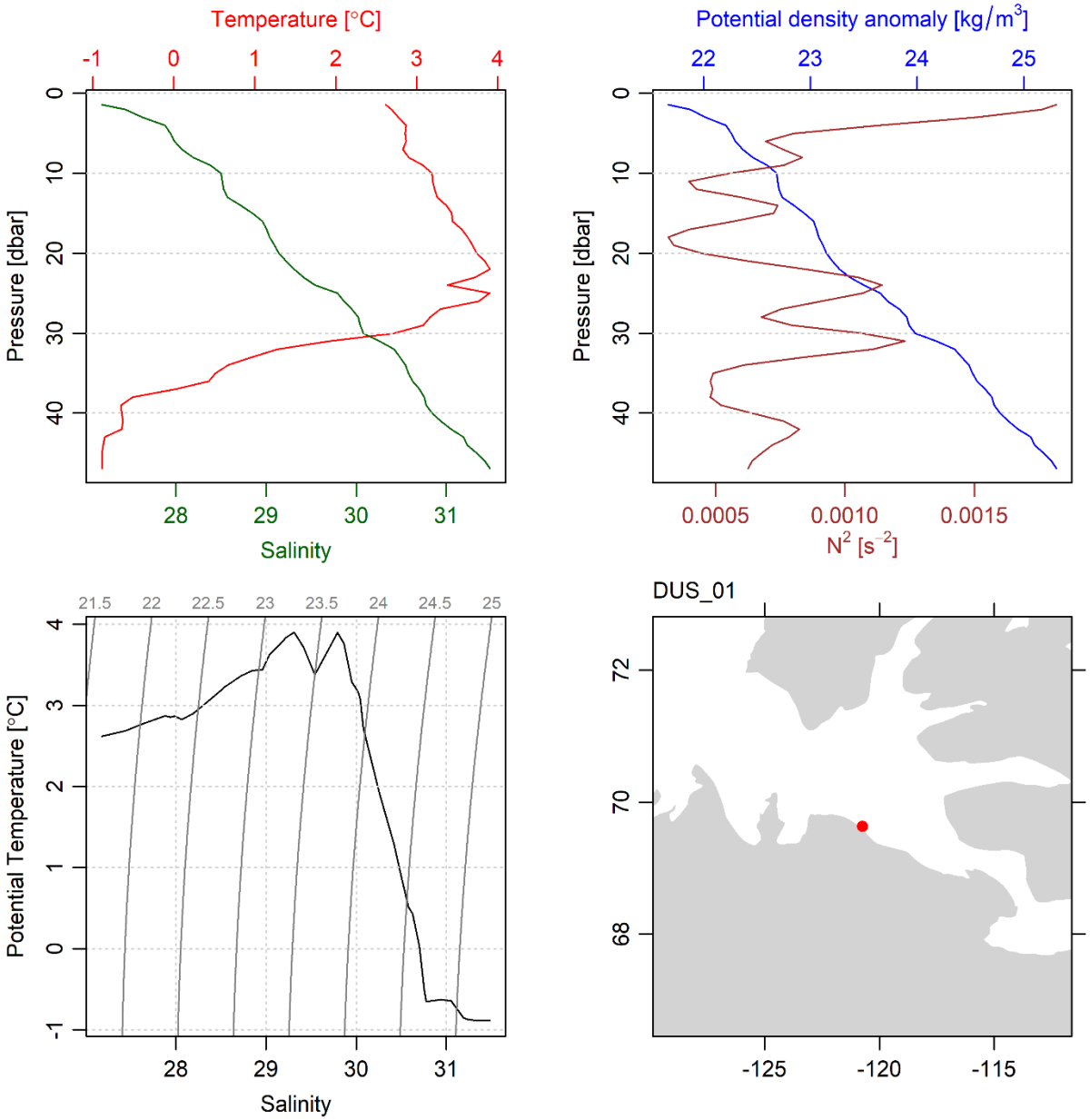
## 8 Tables

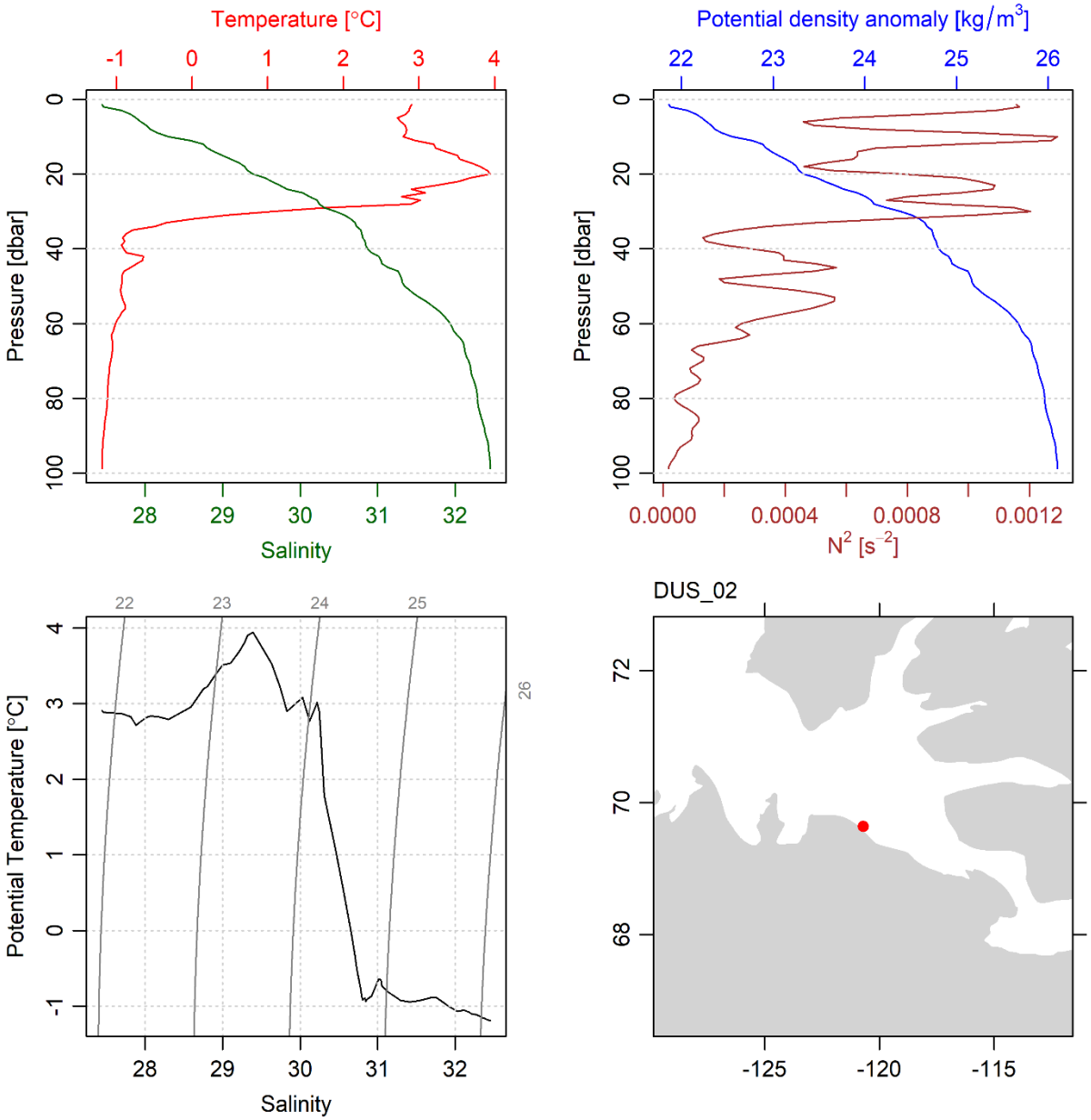
Table 1. Surface and surface layer oceanographic parameters at each CBS-MEA station, August-September 2018. Freshwater content (FWC) and ocean heat content (OHC) is integrated over the surface layer depth.

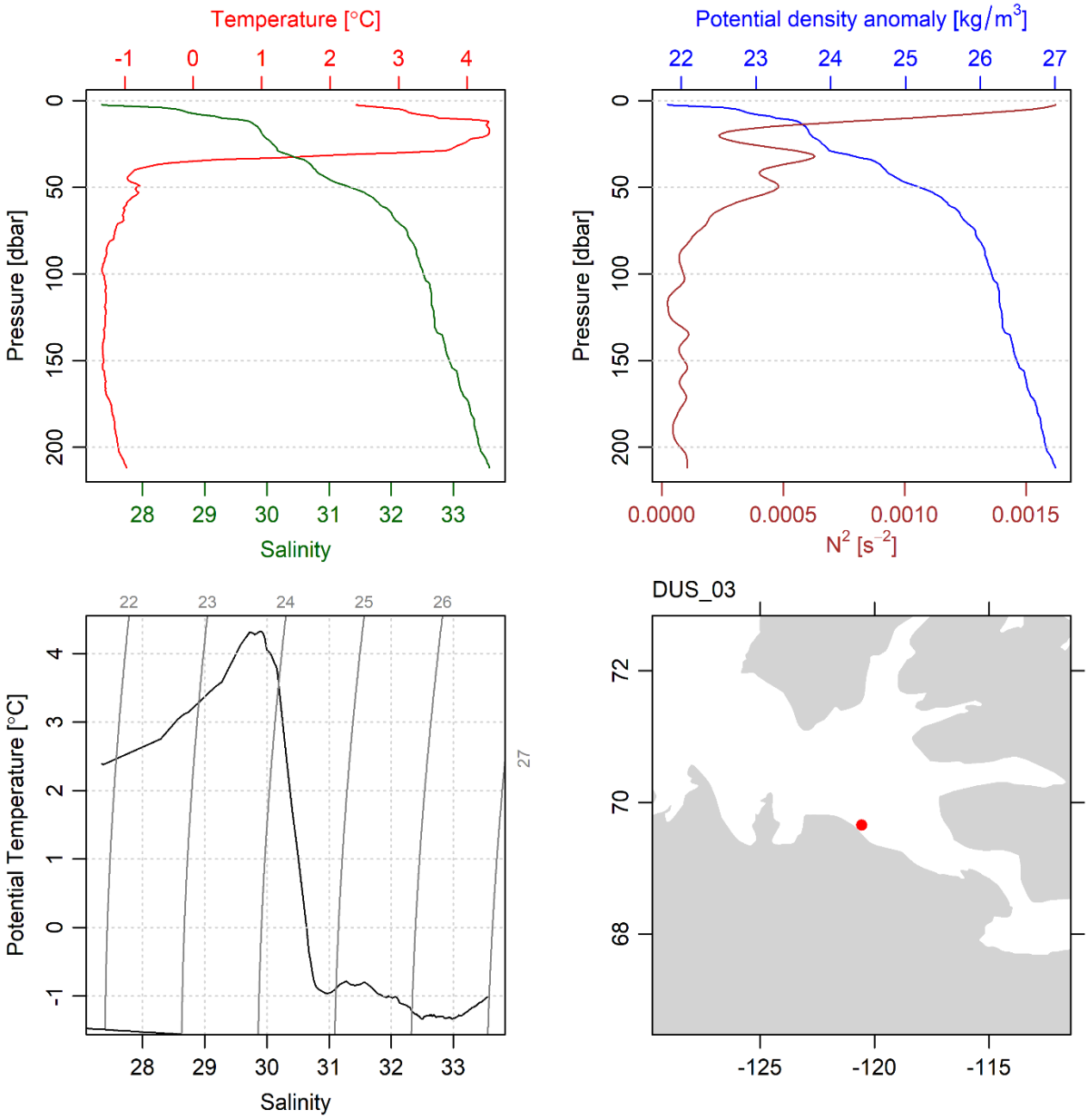
| Station | Lat (°N) | Lon (°N) | Surface Temp (°C) | Surface Salinity | Surface depth (dbar) | Surface Layer (dbar) | OHC (kJ) | FWC (m) | Station Depth |
|---|---|---|---|---|---|---|---|---|---|
| DUS_01 | 69.63 | -120.75 | 2.62 | 27.17 | 1.4 | 1.4 | 10.92 | 0.22 | 51 |
| DUS_02 | 69.64 | -120.72 | 2.91 | 27.44 | 1.4 | 10 | 117.61 | 1.99 | 102 |
| DUS_03 | 69.65 | -120.57 | 2.39 | 27.34 | 2.2 | 2.2 | 9.99 | 0.21 | 217 |
| DUS_04 | 69.73 | -119.96 | 5.05 | 29.13 | 2.8 | 14.9 | 270.26 | 2.09 | 353 |
| DUS_07 | 69.91 | -118.33 | 4.94 | 28.98 | 1.4 | 16 | 322.40 | 2.61 | 501 |
| DUS_09 | 69.97 | -117.73 | 4.81 | 29.03 | 1.4 | 20 | 385.13 | 3.17 | 203 |
| DUS_10 | 69.99 | -117.52 | 5.39 | 28.68 | 1.4 | 13 | 270.40 | 2.18 | 106 |
| DUS_11 | 70.00 | -117.46 | 5.55 | 28.72 | 1.4 | 16 | 336.34 | 2.67 | 41 |
| MTI_01 | 71.07 | -119.35 | 2.31 | 29.63 | 2 | 34 | 211.46 | 4.54 | 167 |
| MTI_02 | 71.25 | -118.21 | 0.73 | 30.35 | 2.2 | 32 | 60.33 | 3.87 | 223 |
| MTI_03 | 71.37 | -117.48 | 5.58 | 25.16 | 1.2 | 5 | 115.45 | 1.38 | 141.3 |
| MTI_04 | 71.30 | -117.35 | 5.59 | 24.88 | 1.3 | 3 | 69.76 | 0.86 | 173 |
| MTI_05 | 71.24 | -117.28 | 4.62 | 27.66 | 3.1 | 22 | 365.34 | 3.95 | 282 |
| MTI_06 | 71.40 | -116.54 | 5.39 | 26.21 | 1.5 | 13.1 | 283.34 | 3.07 | 201 |
| MTI_HC_0 | 71.32 | -116.74 | 4.72 | 25.15 | 2.1 | 10.9 | 191.97 | 2.67 | 313 |
| BIN_01 | 71.41 | -117.45 | 3.38 | 28.25 | 1.1 | 13 | 175.57 | 2.40 | 68 |
| MTI_07 | 71.41 | -116.14 | 6.13 | 23.67 | 2.3 | 12 | 274.04 | 3.31 | 145 |
| MTI_08 | 71.50 | -116.02 | 5.97 | 22.75 | 2.1 | 12 | 250.76 | 3.10 | 170 |
| BPT_01b | 69.70 | -123.77 | 3.75 | 23.19 | 2 | 13.9 | 195.20 | 4.17 | 75 |
| BPT_03 | 69.70 | -123.44 | 2.77 | 23.78 | 2.1 | 15 | 143.90 | 4.16 | 118.5 |
| BPT_05 | 69.70 | -123.19 | 2.23 | 23.67 | 3 | 31 | 252.37 | 8.38 | 41 |
| FKN_06 | 70.00 | -125.40 | 1.57 | 22.73 | 1.3 | 5 | 25.61 | 1.63 | 51 |
| FKN_05 | 70.00 | -125.76 | 2.60 | 23.25 | 2.4 | 7 | 60.01 | 1.93 | 75 |
| FKN_01 | 70.00 | -126.81 | 3.25 | 22.29 | 1.5 | 36 | 457.87 | 12.40 | 51 |
| FKN_02 | 70.00 | -126.67 | 3.35 | 22.00 | 2.1 | 29 | 298.61 | 8.87 | 163 |
| FKN_03 | 70.01 | -126.25 | 2.09 | 24.01 | 1.9 | 18 | 112.37 | 4.67 | 213 |
| FKN_04 | 70.01 | -125.96 | 2.05 | 24.26 | 1.3 | 19 | 133.52 | 5.36 | 136 |
| FKN_07 | 69.63 | -125.95 | 3.10 | 22.02 | 2.9 | 38 | 423.49 | 12.53 | 83 |
| FEX_HC01 | 69.92 | -126.14 | 2.91 | 22.70 | 3 | 39 | 347.26 | 11.61 | 174 |
| AMG_06 | 70.55 | -126.58 | 1.12 | 24.39 | 2.2 | 21 | 22.84 | 5.38 | 329 |
| AMG_05 | 70.42 | -126.48 | 1.72 | 23.58 | 2.1 | 15.9 | 83.93 | 4.59 | 281 |
| AMG_04 | 70.32 | -126.42 | 0.53 | 24.19 | 2.3 | 22 | 11.41 | 5.75 | 250 |
| CPB_01 | 70.53 | -127.72 | 2.41 | 25.40 | 2.3 | 5 | 32.57 | 0.92 | 22 |
| CPB_02 | 70.57 | -127.56 | 0.02 | 30.85 | 2 | 2 | 0.15 | 0.11 | 119 |
| CPB_03 | 70.60 | -127.37 | 2.40 | 25.85 | 2.2 | 2.2 | 10.06 | 0.26 | 238 |
| CPB_04 | 70.63 | -127.20 | 4.14 | 21.73 | 2 | 13 | 176.76 | 4.24 | 262 |
| CPB_HC01 | 70.61 | -127.28 | 4.14 | 21.64 | 3.2 | 8 | 99.52 | 2.22 | 252 |
| KUG_01 | 70.01 | -133.84 | 8.97 | 15.82 | 1.4 | 1.4 | 37.49 | 0.55 | 24 |
| KUG_01b | 70.25 | -134.08 | 6.28 | 22.11 | 1.4 | 8.9 | 138.29 | 2.75 | 44 |
| KUG_01c | 70.65 | -134.48 | 2.54 | 24.15 | 2.1 | 12 | 68.74 | 3.06 | 61 |
| KUG_03 | 70.93 | -134.76 | 0.58 | 26.24 | 2 | 19 | 5.66 | 4.19 | 210 |
| KUG_04 | 70.98 | -134.81 | 0.80 | 26.09 | 2.4 | 19 | 8.31 | 4.24 | 346 |
| DAL_01 | 70.54 | -130.84 | 7.81 | 17.39 | 1.3 | 10 | 282.42 | 3.99 | 24 |
| DAL_01b | 71.01 | -131.07 | 3.83 | 18.99 | 1.4 | 1.4 | 16.07 | 0.45 | 56 |
| FRK_06 | 70.09 | -125.43 | 1.42 | 22.38 | 1.4 | 3.2 | 15.45 | 1.02 | 83 |
| ICE_01 | 70.83 | -133.21 | 3.01 | 24.50 | 1.5 | 9.9 | 86.70 | 2.80 | 66 |
| ICE_03 | 70.99 | -130.21 | 3.25 | 19.23 | 1.4 | 4 | 47.49 | 1.67 | 43 |
| TUCK_01 | 70.97 | -130.83 | 3.06 | 19.59 | 1.3 | 2 | 24.31 | 0.85 | 47 |
| BOW_02 | 70.93 | -132.95 | 2.74 | 23.73 | 2.4 | 16 | 64.32 | 3.90 | 67 |
| WIS_02 | 70.17 | -124.83 | -0.22 | 25.53 | 2.2 | 11 | -13.05 | 2.39 | 48 |
| WIS_01 | 70.10 | -125.06 | 1.34 | 22.74 | 1.9 | 1.9 | 5.70 | 0.35 | 55 |

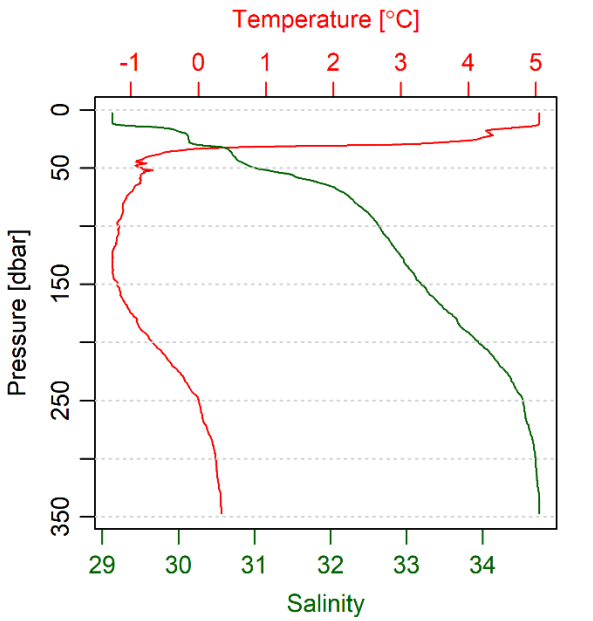
## Appendix A – Profiles and Maps

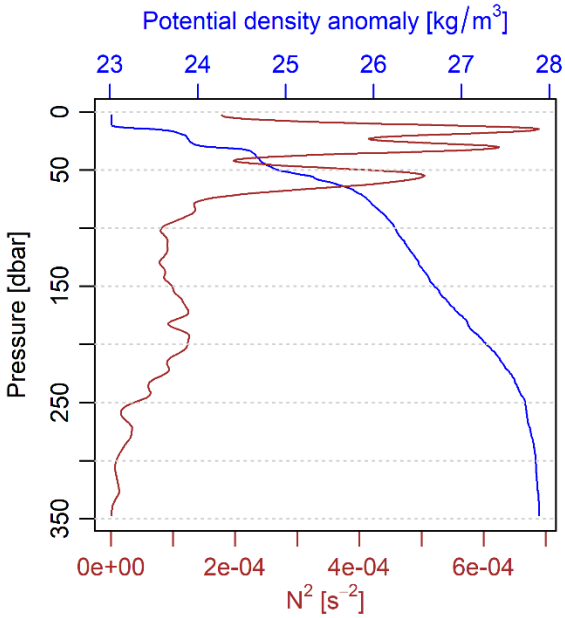
Salinity, temperature, potential density anomaly, and $N^2$, and T-S plots for each of the stations sampled during CBS-MEA 2018. Station name is indicated with the map, showing the station location as described in Figure 21 and Table 1.

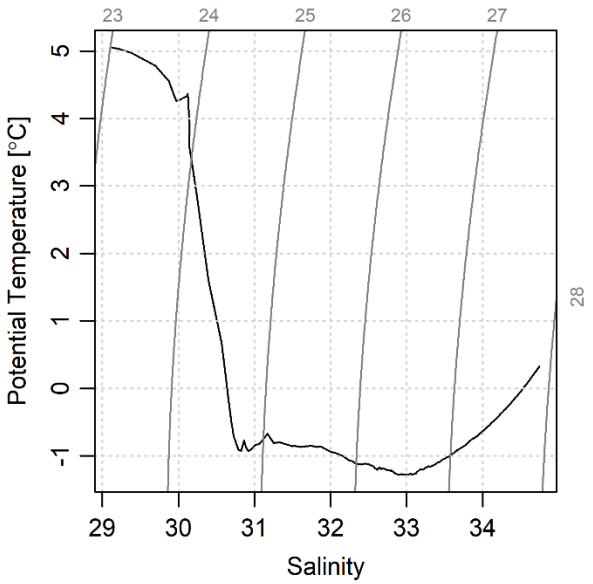


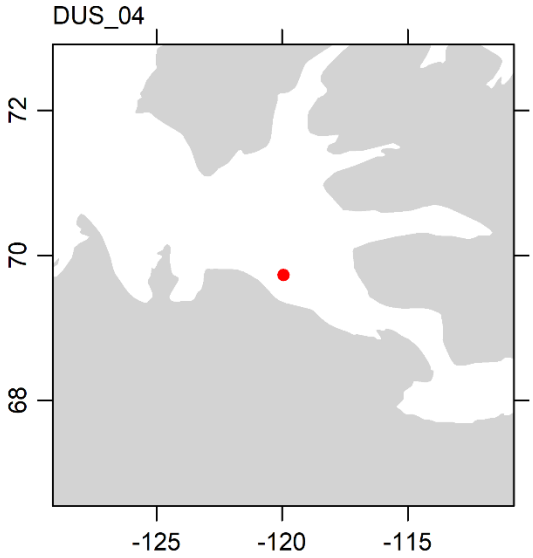

Temperature [°C]
-1
0
1
2
3
4
Pressure [dbar]
0
20
40
60
80
100
28
29
30
31
32
Salinity
Potential density anomaly [kg/m3]
22
23
24
25
26
0.0000
0.0004
0.0008
0.0012
N2 [s−2]
Potential Temperature [°C]
-1
0
1
2
3
4
26
DUS_02
72
70
68
-125
-120
-115

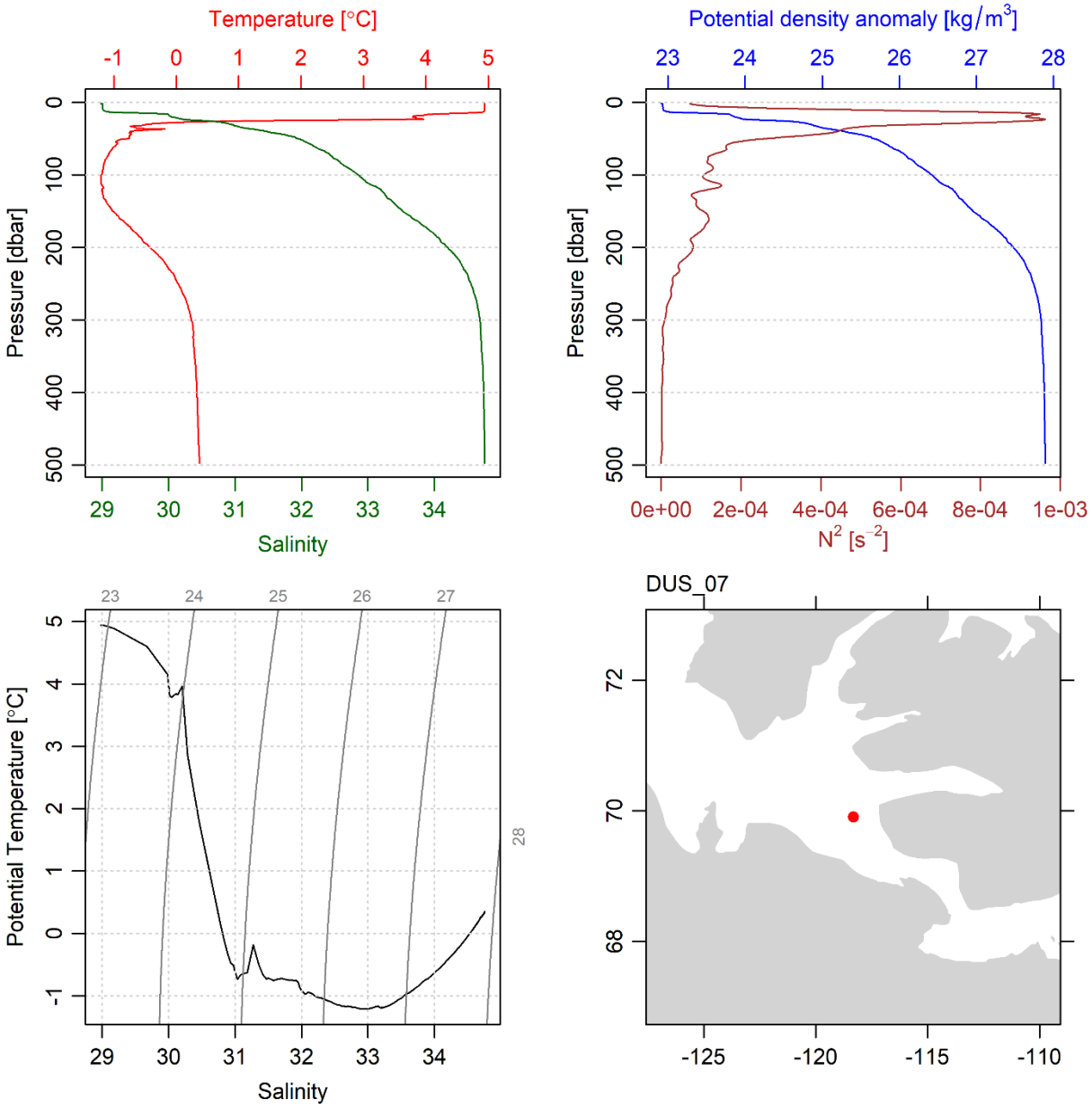

Temperature [°C]
-1
0
1
2
3
4
Pressure [dbar]
0
50
100
150
200
28
29
30
31
32
33
Salinity
Potential density anomaly [kg/m3]
22
23
24
25
26
27
0.0000
0.0005
0.0010
0.0015
N2 [s−2]
Potential Temperature [°C]
22
23
24
25
26
27
DUS_03
72
70
68
-125
-120
-115

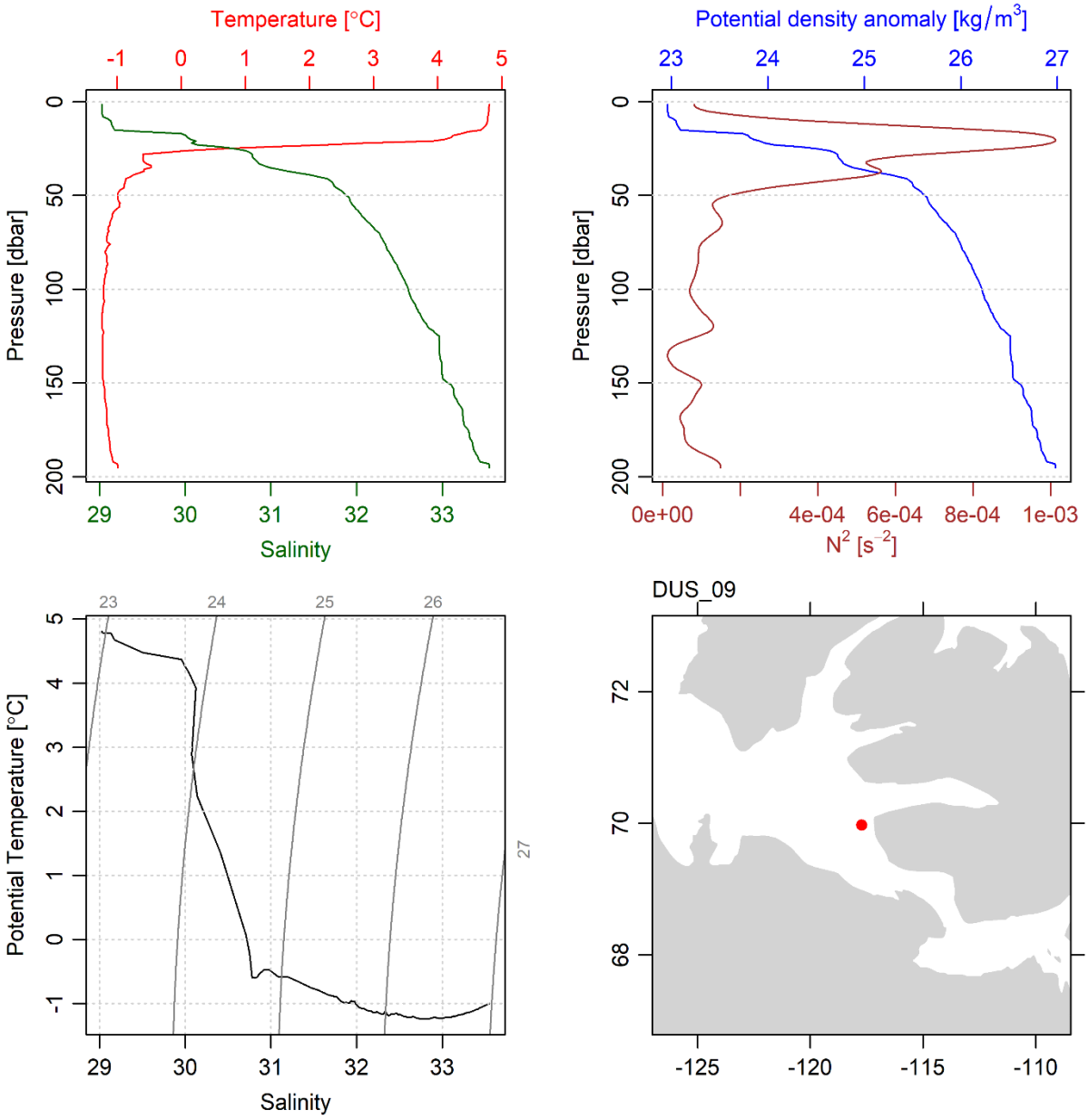

Temperature [°C]
-1
0
1
2
3
4
5
Pressure [dbar]
0
50
150
250
350
29
30
31
32
33
34
Salinity

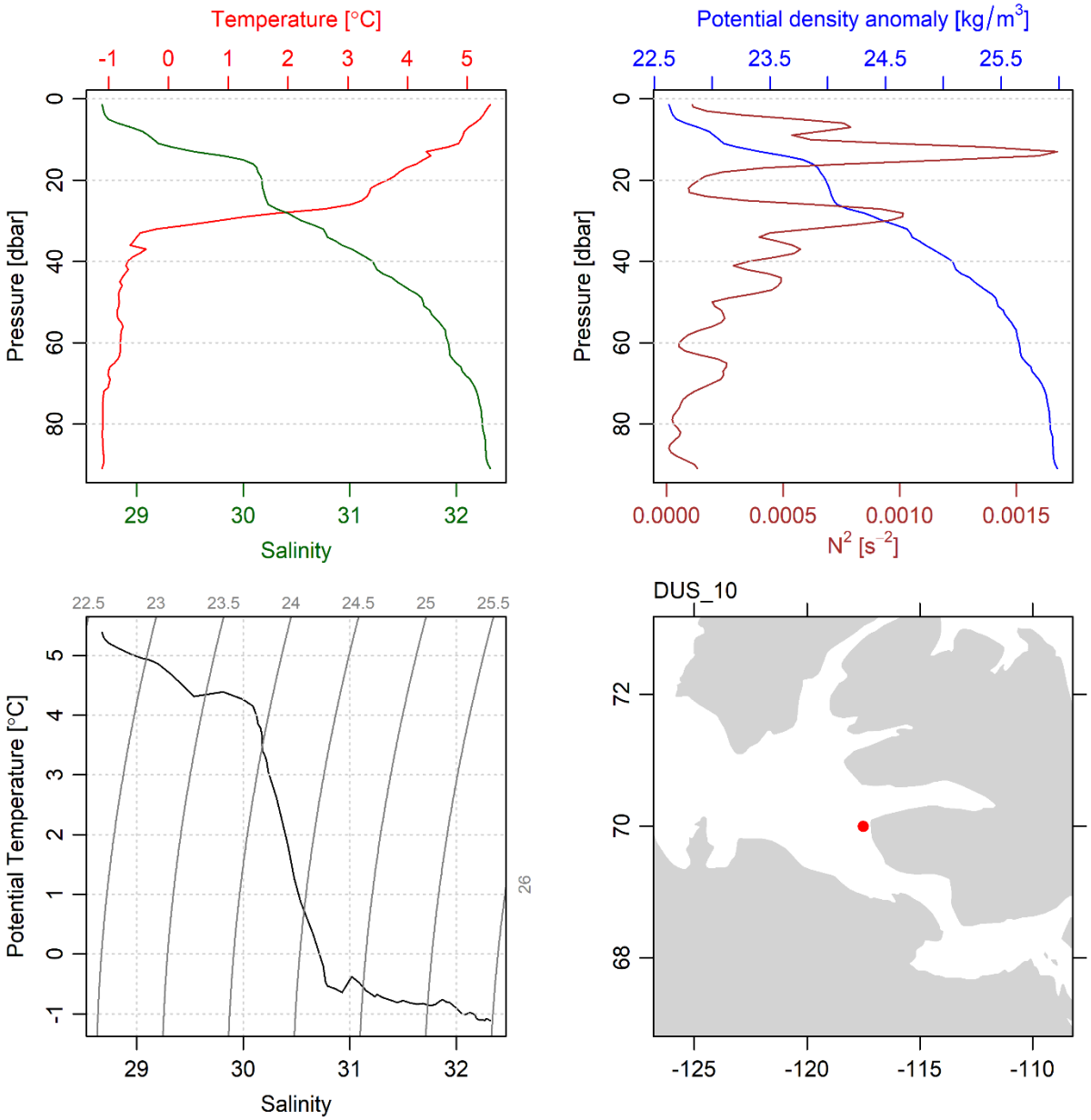

Potential density anomaly [kg/m3]
23
24
25
26
27
28
Pressure [dbar]
0
50
150
250
350
0e+00
2e-04
4e-04
6e-04
N2 [s−2]

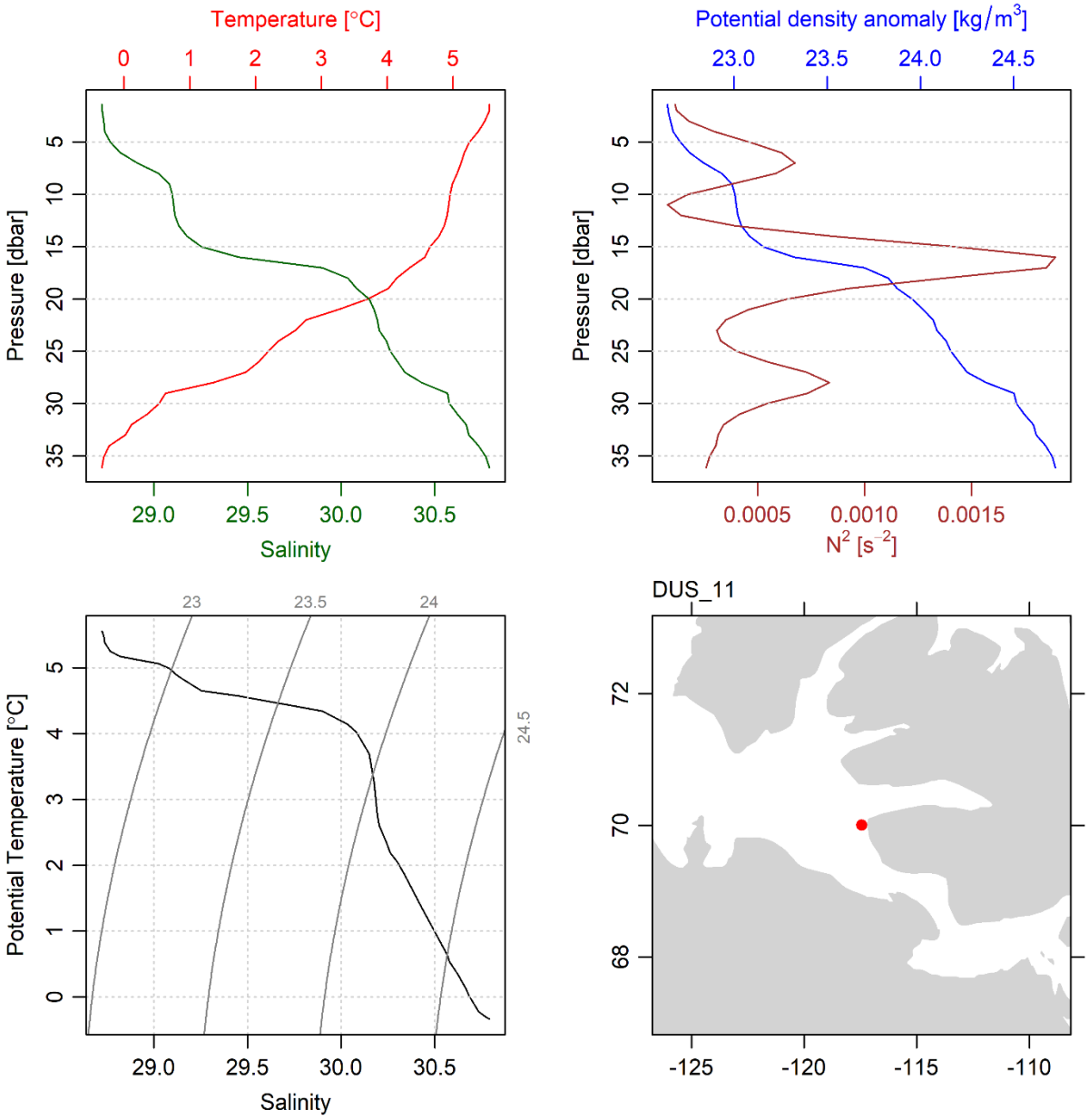

23
24
25
26
27
Potential Temperature [°C]
5
4
3
2
1
0
-1
28
29
30
31
32
33
34
Salinity

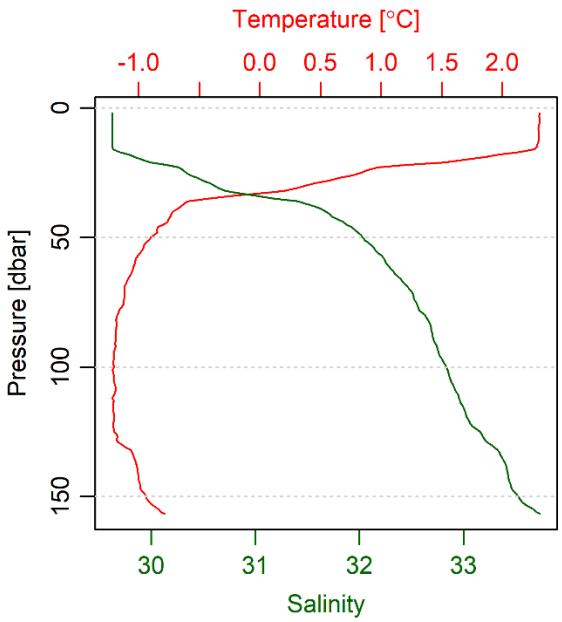

DUS_04
72
70
68
-125
-120
-115

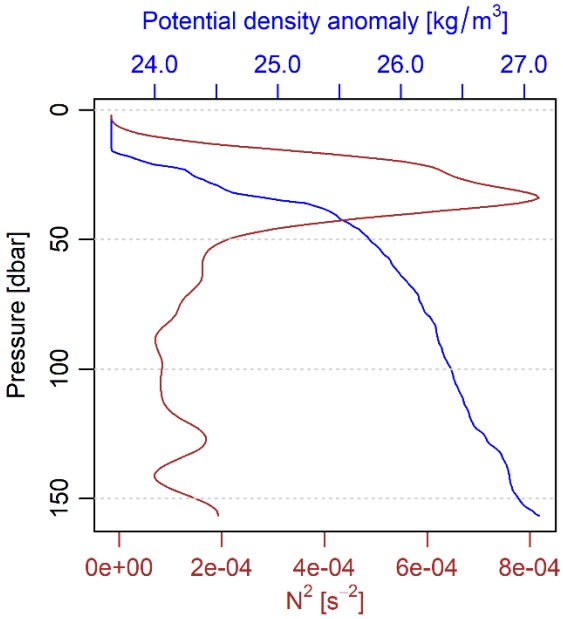

Temperature [°C]
-1 0 1 2 3 4 5
Pressure [dbar]
0 100 200 300 400 500
29 30 31 32 33 34
Salinity
Potential density anomaly [kg/m3]
23 24 25 26 27 28
Pressure [dbar]
0 100 200 300 400 500
0e+00 2e-04 4e-04 6e-04 8e-04 1e-03
N2 [s−2]
Potential Temperature [°C]
23 24 25 26 27
-1 0 1 2 3 4 5
28
29 30 31 32 33 34
Salinity
DUS_07
72 70 68
-125 -120 -115 -110

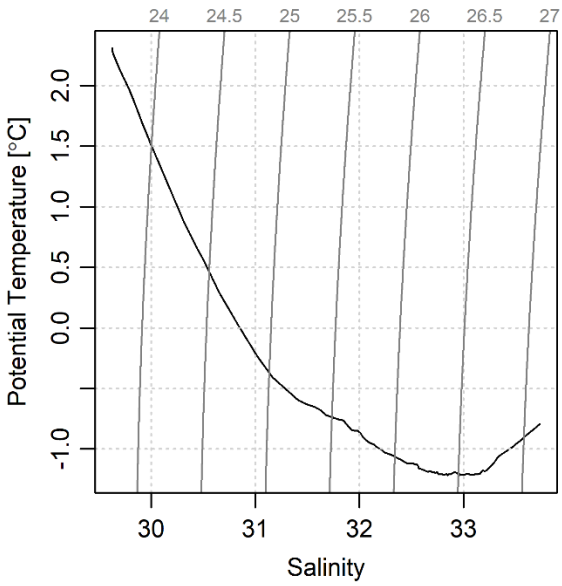

Temperature [°C]
-1
0
1
2
3
4
5
Pressure [dbar]
0
50
100
150
200
29
30
31
32
33
Salinity
Potential density anomaly [kg/m3]
23
24
25
26
27
0e+00
4e-04
6e-04
8e-04
1e-03
N2 [s−2]
Potential Temperature [°C]
23
24
25
26
27
DUS_09
72
70
68
-125
-120
-115
-110

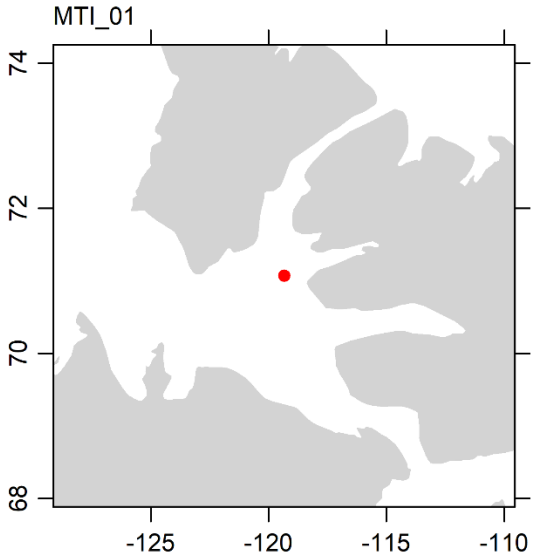

Temperature [°C]
-1
0
1
2
3
4
5
Pressure [dbar]
0
20
40
60
80
29
30
31
32
Salinity
Potential density anomaly [kg/m3]
22.5
23.5
24.5
25.5
0.0000
0.0005
0.0010
0.0015
N2 [s−2]
Potential Temperature [°C]
22.5
23
23.5
24
24.5
25
25.5
26
DUS_10
72
70
68
-125
-120
-115
-110

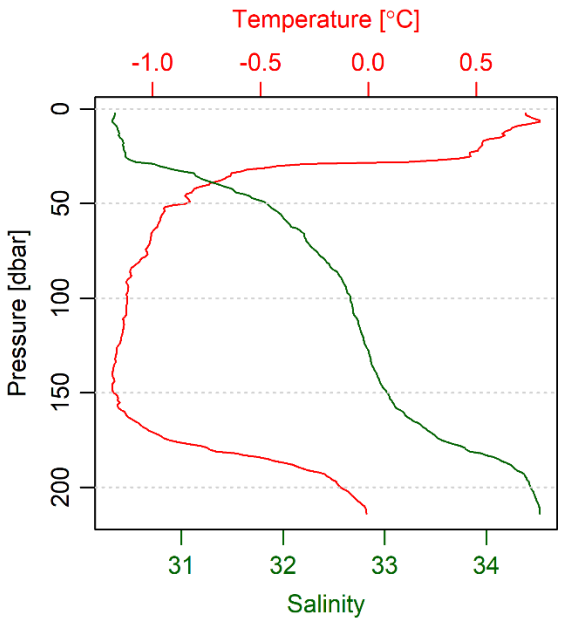

Temperature [°C]
0
1
2
3
4
5
Pressure [dbar]
5
10
15
20
25
30
35
29.0
29.5
30.0
30.5
Salinity
Potential density anomaly [kg/m3]
23.0
23.5
24.0
24.5
0.0005
0.0010
0.0015
N2 [s−2]
Potential Temperature [°C]
23
23.5
24
24.5
0
1
2
3
4
5
DUS_11
72
70
68
-125
-120
-115
-110

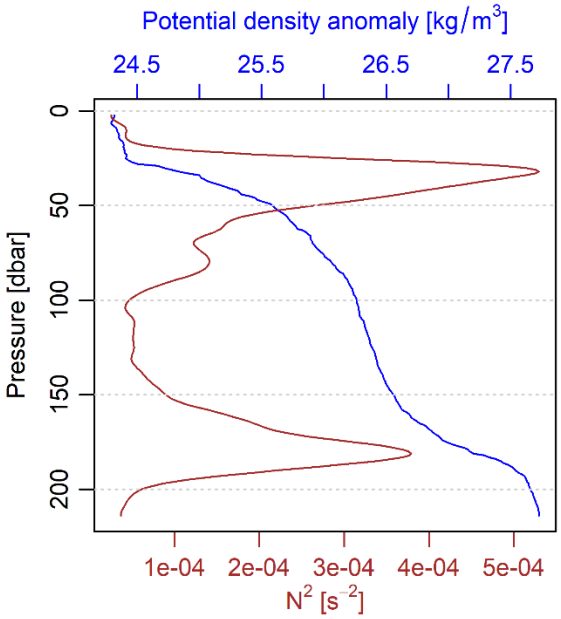

Temperature [°C]
-1.0
0.0
0.5
1.0
1.5
2.0
Pressure [dbar]
0
50
100
150
30
31
32
33
Salinity

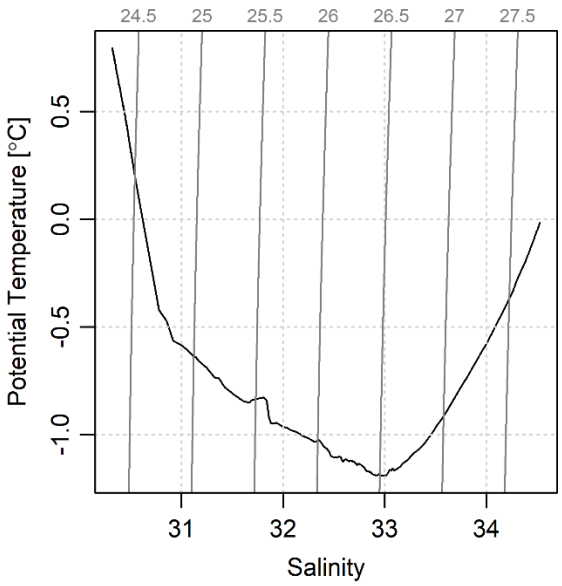

Potential density anomaly [kg/m3]
24.0
25.0
26.0
27.0
Pressure [dbar]
0
50
100
150
0e+00
2e-04
4e-04
6e-04
8e-04
N2 [s−2]

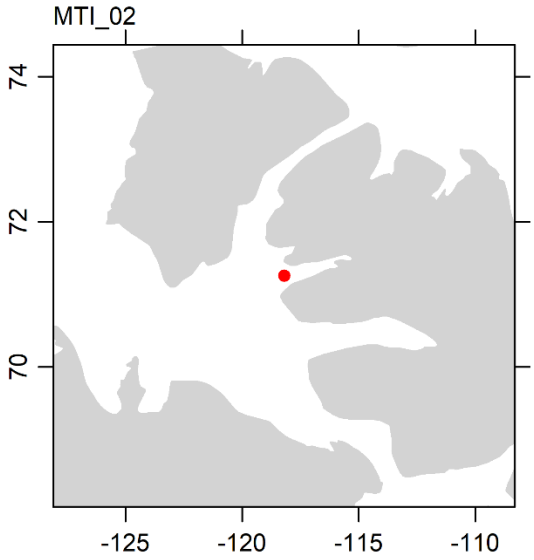

24
24.5
25
25.5
26
26.5
27
Potential Temperature [°C]
-1.0
0.0
0.5
1.0
1.5
2.0
30
31
32
33
Salinity

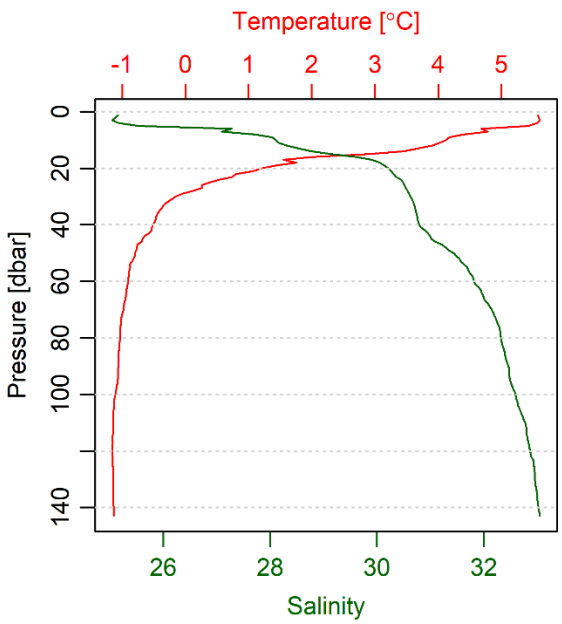

MTI_01
74
72
70
68
-125
-120
-115
-110

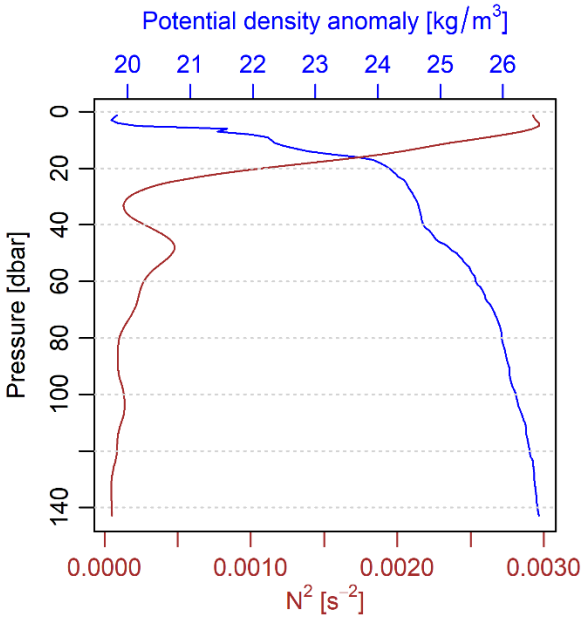

Temperature [°C]
-1.0
-0.5
0.0
0.5
Pressure [dbar]
0
50
100
150
200
31
32
33
34
Salinity

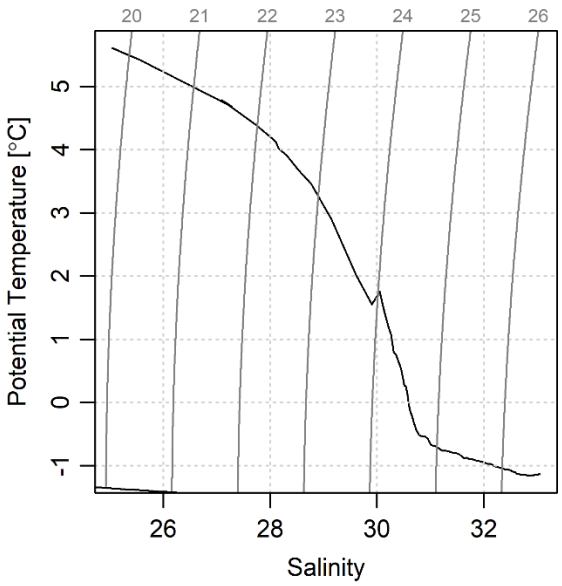

Potential density anomaly [kg/m3]
24.5
25.5
26.5
27.5
Pressure [dbar]
0
50
100
150
200
1e-04
2e-04
3e-04
4e-04
5e-04
N2 [s−2]

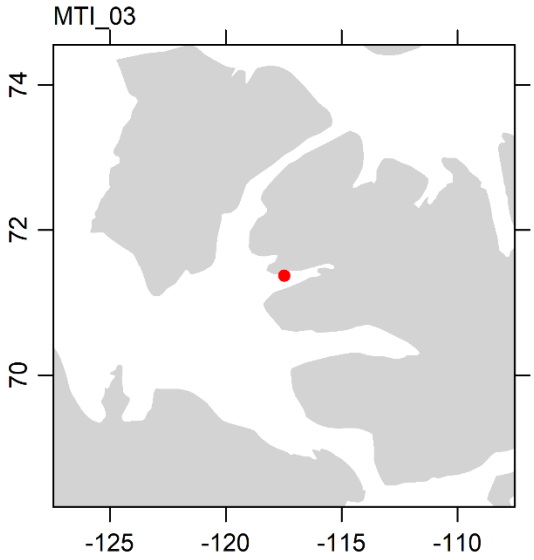

24.5
25
25.5
26
26.5
27
27.5
Potential Temperature [°C]
0.5
0.0
-0.5
-1.0
31
32
33
34
Salinity

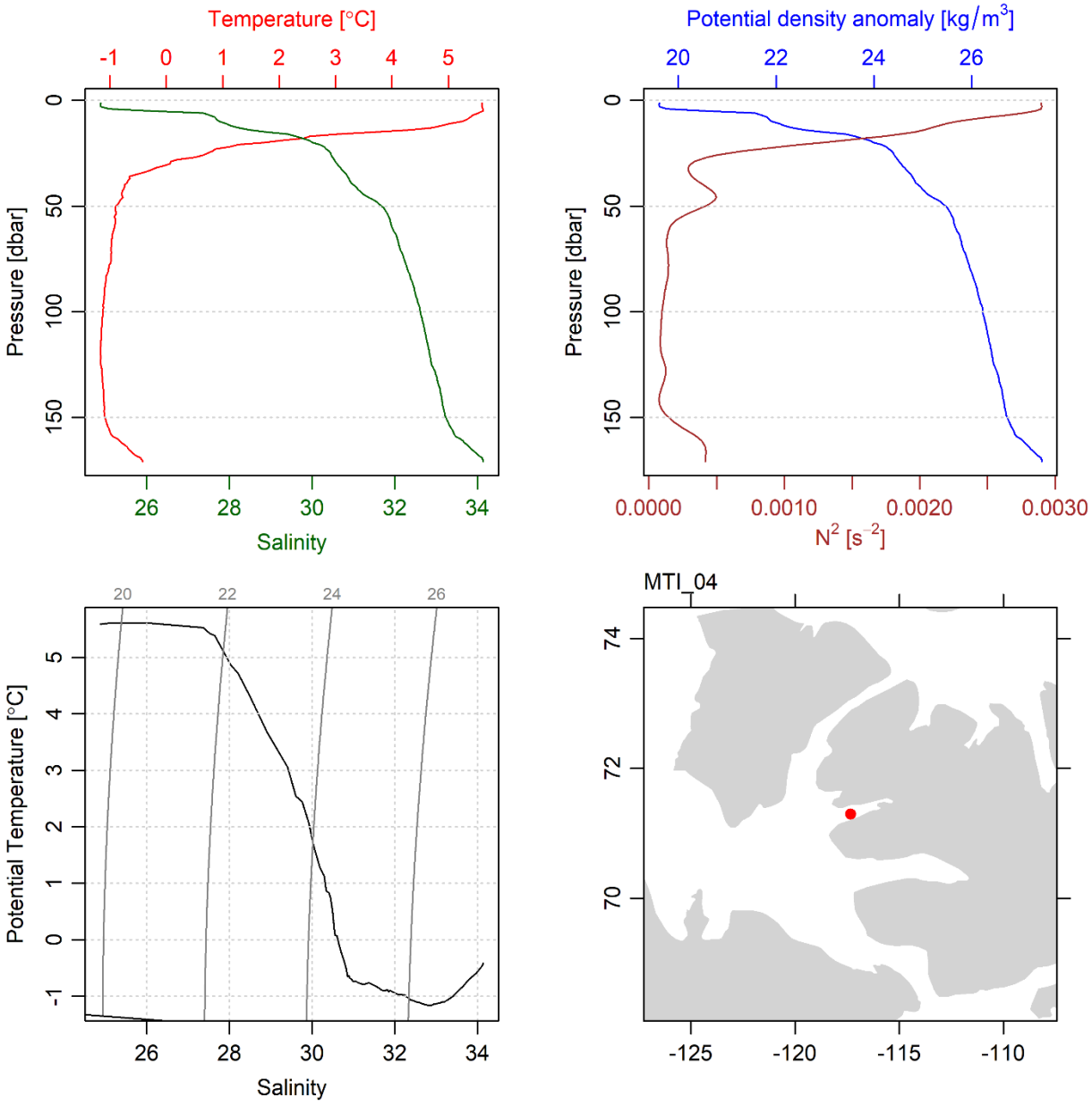

MTI_02
74
72
70
-125
-120
-115
-110

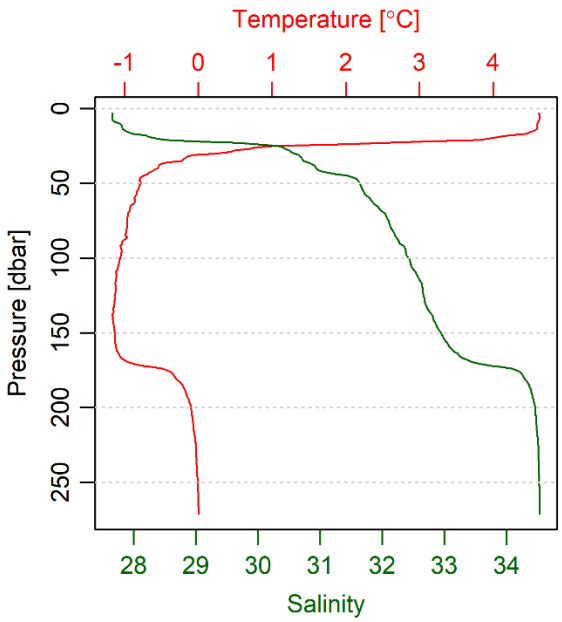

Temperature [°C]
-1
0
1
2
3
4
5
Pressure [dbar]
0
20
40
60
80
100
140
26
28
30
32
Salinity

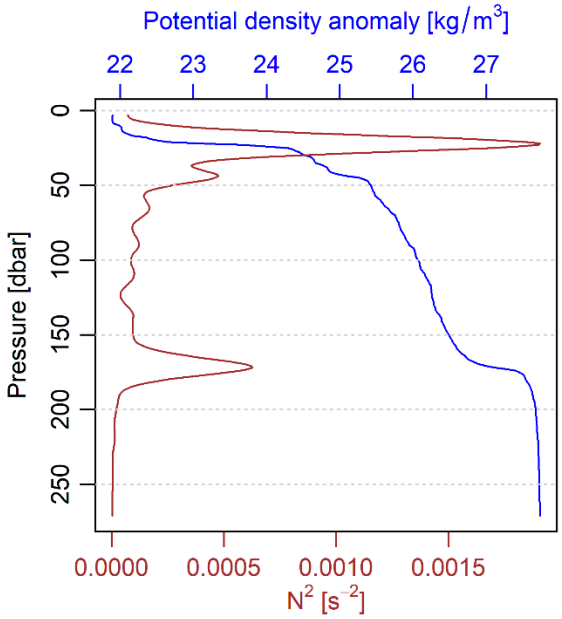

Potential density anomaly [kg/m3]
20
21
22
23
24
25
26
Pressure [dbar]
0
20
40
60
80
100
140
0.0000
0.0010
0.0020
0.0030
N2 [s−2]

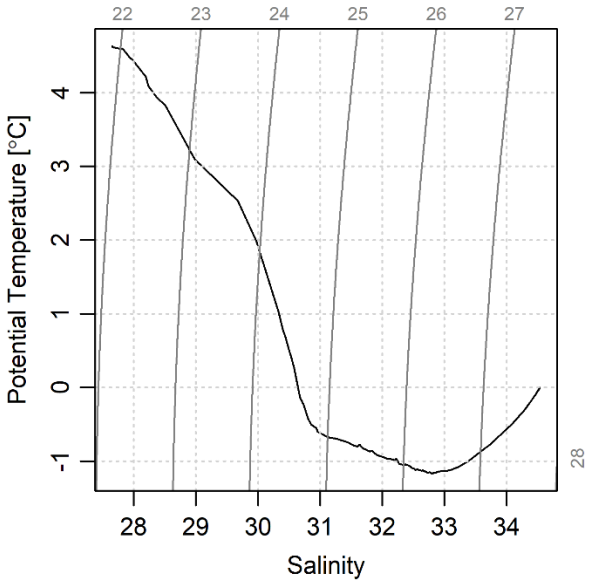

20
21
22
23
24
25
26
Potential Temperature [°C]
-1
0
1
2
3
4
5
26
28
30
32
Salinity

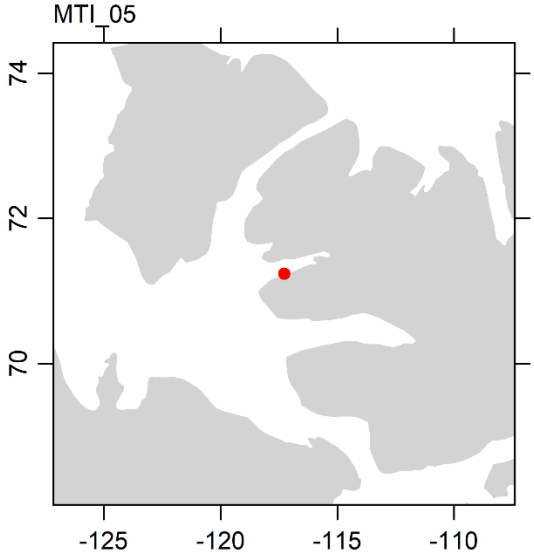

MTI_03
74
72
70
-125
-120
-115
-110

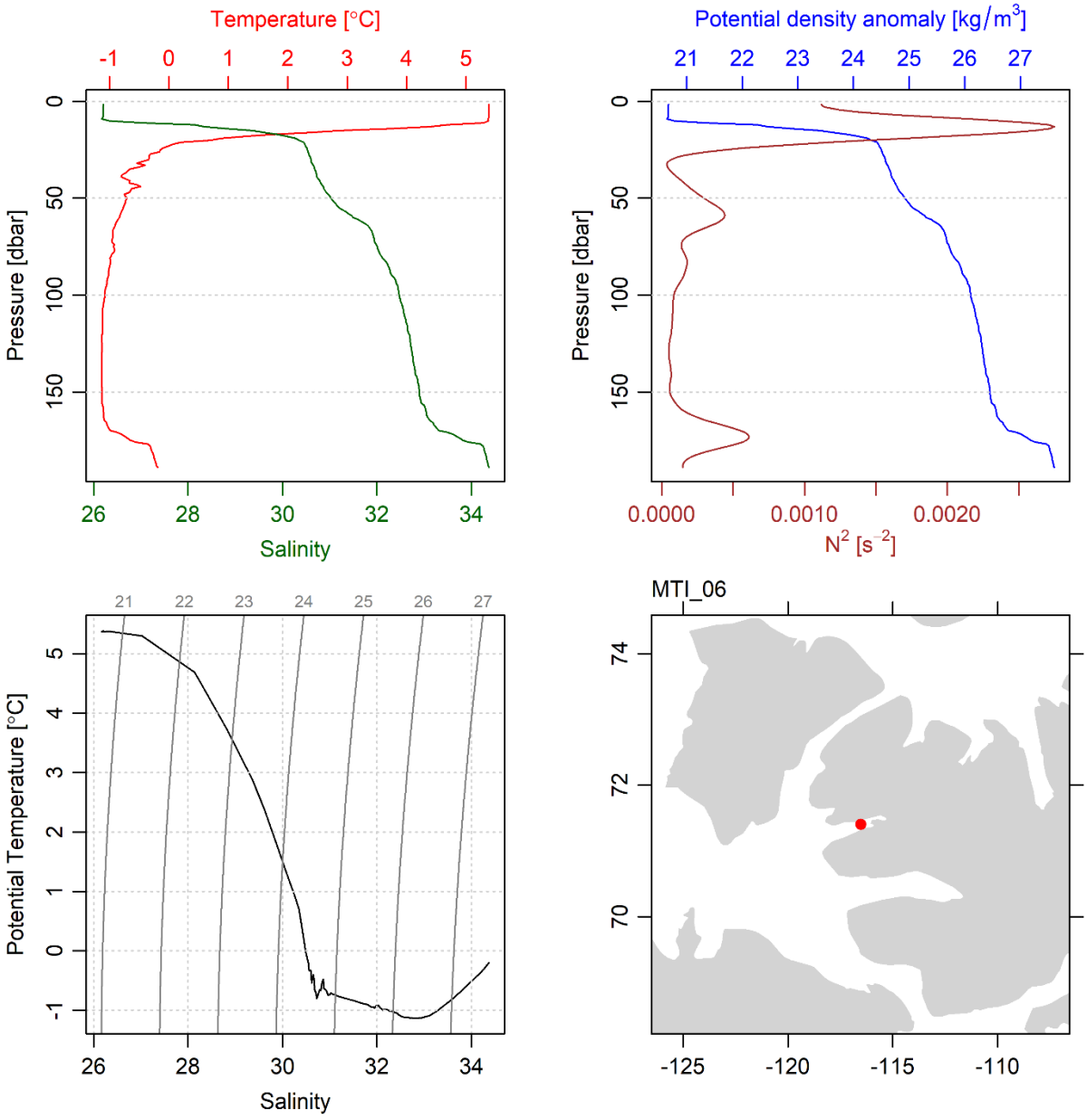

Temperature [°C]
-1
0
1
2
3
4
5
Pressure [dbar]
0
50
100
150
26
28
30
32
34
Salinity
Potential density anomaly [kg/m3]
20
22
24
26
0.0000
0.0010
0.0020
0.0030
N2 [s−2]
Potential Temperature [°C]
MTI_04
74
72
70
-125
-120
-115
-110

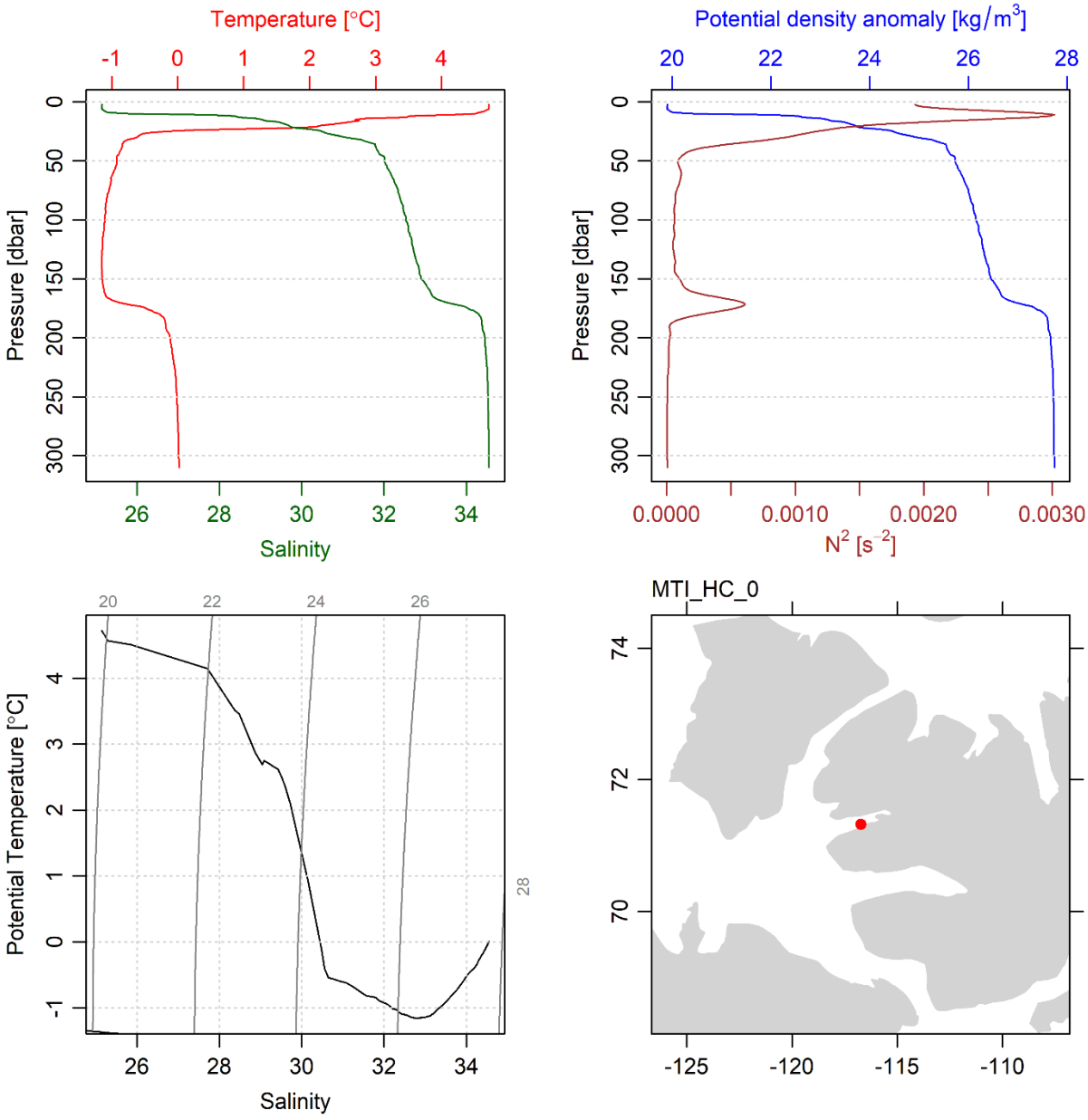

Temperature [°C]
-1
0
1
2
3
4
Pressure [dbar]
0
50
100
150
200
250
28
29
30
31
32
33
34
Salinity

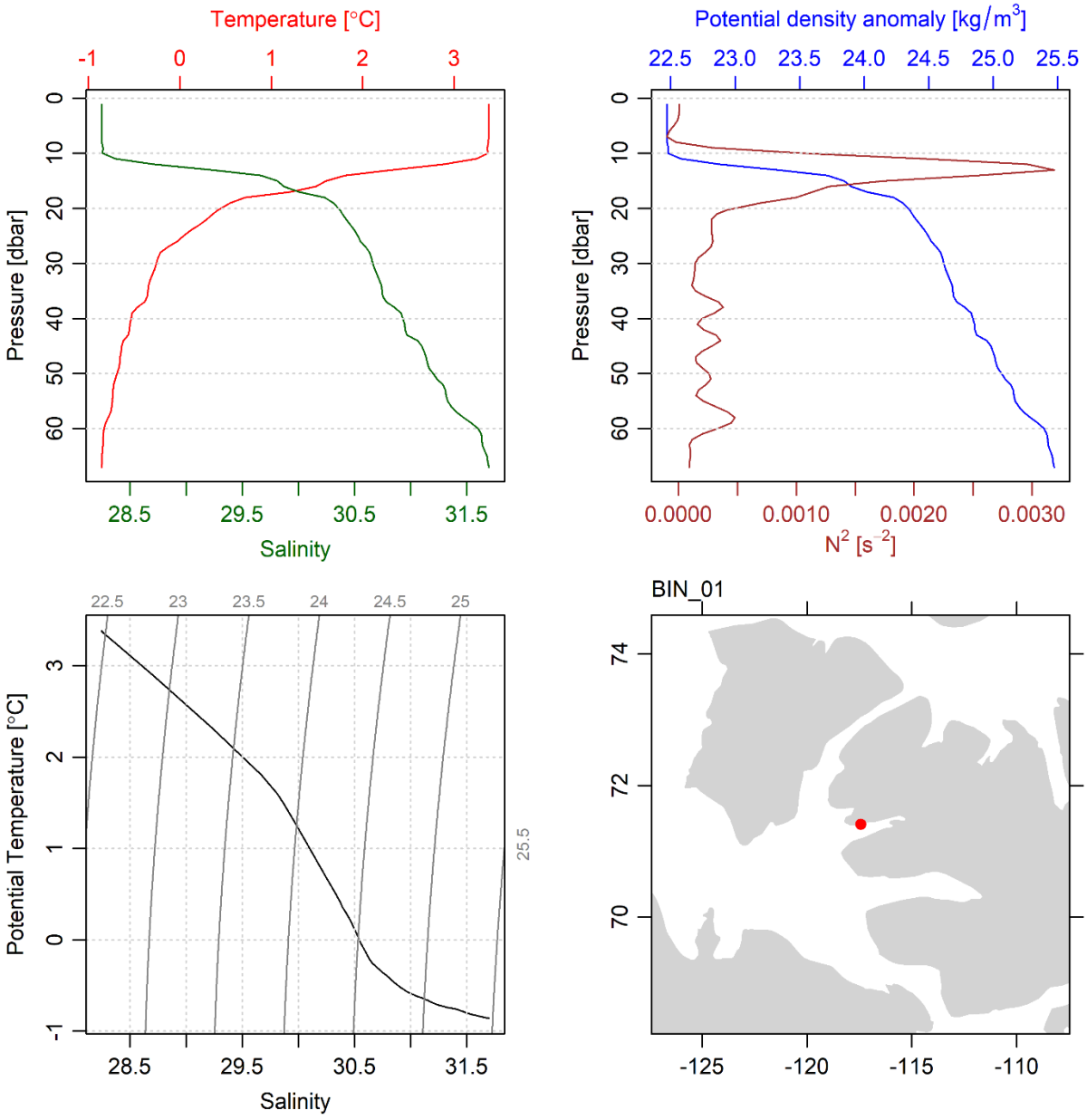

Potential density anomaly [kg/m3]
22
23
24
25
26
27
Pressure [dbar]
0
50
100
150
200
250
0.0000
0.0005
0.0010
0.0015
N2 [s−2]

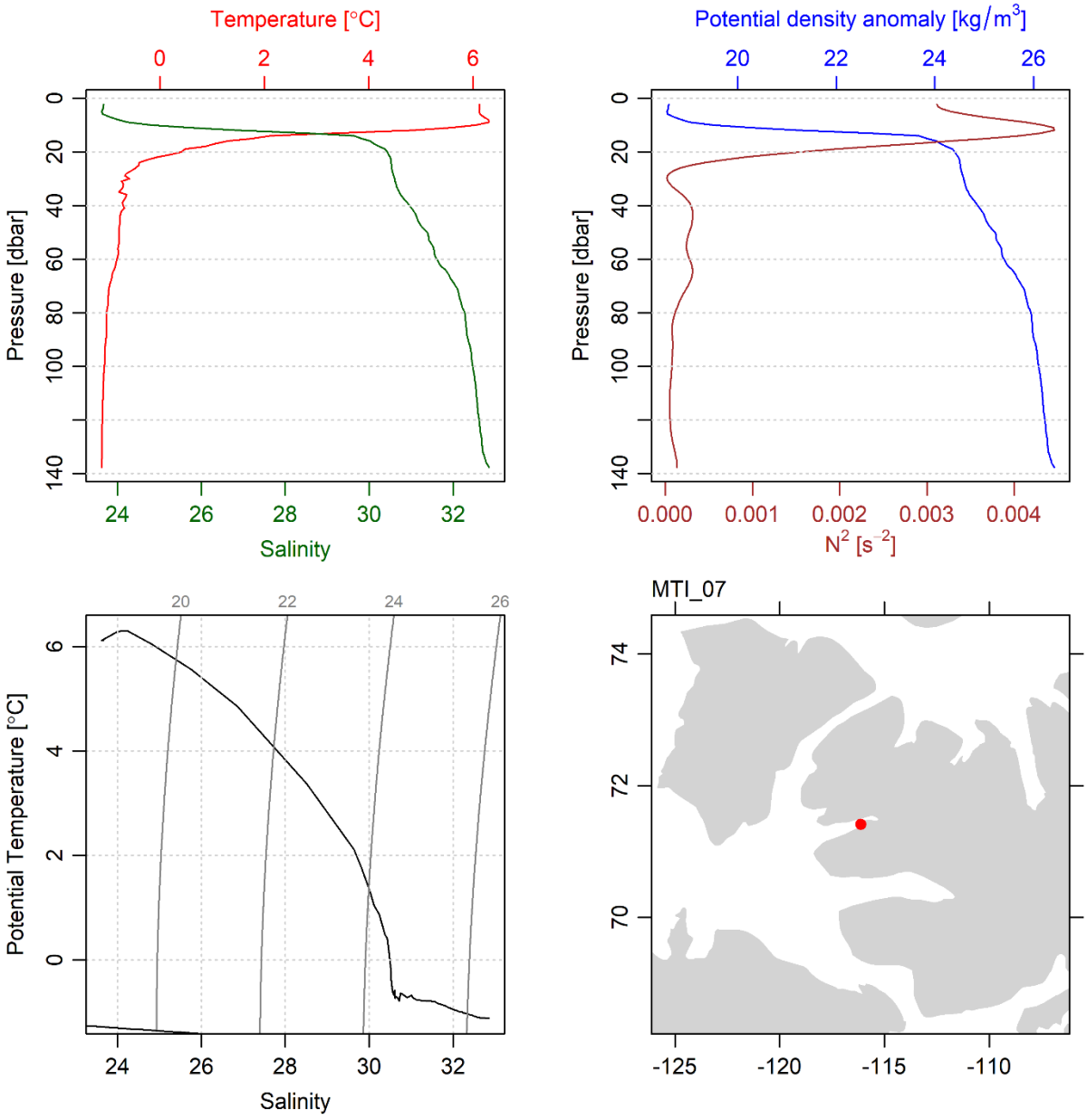

22
23
24
25
26
27
Potential Temperature [°C]
-1
0
1
2
3
4
28
29
30
31
32
33
34
Salinity
28

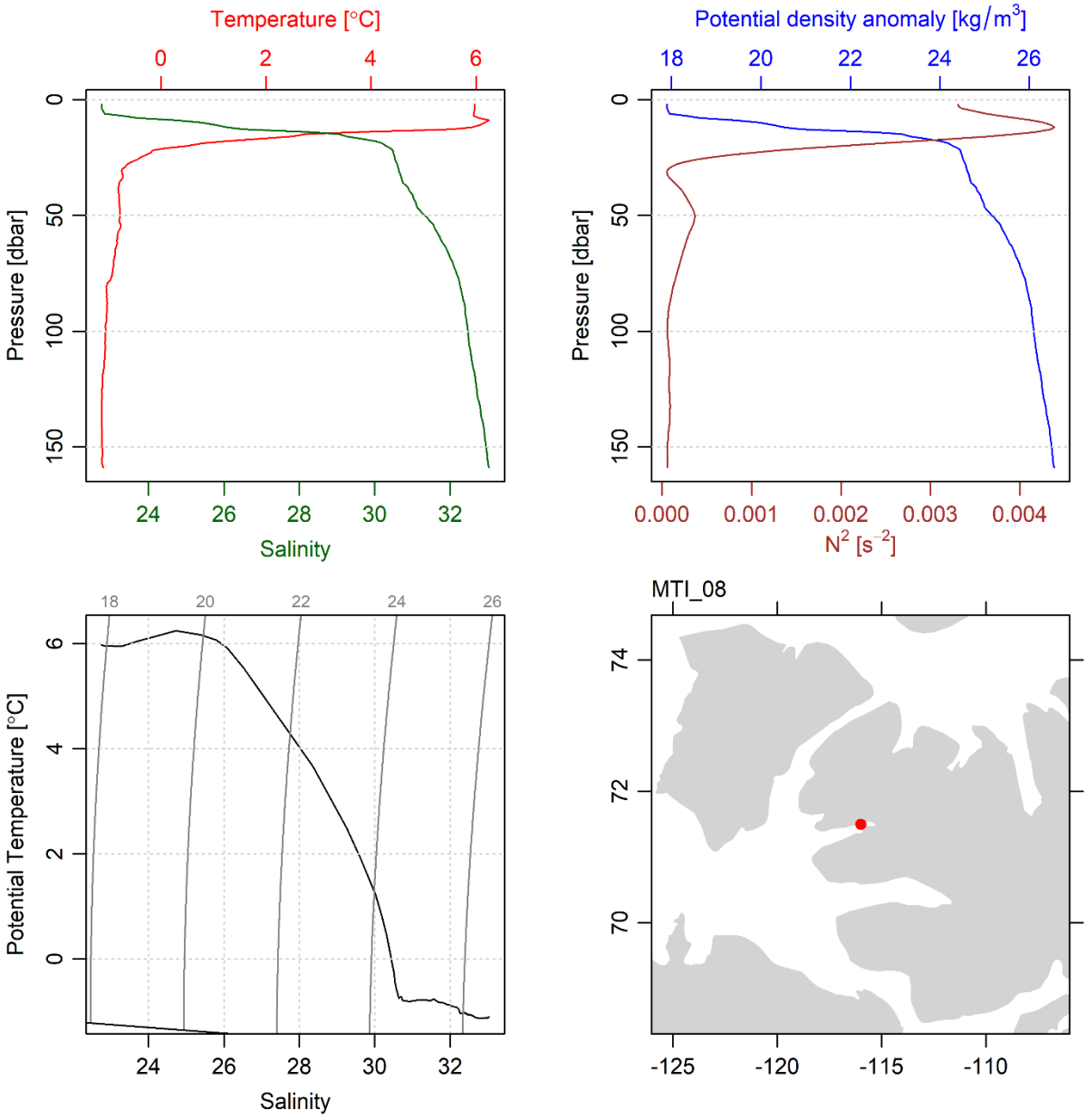

MTI_05
74
72
70
-125
-120
-115
-110

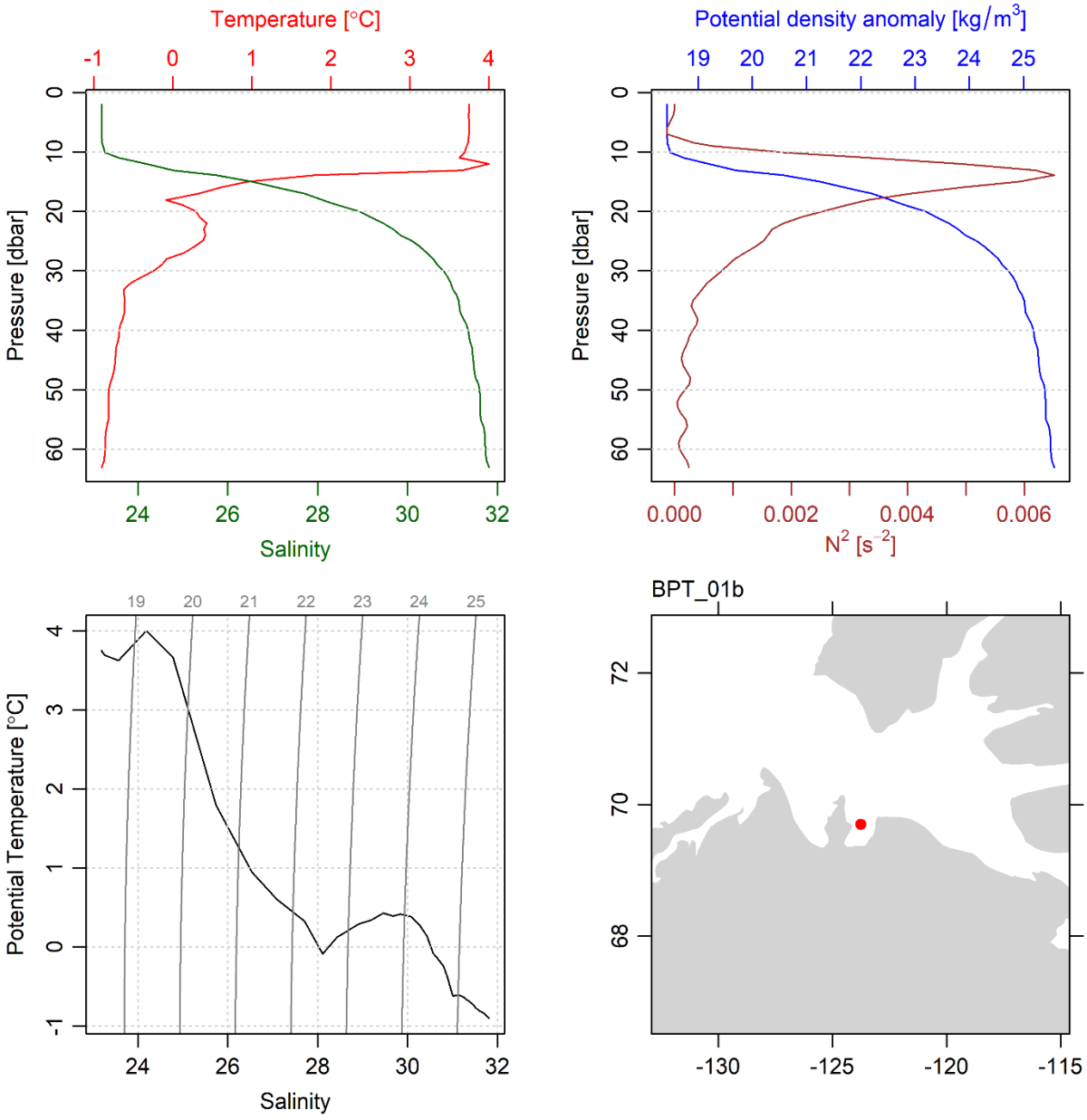

Temperature [°C]
-1 0 1 2 3 4 5
Pressure [dbar]
0 50 100 150
26 28 30 32 34
Salinity
Potential density anomaly [kg/m$^3$]
21 22 23 24 25 26 27
Pressure [dbar]
0 50 100 150
0.0000 0.0010 0.0020
N$^2$ [s$^{-2}$]
21 22 23 24 25 26 27
Potential Temperature [°C]
-1 0 1 2 3 4 5
26 28 30 32 34
Salinity
MTI_06
74 72 70
-125 -120 -115 -110

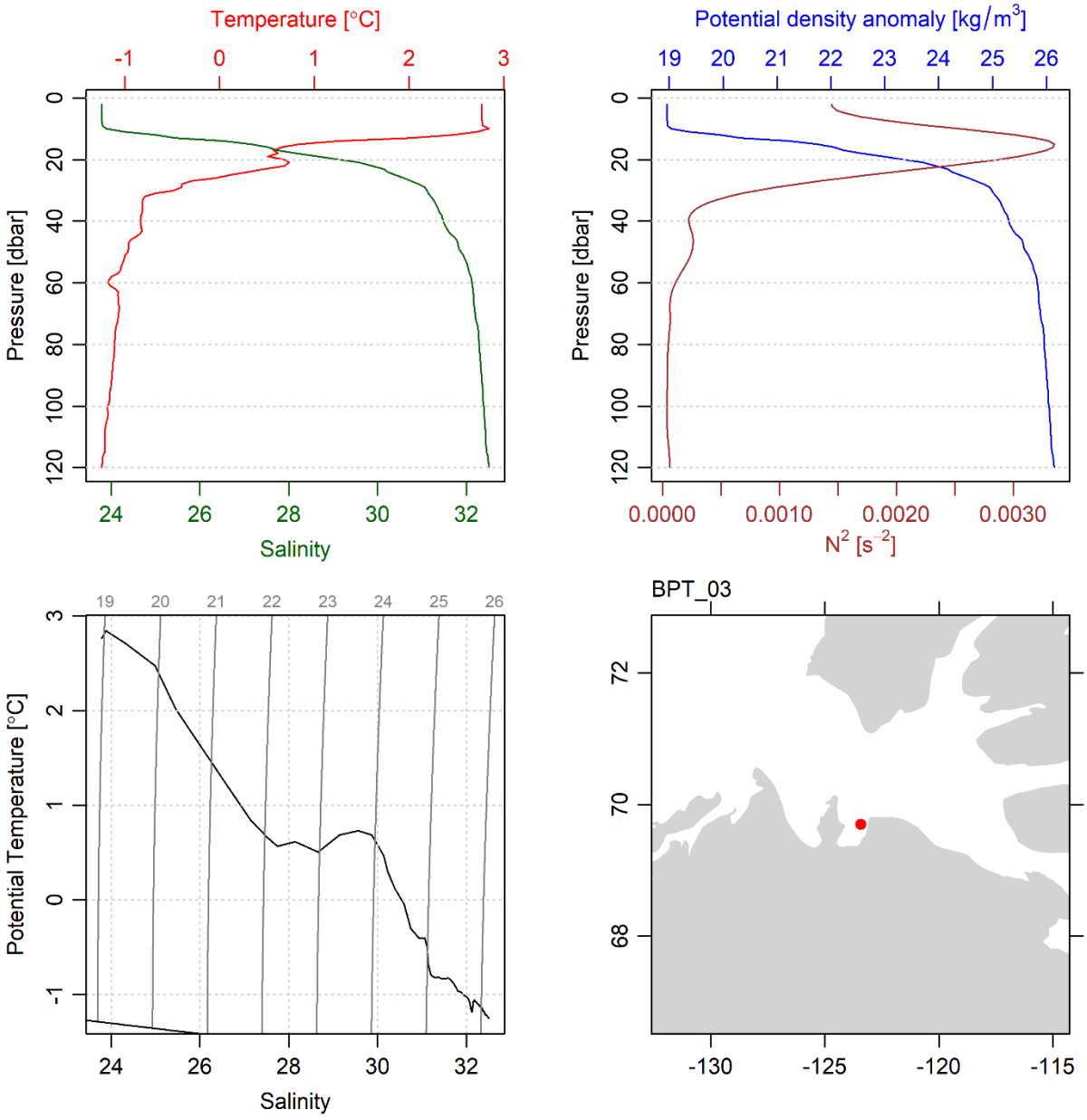

Temperature [°C]
-1
0
1
2
3
4
Pressure [dbar]
0
50
100
150
200
250
300
26
28
30
32
34
Salinity
Potential density anomaly [kg/m3]
20
22
24
26
28
0.0000
0.0010
0.0020
0.0030
N2 [s−2]
Potential Temperature [°C]
MTI_HC_0
74
72
70
-125
-120
-115
-110

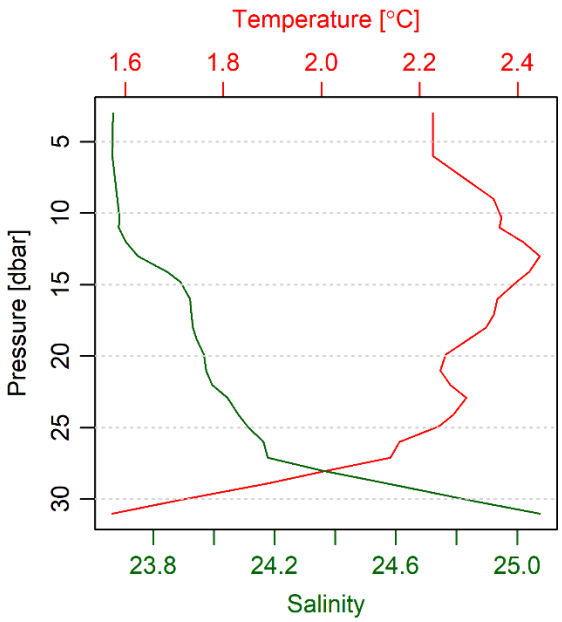

Temperature [°C]
-1
0
1
2
3
Pressure [dbar]
0
10
20
30
40
50
60
28.5
29.5
30.5
31.5
Salinity
Potential density anomaly [kg/m3]
22.5
23.0
23.5
24.0
24.5
25.0
25.5
0.0000
0.0010
0.0020
0.0030
N2 [s−2]
Potential Temperature [°C]
22.5
23
23.5
24
24.5
25
25.5
BIN_01
74
72
70
-125
-120
-115
-110

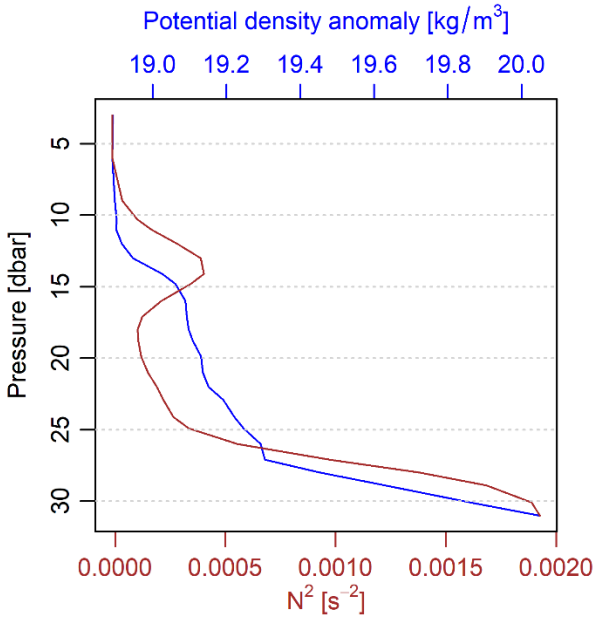

Temperature [°C]
0
2
4
6
Pressure [dbar]
0
20
40
60
80
100
140
24
26
28
30
32
Salinity
Potential density anomaly [kg/m3]
20
22
24
26
0.000
0.001
0.002
0.003
0.004
N2 [s−2]
Potential Temperature [°C]
MTI_07
74
72
70
-125
-120
-115
-110

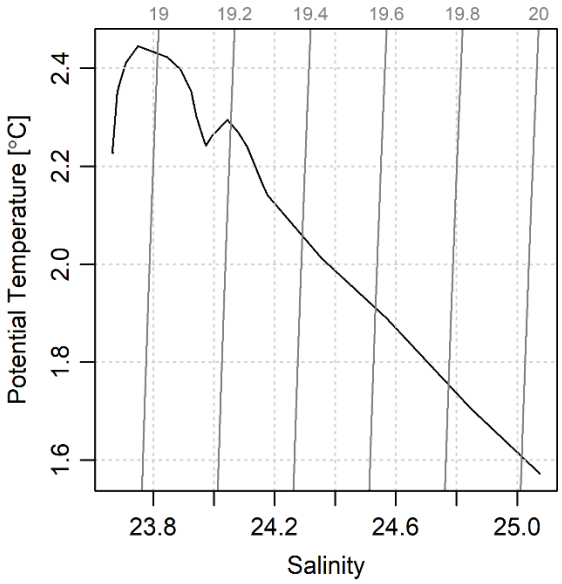

Temperature [°C]
0
2
4
6
Pressure [dbar]
0
50
100
150
24
26
28
30
32
Salinity
Potential density anomaly [kg/m3]
18
20
22
24
26
0.000
0.001
0.002
0.003
0.004
N2 [s−2]
18
20
22
24
26
Potential Temperature [°C]
0
2
4
6
24
26
28
30
32
Salinity
MTI_08
74
72
70
-125
-120
-115
-110

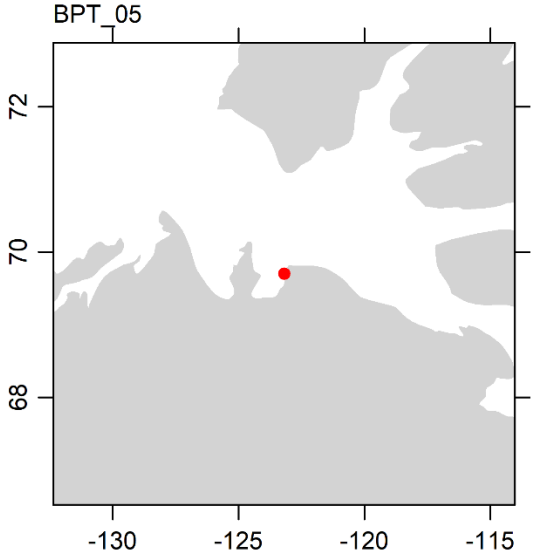

Temperature [°C]
-1
0
1
2
3
4
Pressure [dbar]
0
10
20
30
40
50
60
24
26
28
30
32
Salinity
Potential density anomaly [kg/m3]
19
20
21
22
23
24
25
0.000
0.002
0.004
0.006
N2 [s−2]
Potential Temperature [°C]
-1
0
1
2
3
4
BPT_01b
72
70
68
-130
-125
-120
-115

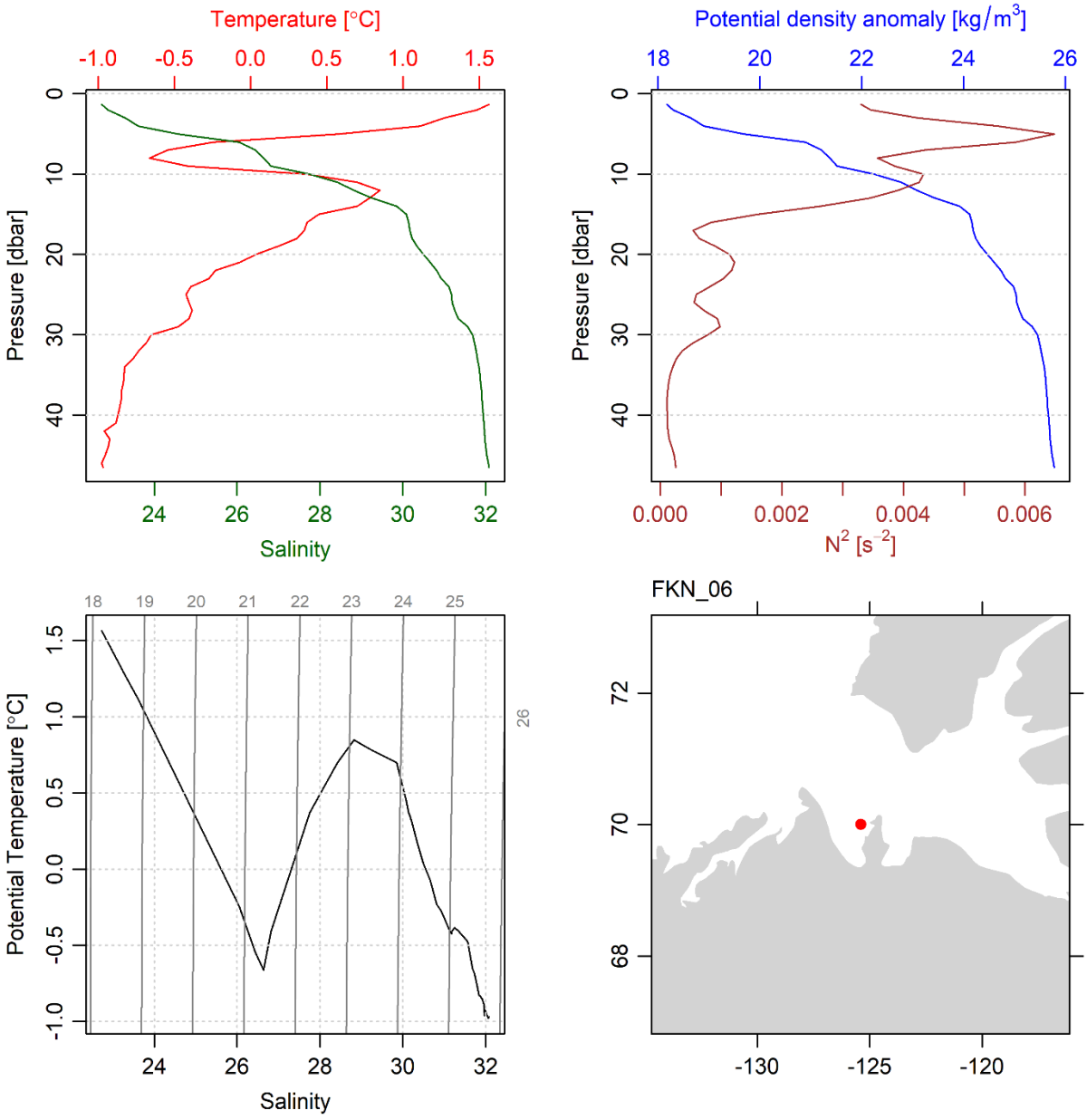

Temperature [°C]
-1
0
1
2
3
Pressure [dbar]
0
20
40
60
80
100
120
24
26
28
30
32
Salinity
Potential density anomaly [kg/m3]
19
20
21
22
23
24
25
26
0.0000
0.0010
0.0020
0.0030
N2 [s−2]
Potential Temperature [°C]
BPT_03
72
70
68
-130
-125
-120
-115

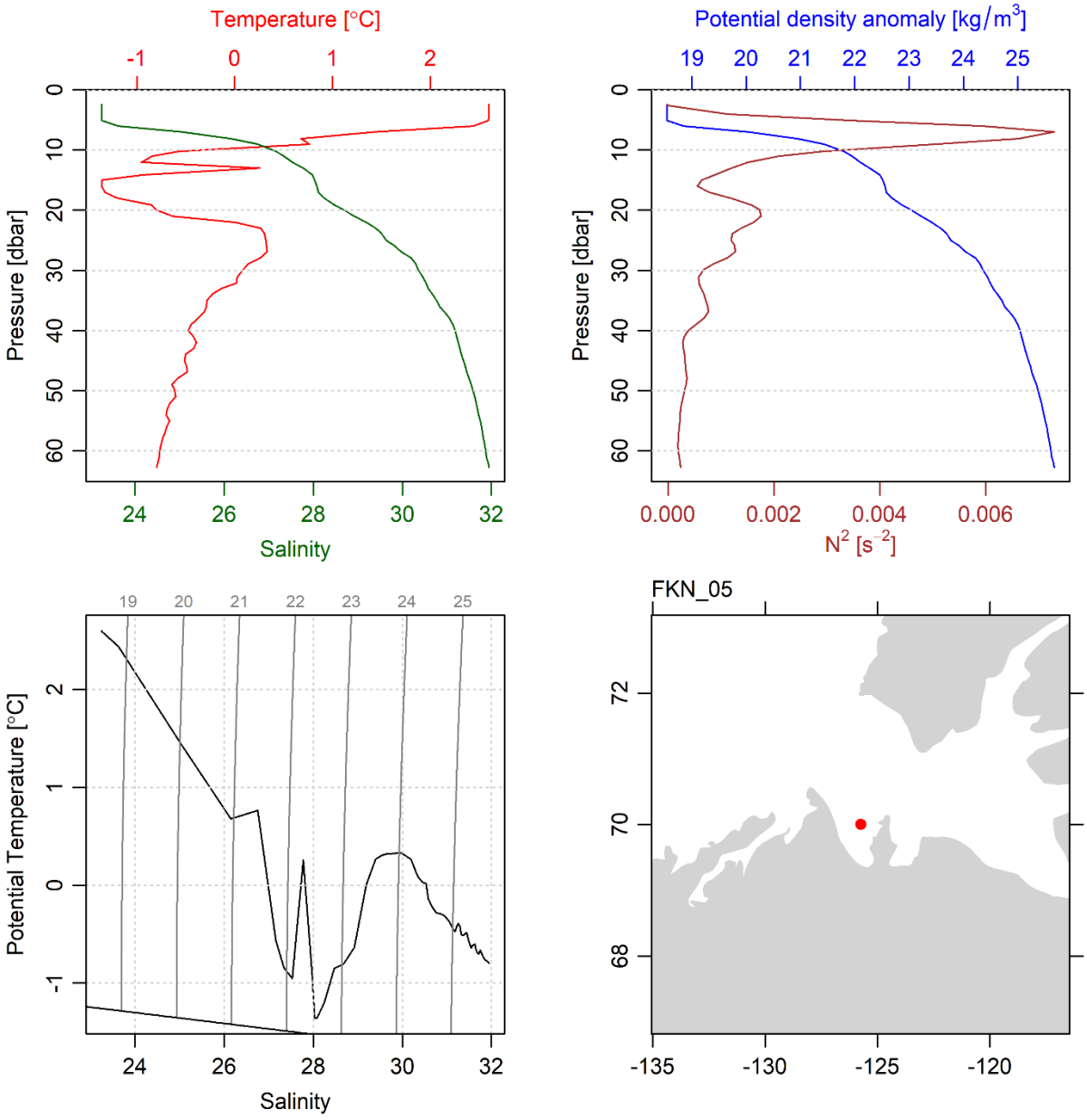

Temperature [°C]
1.6
1.8
2.0
2.2
2.4
Pressure [dbar]
5
10
15
20
25
30
23.8
24.2
24.6
25.0
Salinity

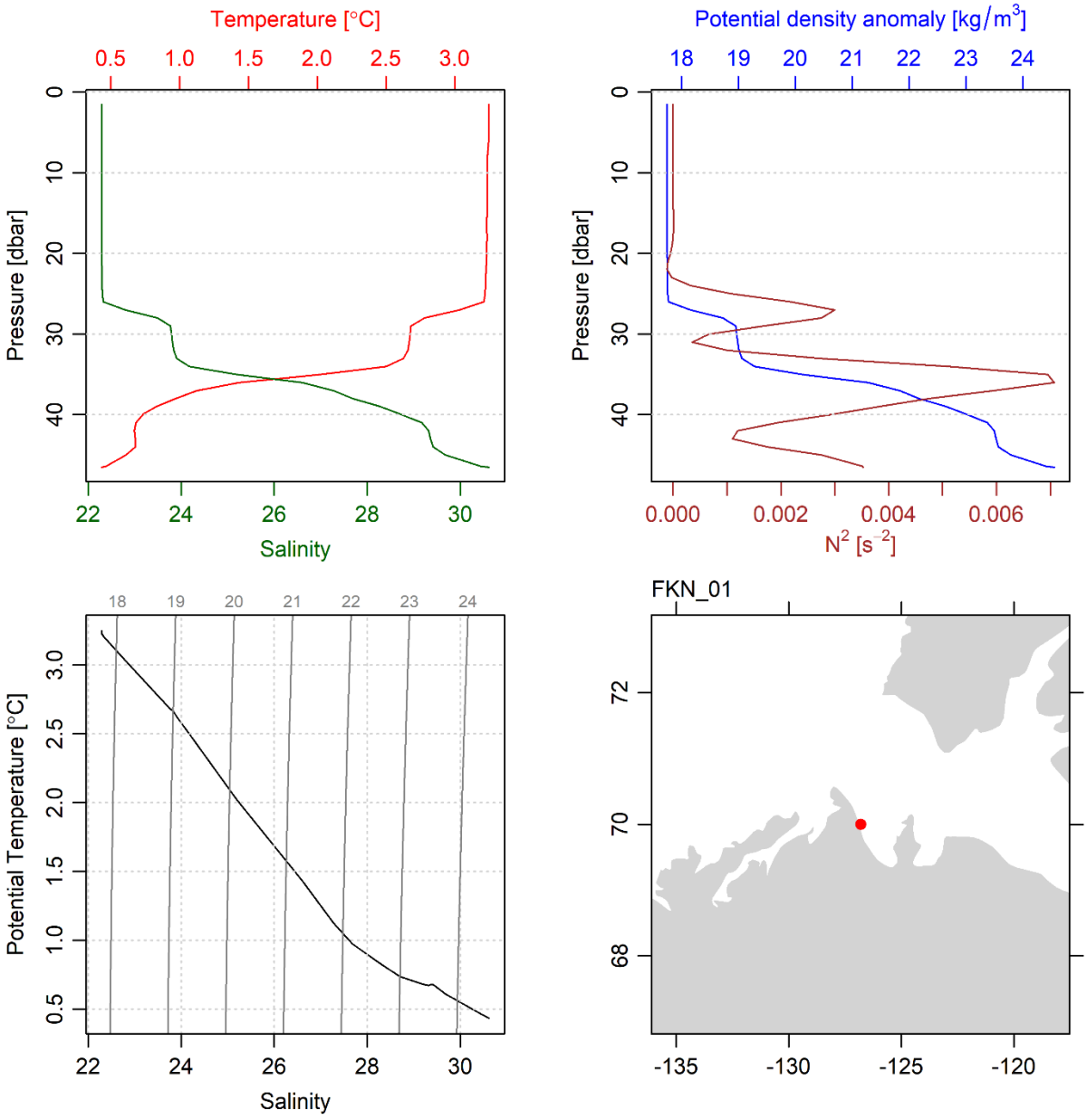

Potential density anomaly [kg/m3]
19.0
19.2
19.4
19.6
19.8
20.0
Pressure [dbar]
5
10
15
20
25
30
0.0000
0.0005
0.0010
0.0015
0.0020
N2 [s−2]

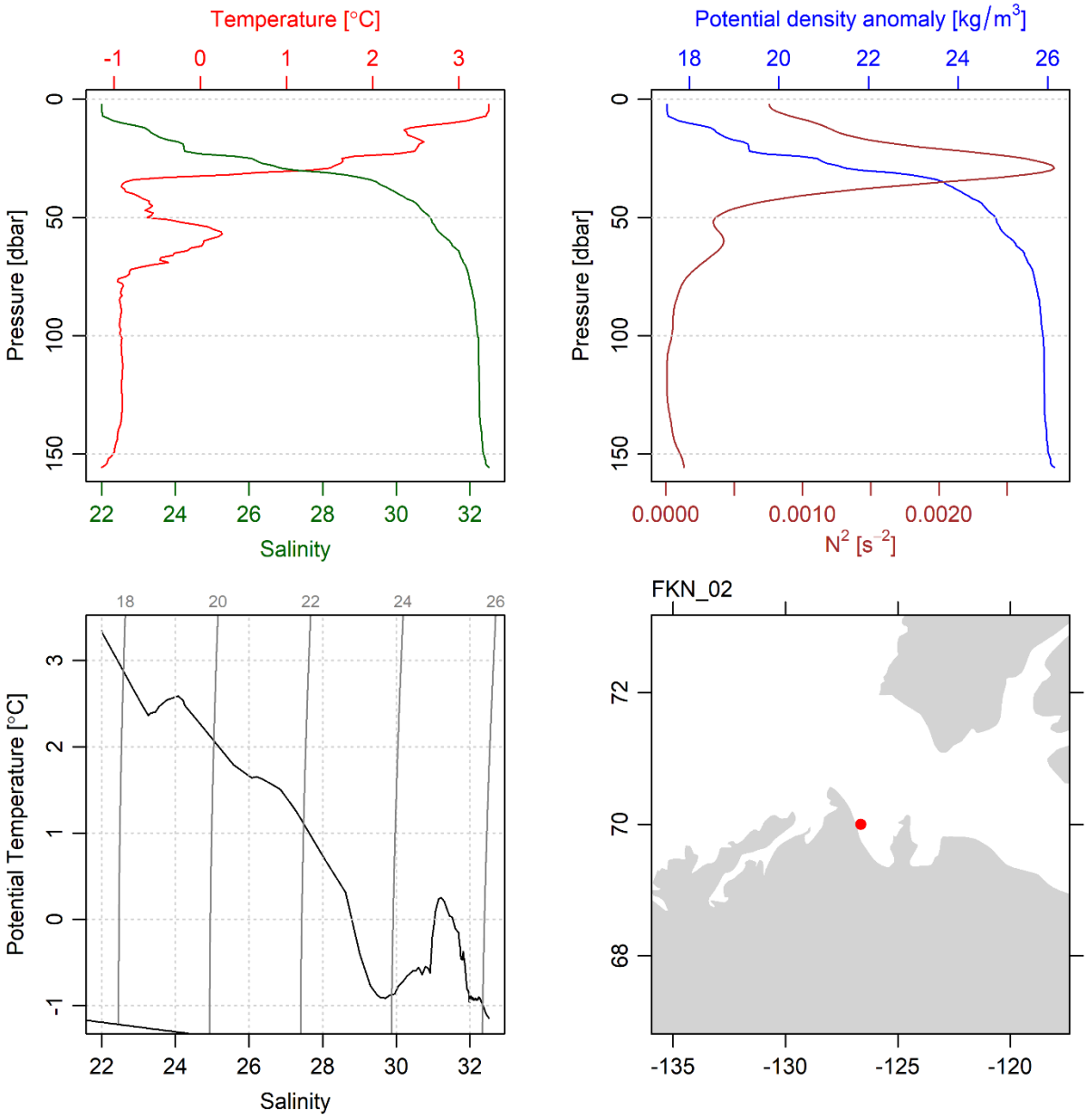

19
19.2
19.4
19.6
19.8
20
Potential Temperature [°C]
1.6
1.8
2.0
2.2
2.4
23.8
24.2
24.6
25.0
Salinity

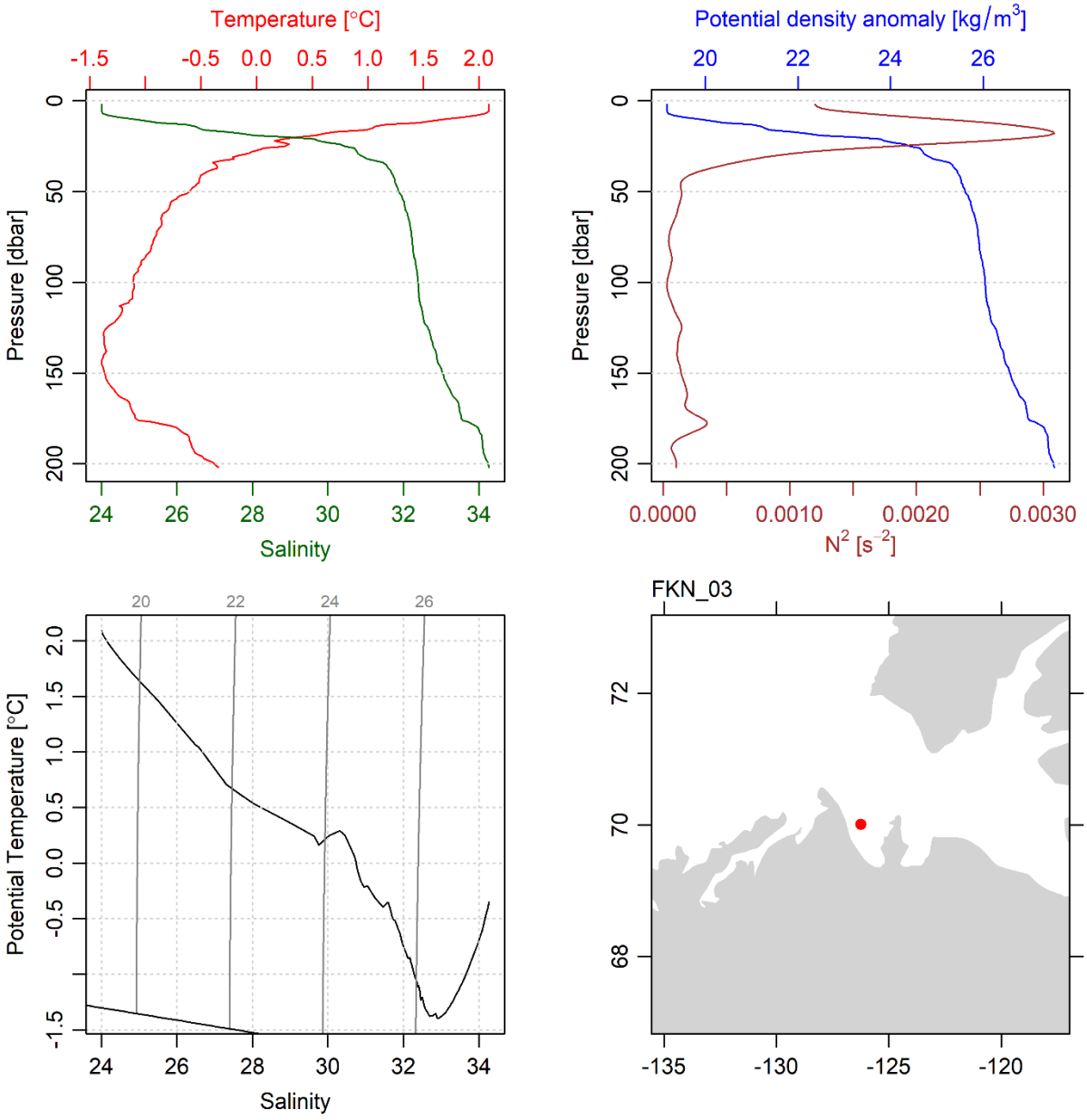

BPT_05
72
70
68
-130
-125
-120
-115

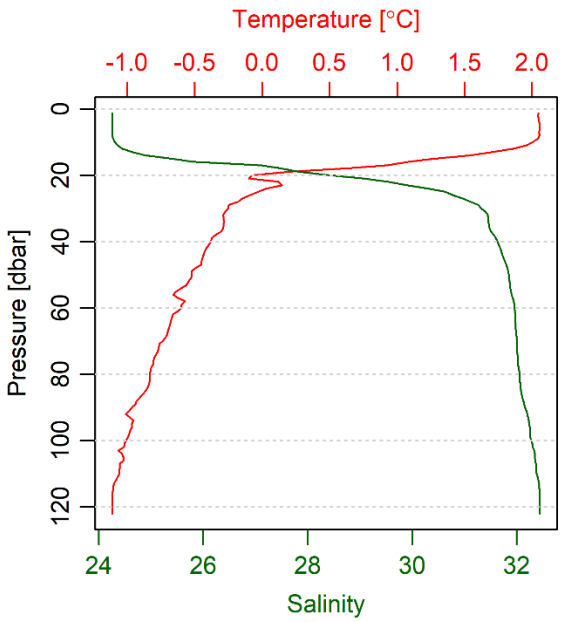

Temperature [°C]
-1.0
-0.5
0.0
0.5
1.0
1.5
Pressure [dbar]
0
10
20
30
40
24
26
28
30
32
Salinity
Potential density anomaly [kg/m3]
18
20
22
24
26
0.000
0.002
0.004
0.006
N2 [s−2]
Potential Temperature [°C]
18
19
20
21
22
23
24
25
26
FKN_06
72
70
68
-130
-125
-120

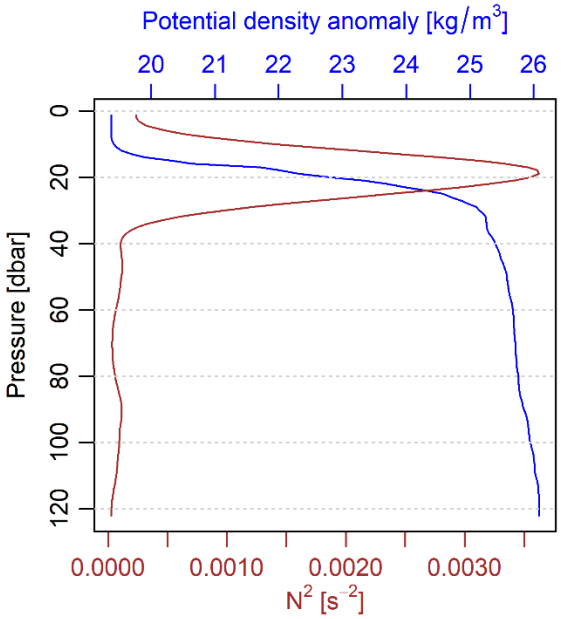

Temperature [°C]
-1
0
1
2
Pressure [dbar]
0
10
20
30
40
50
60
24
26
28
30
32
Salinity
Potential density anomaly [kg/m3]
19
20
21
22
23
24
25
0.000
0.002
0.004
0.006
N2 [s−2]
Potential Temperature [°C]
FKN_05
72
70
68
-135
-130
-125
-120

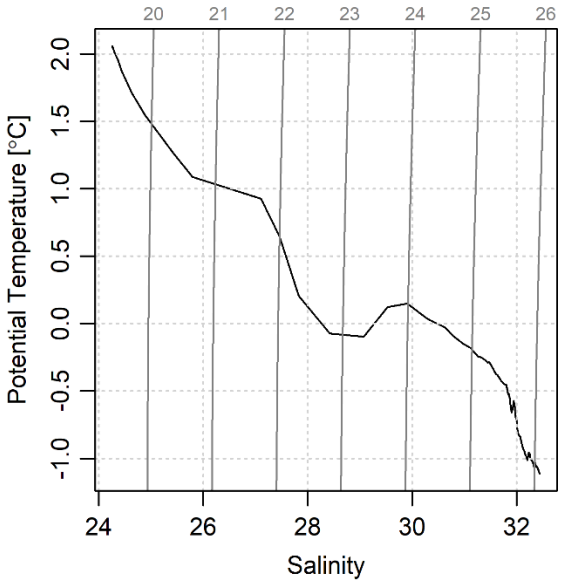

Temperature [°C]
0.5
1.0
1.5
2.0
2.5
3.0
Pressure [dbar]
0
10
20
30
40
22
24
26
28
30
Salinity
Potential density anomaly [kg/m3]
18
19
20
21
22
23
24
0.000
0.002
0.004
0.006
N2 [s−2]
Potential Temperature [°C]
FKN_01
72
70
68
-135
-130
-125
-120

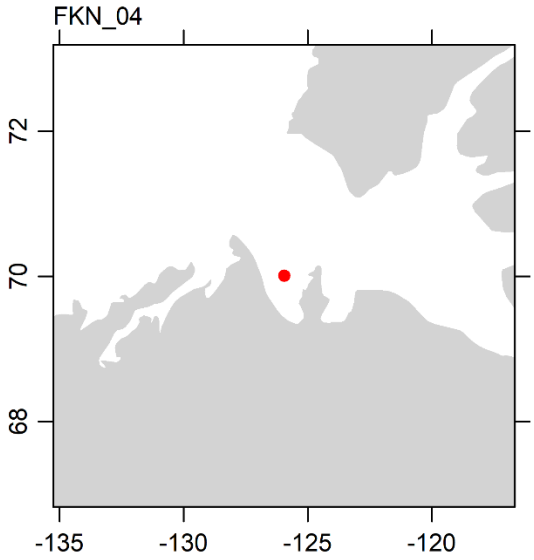

Temperature [°C]
-1
0
1
2
3
Pressure [dbar]
0
50
100
150
22
24
26
28
30
32
Salinity
Potential density anomaly [kg/m3]
18
20
22
24
26
0.0000
0.0010
0.0020
N2 [s−2]
Potential Temperature [°C]
FKN_02
72
70
68
-135
-130
-125
-120

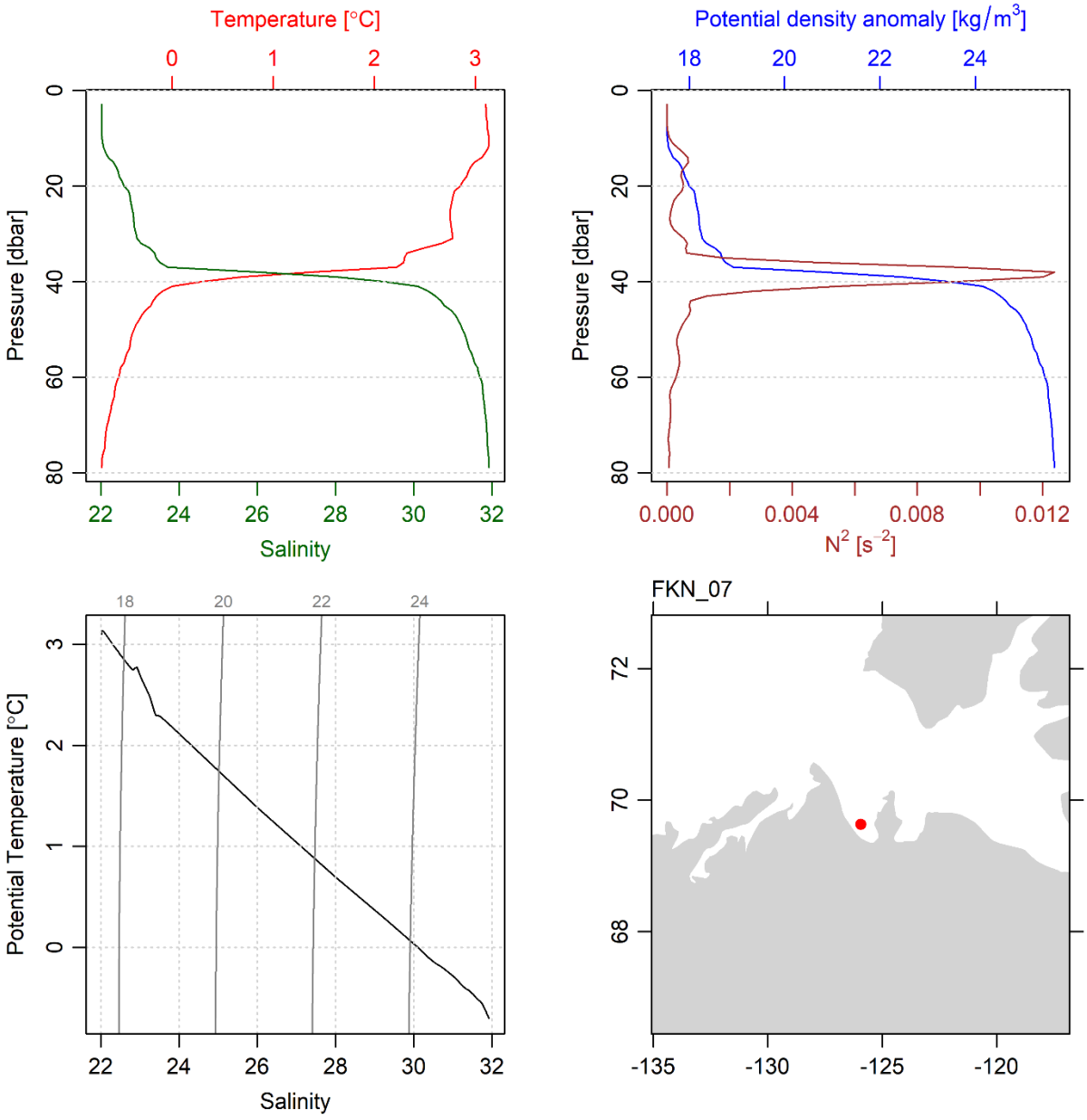

Temperature [°C]
-1.5
-0.5
0.0
0.5
1.0
1.5
2.0
Pressure [dbar]
0
50
100
150
200
24
26
28
30
32
34
Salinity
Potential density anomaly [kg/m3]
20
22
24
26
0.0000
0.0010
0.0020
0.0030
N2 [s−2]
Potential Temperature [°C]
FKN_03
72
70
68
-135
-130
-125
-120

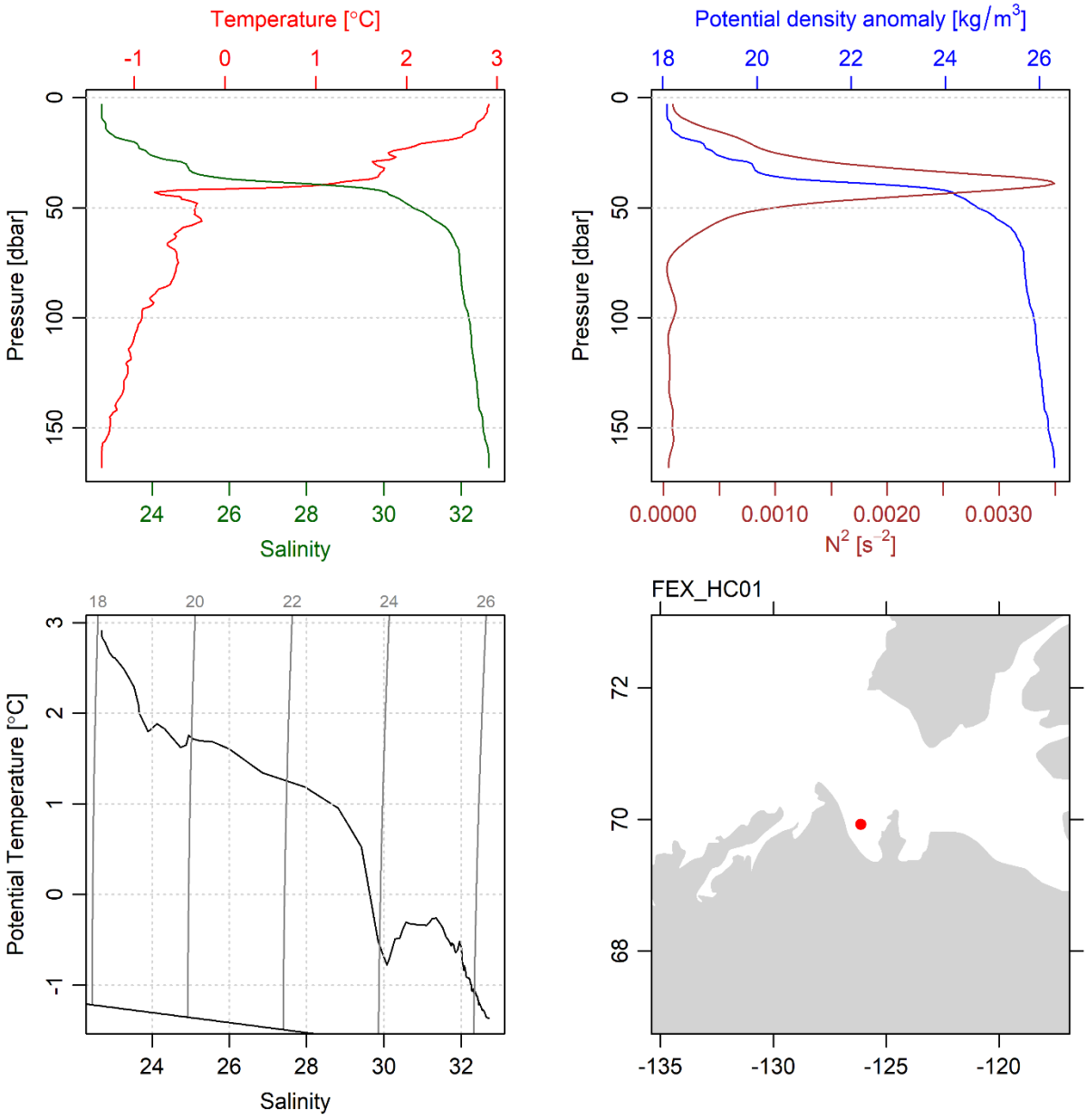

Temperature [°C]
-1.0 -0.5 0.0 0.5 1.0 1.5 2.0
Pressure [dbar]
0 20 40 60 80 100 120
24 26 28 30 32
Salinity

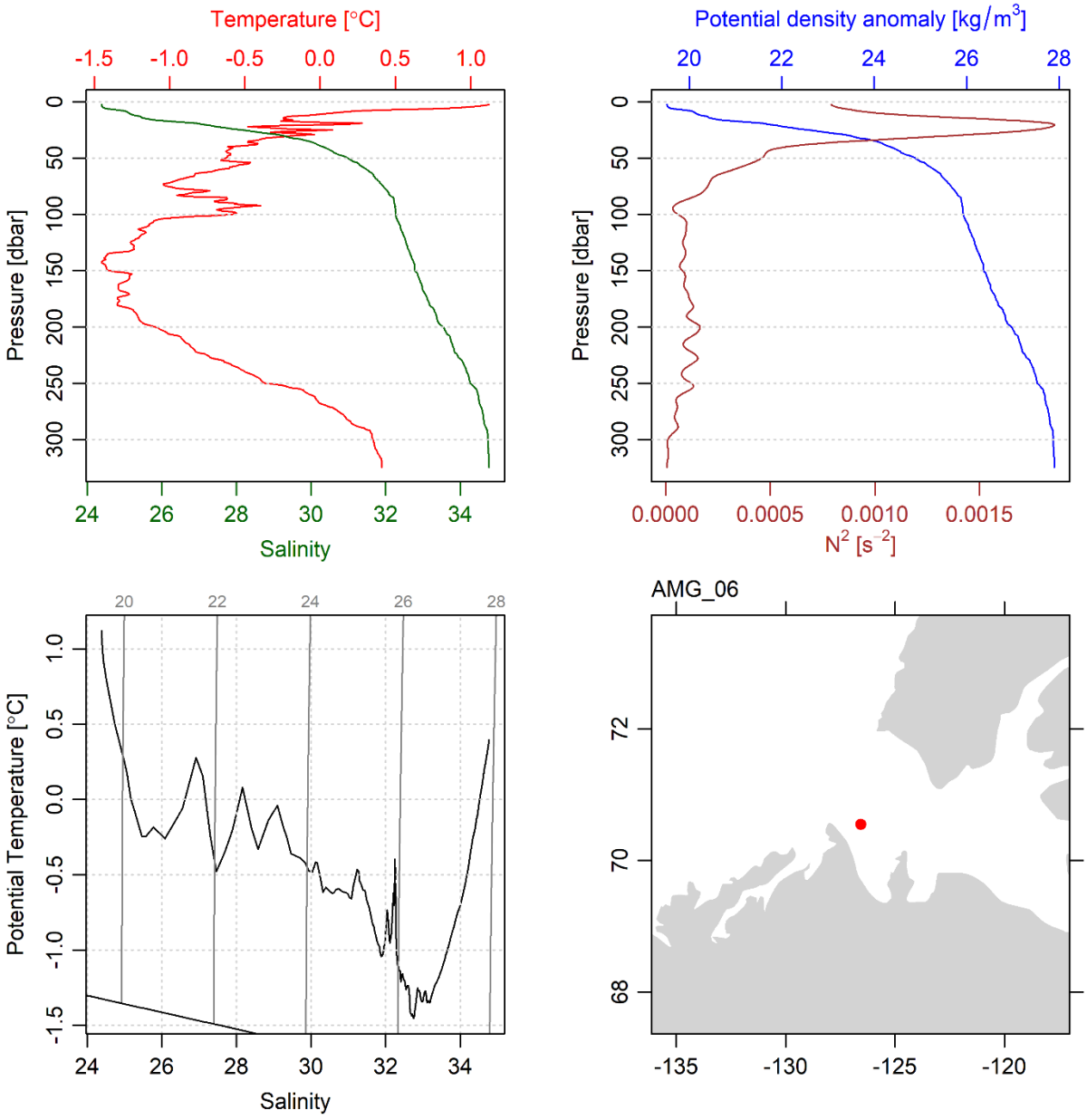

Potential density anomaly [kg/m3]
20 21 22 23 24 25 26
Pressure [dbar]
0 20 40 60 80 100 120
0.0000 0.0010 0.0020 0.0030
N2 [s−2]

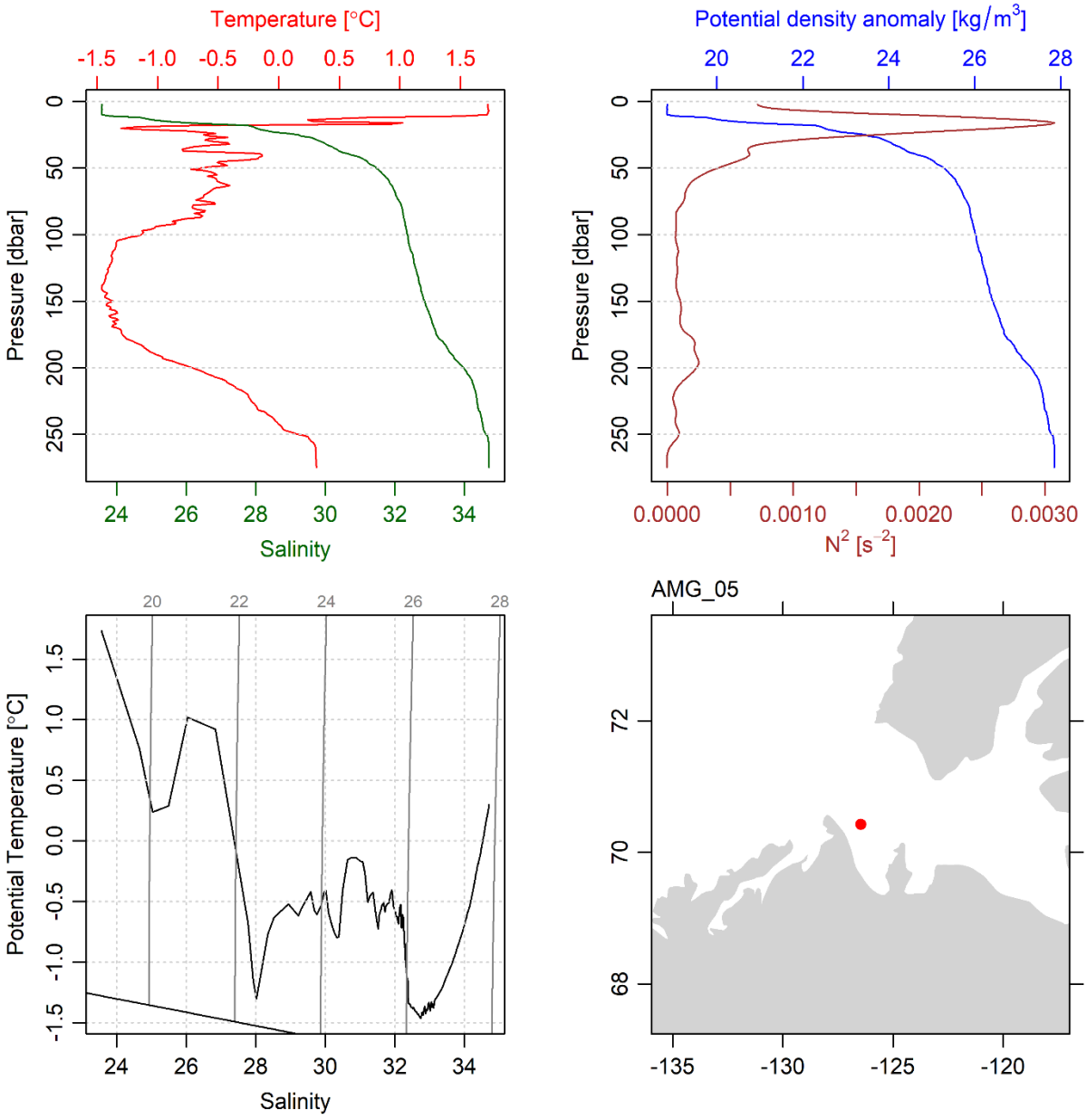

20 21 22 23 24 25 26
Potential Temperature [°C]
-1.0 -0.5 0.0 0.5 1.0 1.5 2.0
24 26 28 30 32
Salinity

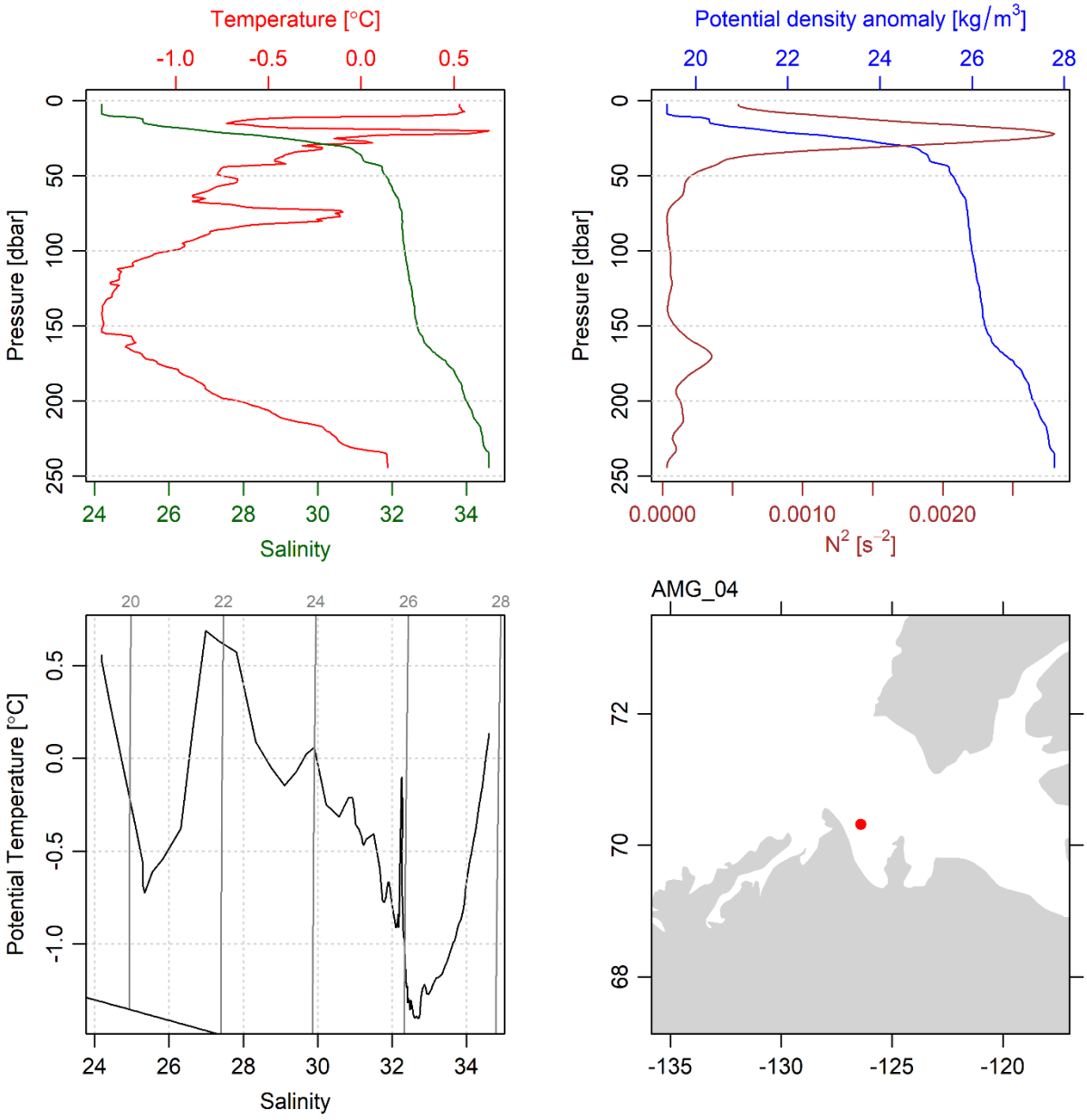

FKN_04
72
70
68
-135 -130 -125 -120

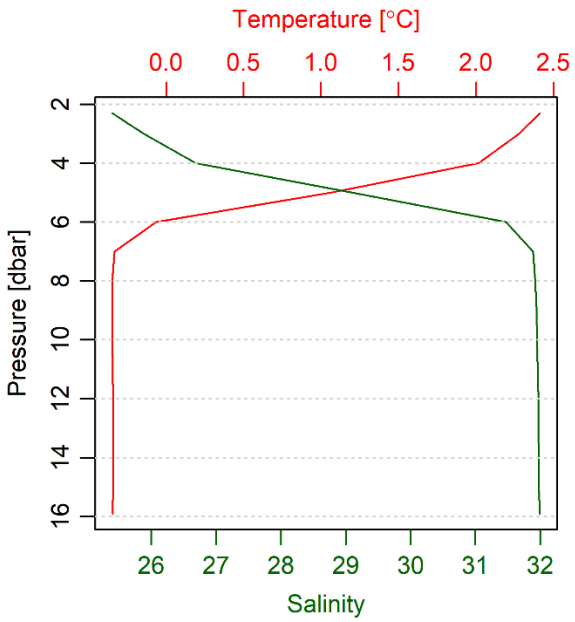

Temperature [°C]
0
1
2
3
Pressure [dbar]
0
20
40
60
80
22
24
26
28
30
32
Salinity
Potential density anomaly [kg/m3]
18
20
22
24
0.000
0.004
0.008
0.012
N2 [s−2]
Potential Temperature [°C]
FKN_07
72
70
68
-135
-130
-125
-120

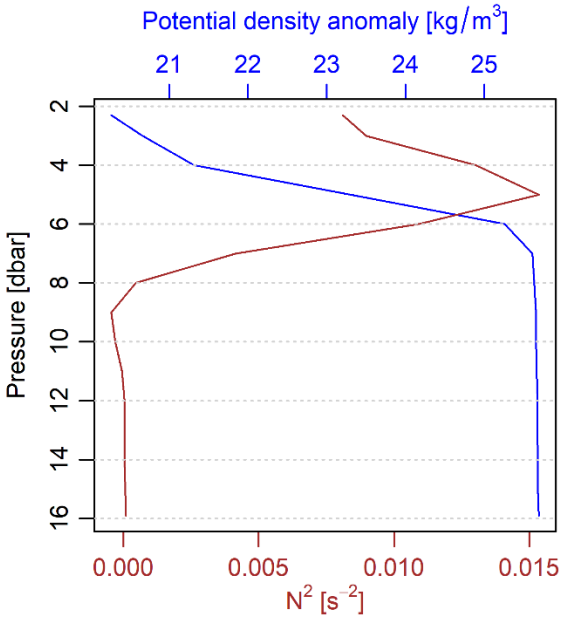

Temperature [°C]
-1
0
1
2
3
Pressure [dbar]
0
50
100
150
24
26
28
30
32
Salinity
Potential density anomaly [kg/m3]
18
20
22
24
26
0.0000
0.0010
0.0020
0.0030
N2 [s−2]
Potential Temperature [°C]
FEX_HC01
72
70
68
-135
-130
-125
-120

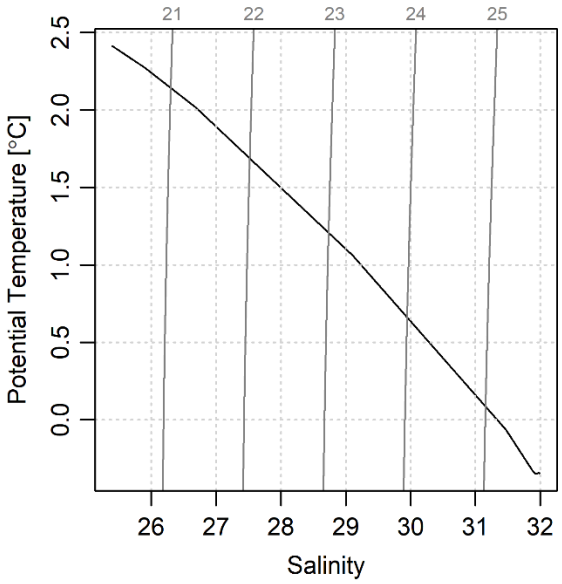

Temperature [°C]
-1.5
-1.0
-0.5
0.0
0.5
1.0
Pressure [dbar]
0
50
100
150
200
250
300
24
26
28
30
32
34
Salinity
Potential density anomaly [kg/m3]
20
22
24
26
28
0.0000
0.0005
0.0010
0.0015
N2 [s−2]
Potential Temperature [°C]
AMG_06
72
70
68
-135
-130
-125
-120

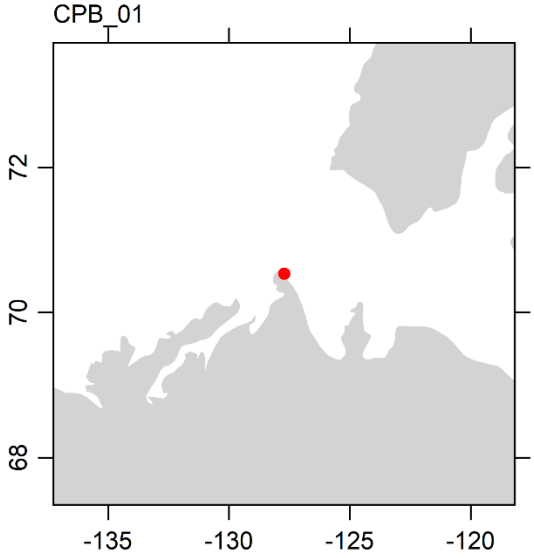

Temperature [°C]
-1.5 -1.0 -0.5 0.0 0.5 1.0 1.5
Pressure [dbar]
0 50 100 150 200 250
24 26 28 30 32 34
Salinity
Potential density anomaly [kg/m3]
20 22 24 26 28
0.0000 0.0010 0.0020 0.0030
N2 [s−2]
Potential Temperature [°C]
-1.5 -1.0 -0.5 0.0 0.5 1.0 1.5
AMG_05
72 70 68
-135 -130 -125 -120

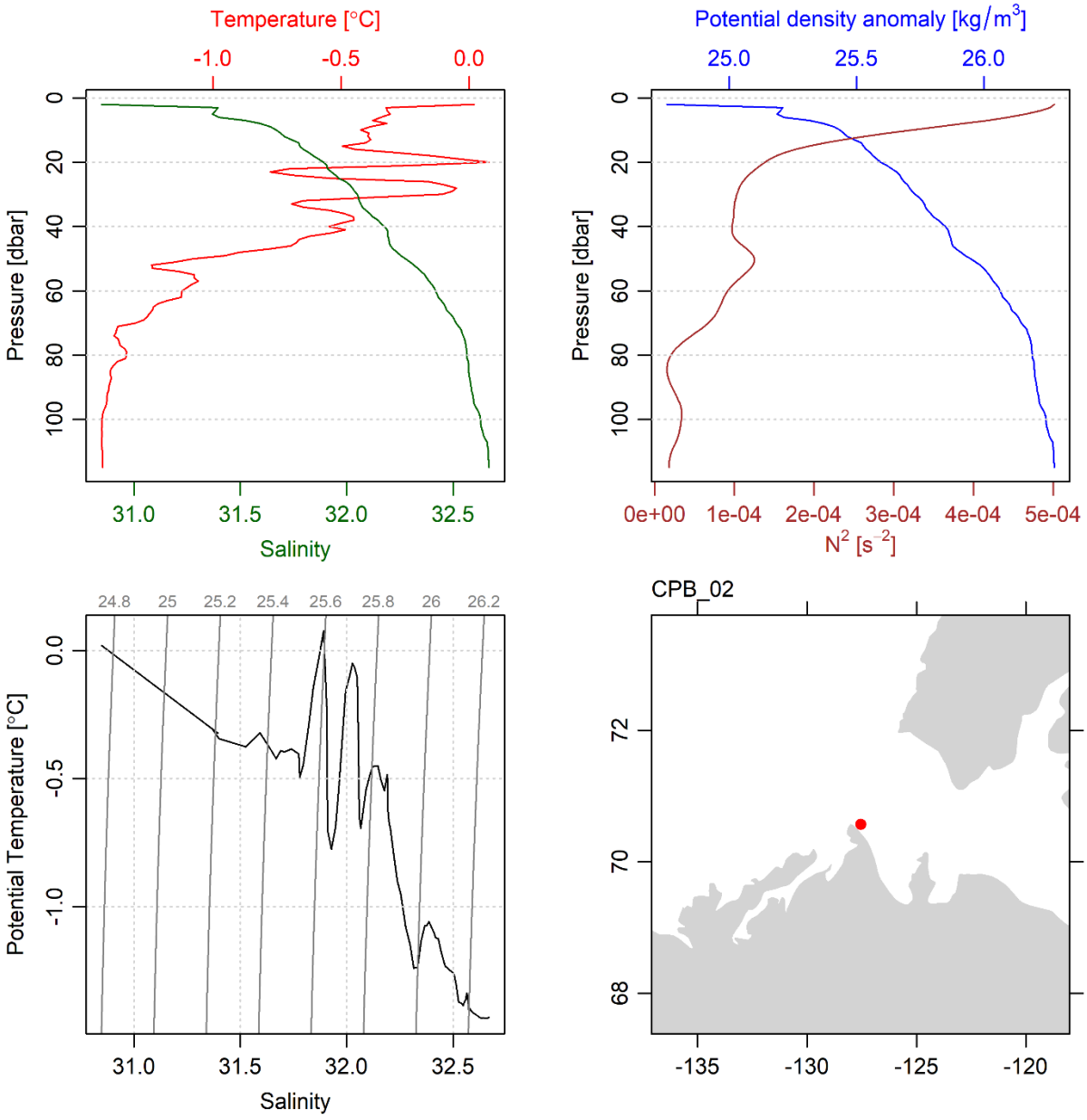

Temperature [°C]
-1.0
-0.5
0.0
0.5
Pressure [dbar]
0
50
100
150
200
250
24
26
28
30
32
34
Salinity
Potential density anomaly [kg/m3]
20
22
24
26
28
0.0000
0.0010
0.0020
N2 [s−2]
Potential Temperature [°C]
AMG_04
72
70
68
-135
-130
-125
-120

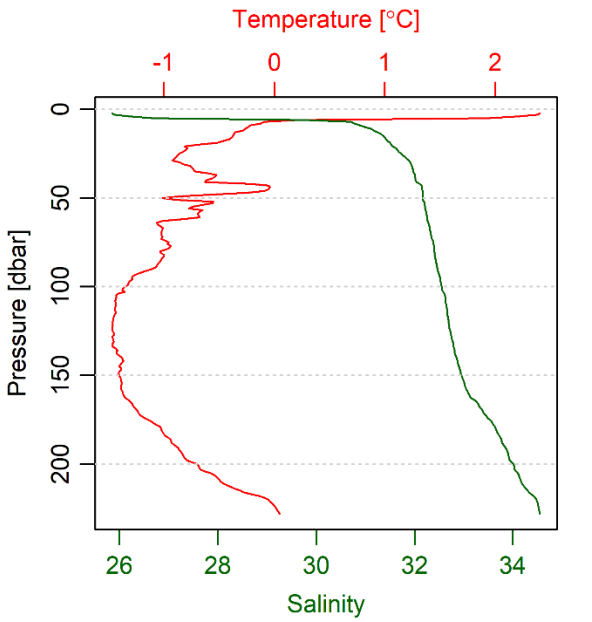

Temperature [°C]
0.0
0.5
1.0
1.5
2.0
2.5
Pressure [dbar]
2
4
6
8
10
12
14
16
26
27
28
29
30
31
32
Salinity

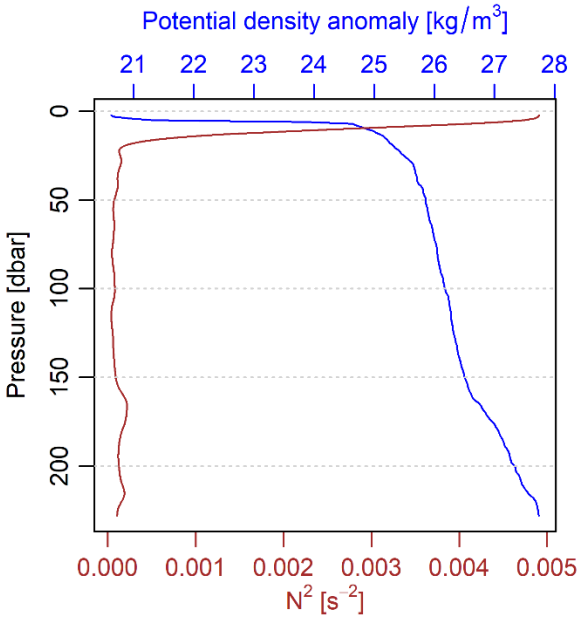

Potential density anomaly [kg/m3]
21
22
23
24
25
Pressure [dbar]
2
4
6
8
10
12
14
16
0.000
0.005
0.010
0.015
N2 [s−2]

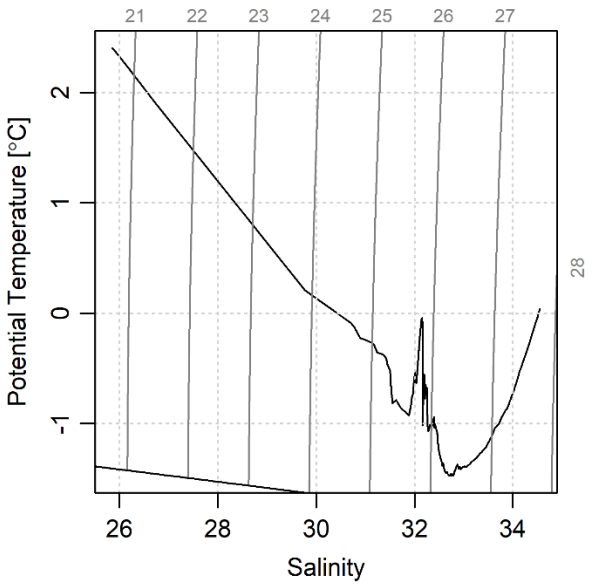

21
22
23
24
25
Potential Temperature [°C]
0.0
0.5
1.0
1.5
2.0
2.5
26
27
28
29
30
31
32
Salinity

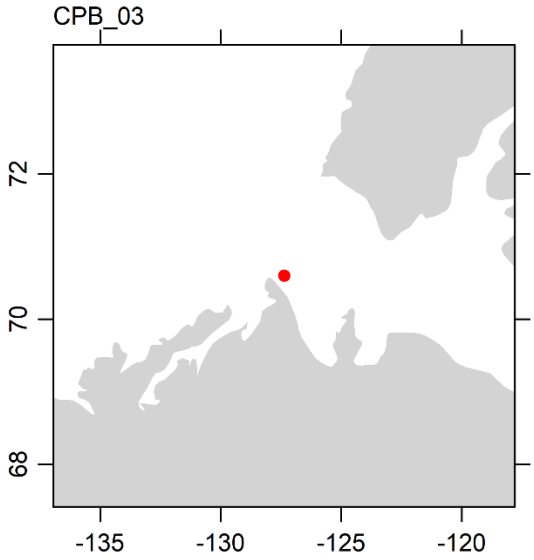

CPB_01
72
70
68
-135
-130
-125
-120

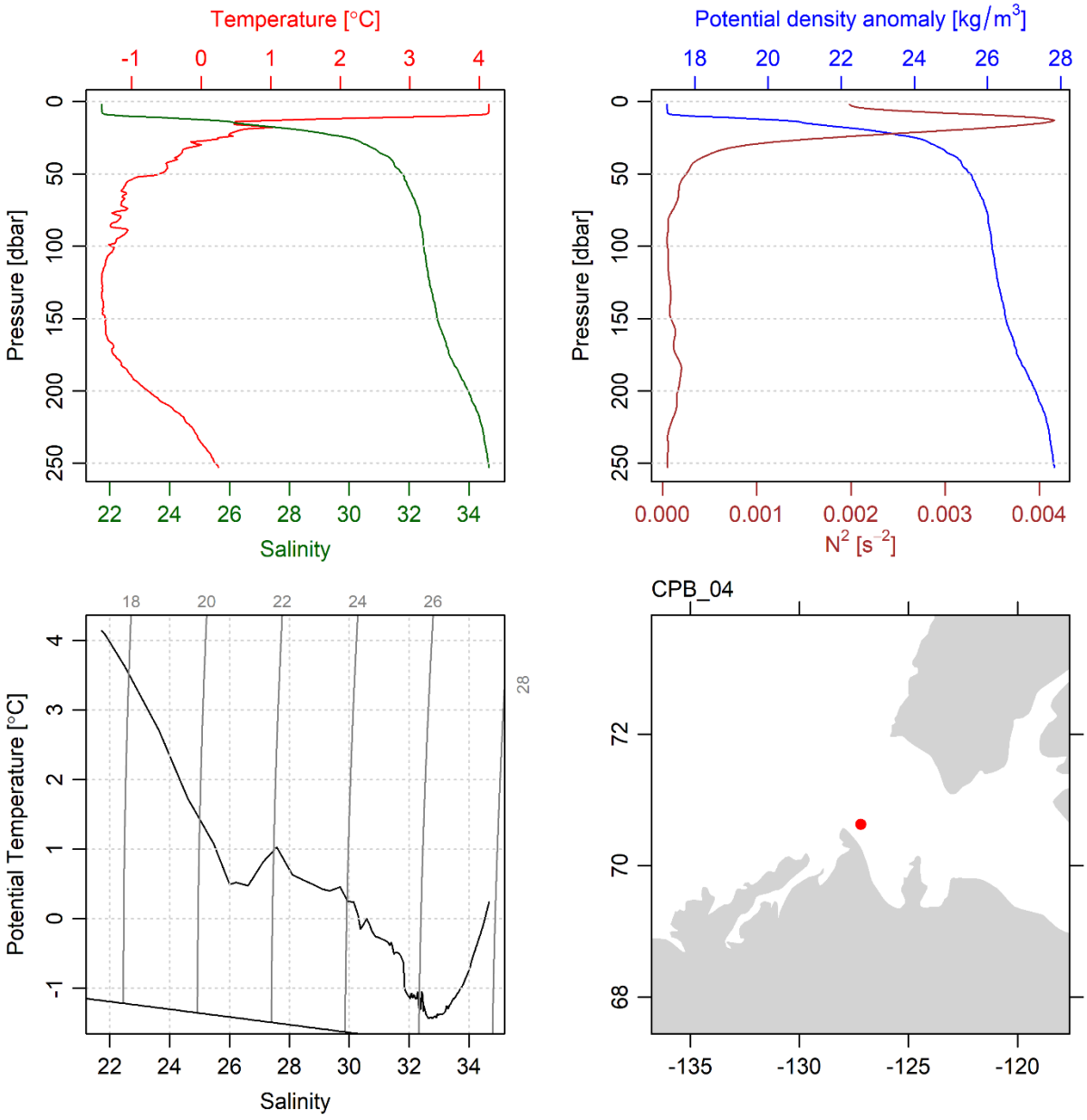

Temperature [°C]
-1.0
-0.5
0.0
Pressure [dbar]
0
20
40
60
80
100
31.0
31.5
32.0
32.5
Salinity
Potential density anomaly [kg/m3]
25.0
25.5
26.0
0e+00
1e-04
2e-04
3e-04
4e-04
5e-04
N2 [s−2]
24.8
25
25.2
25.4
25.6
25.8
26
26.2
Potential Temperature [°C]
CPB_02
72
70
68
-135
-130
-125
-120

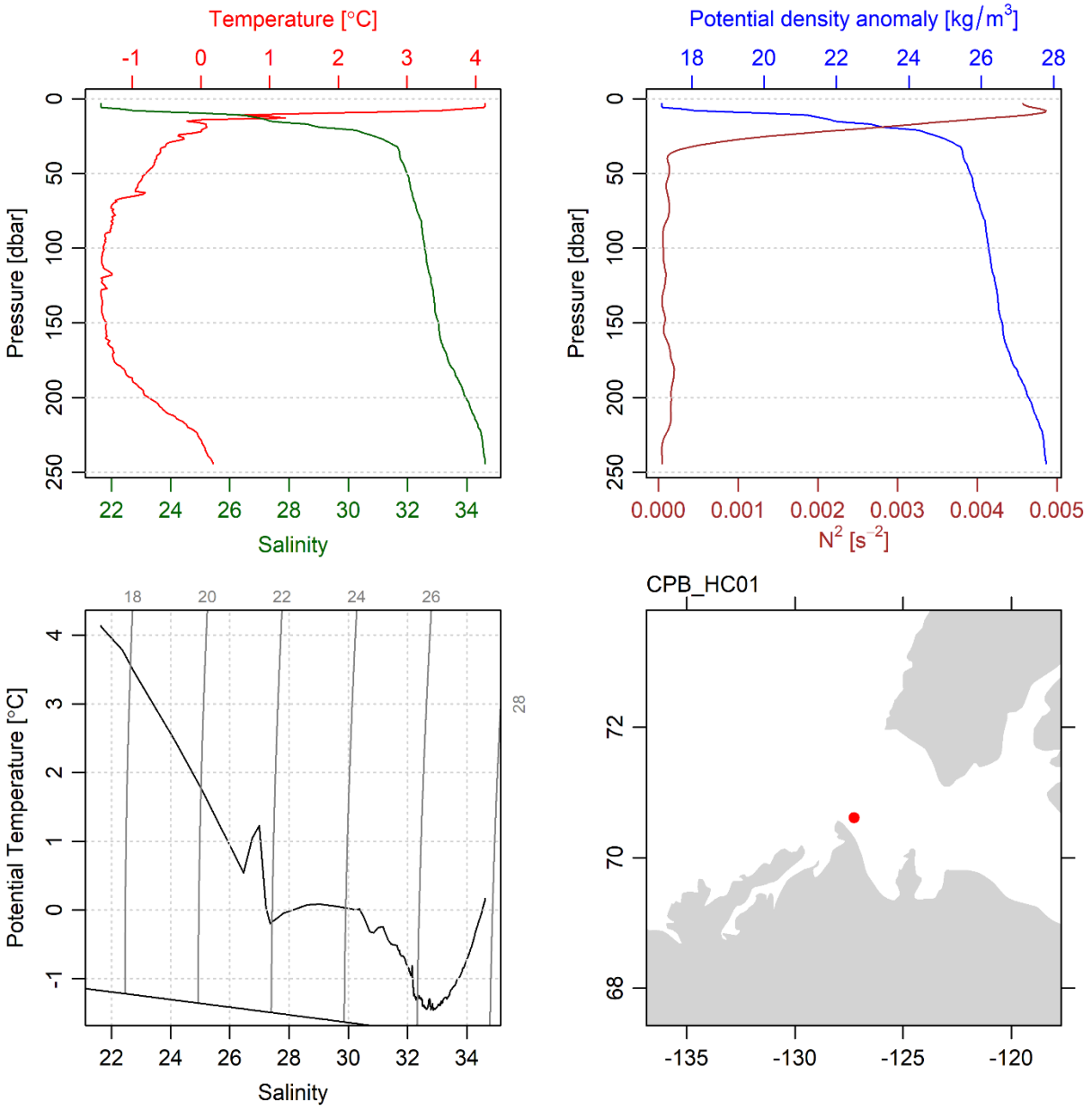

Temperature [°C]
-1
0
1
2
Pressure [dbar]
0
50
100
150
200
26
28
30
32
34
Salinity

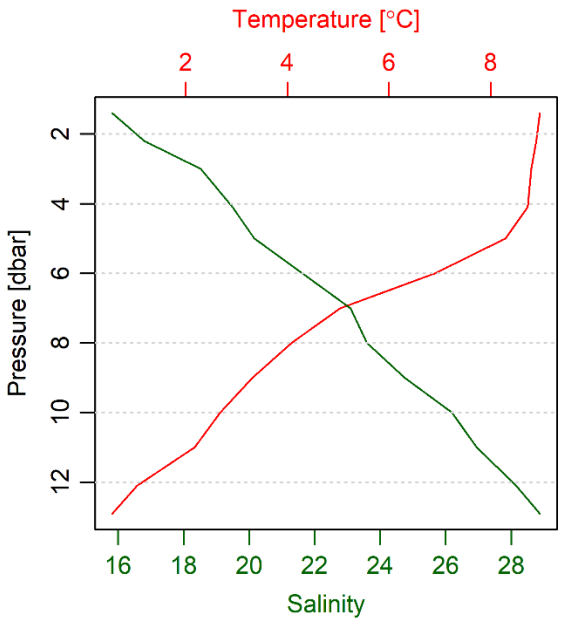

Potential density anomaly [kg/m3]
21
22
23
24
25
26
27
28
Pressure [dbar]
0
50
100
150
200
0.000
0.001
0.002
0.003
0.004
0.005
N2 [s−2]

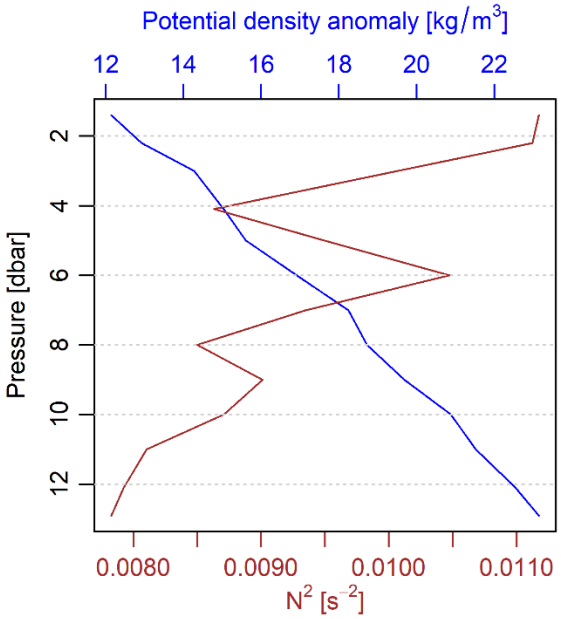

21
22
23
24
25
26
27
Potential Temperature [°C]
2
1
0
-1
28
26
28
30
32
34
Salinity

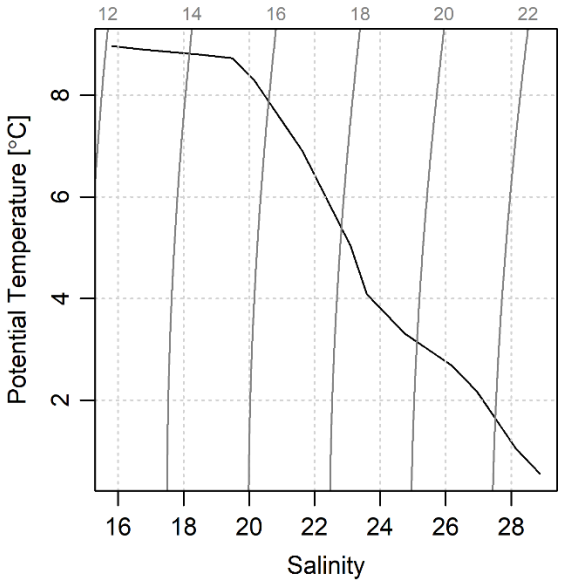

CPB_03
72
70
68
-135
-130
-125
-120

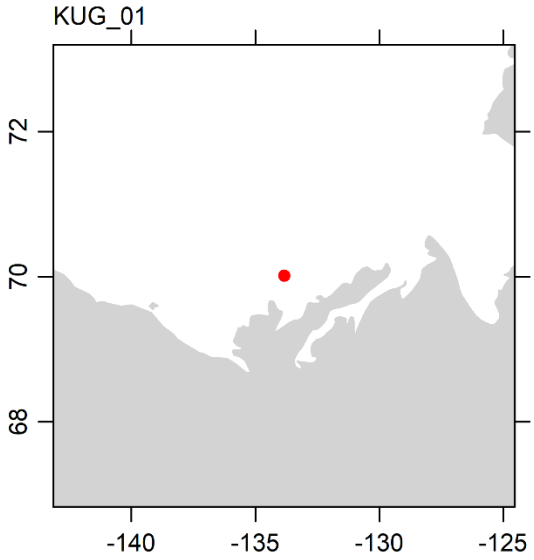

Temperature [°C]
-1
0
1
2
3
4
Pressure [dbar]
0
50
100
150
200
250
22
24
26
28
30
32
34
Salinity
Potential density anomaly [kg/m3]
18
20
22
24
26
28
0.000
0.001
0.002
0.003
0.004
N2 [s−2]
Potential Temperature [°C]
28
CPB_04
72
70
68
-135
-130
-125
-120

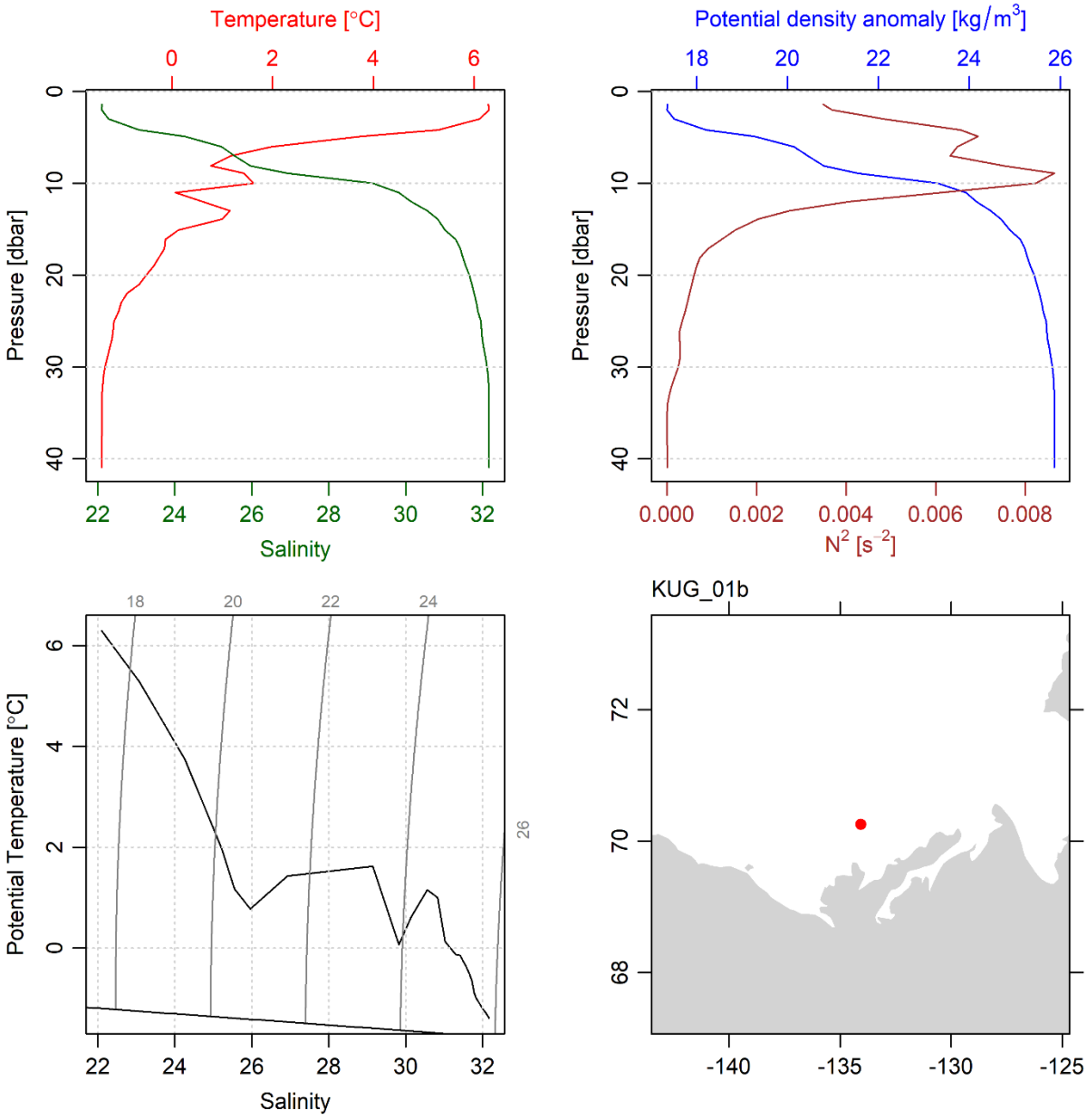

Temperature [°C]
-1
0
1
2
3
4
Pressure [dbar]
0
50
100
150
200
250
22
24
26
28
30
32
34
Salinity
Potential density anomaly [kg/m3]
18
20
22
24
26
28
0.000
0.001
0.002
0.003
0.004
0.005
N2 [s−2]
Potential Temperature [°C]
28
CPB_HC01
72
70
68
-135
-130
-125
-120

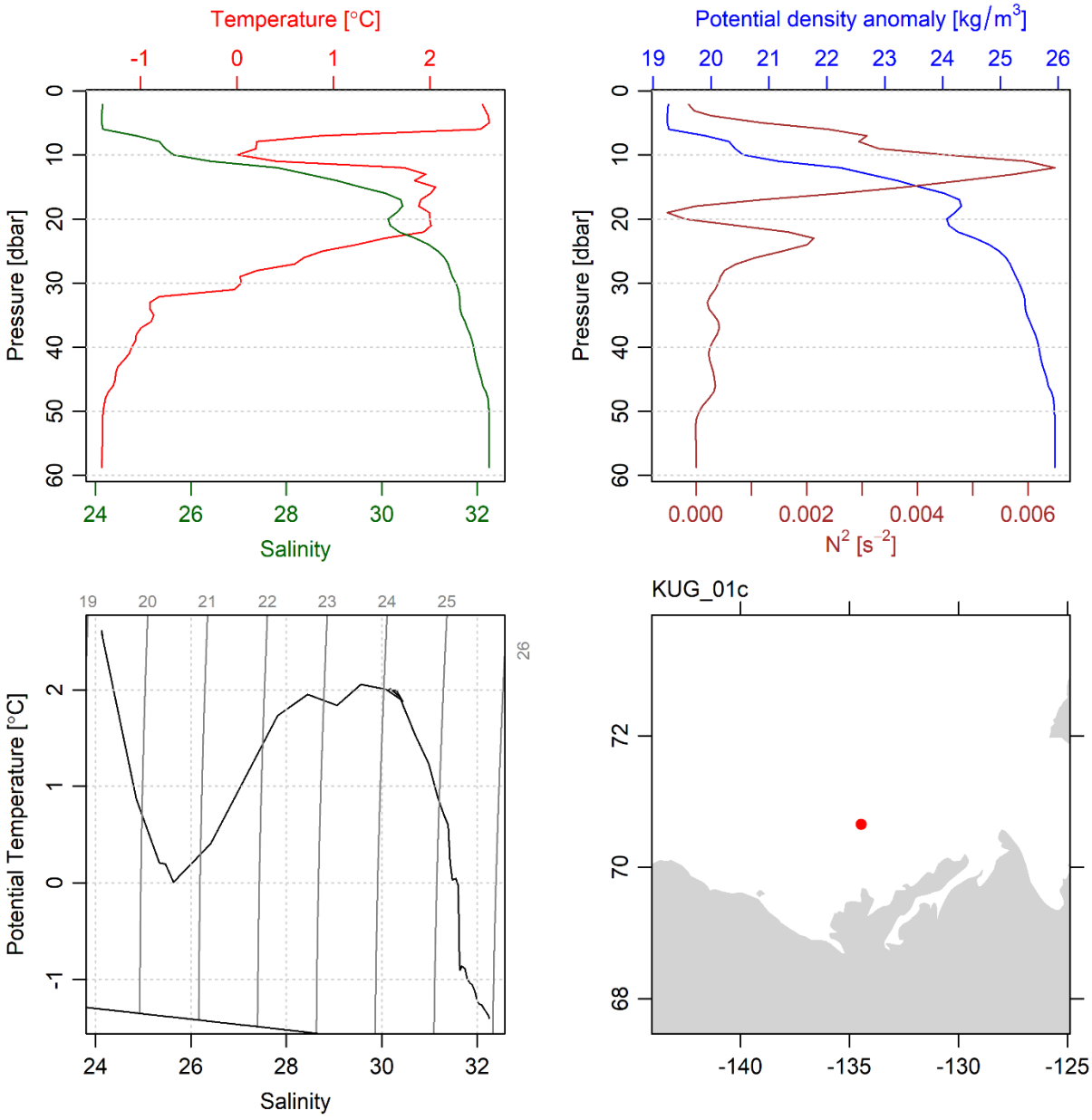

Temperature [°C]
2
4
6
8
Pressure [dbar]
2
4
6
8
10
12
16
18
20
22
24
26
28
Salinity

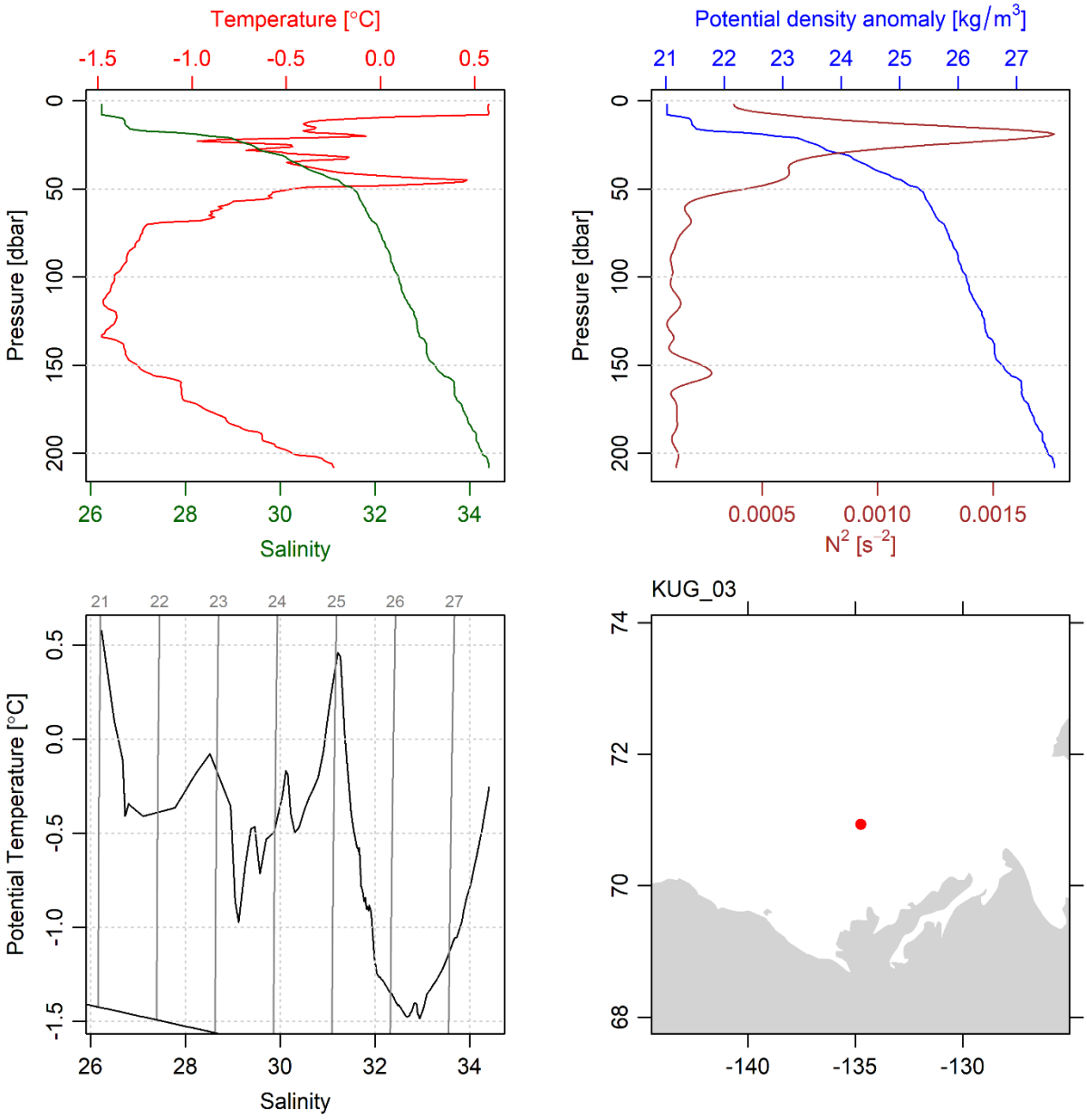

Potential density anomaly [kg/m3]
12
14
16
18
20
22
Pressure [dbar]
2
4
6
8
10
12
0.0080
0.0090
0.0100
0.0110
N2 [s−2]

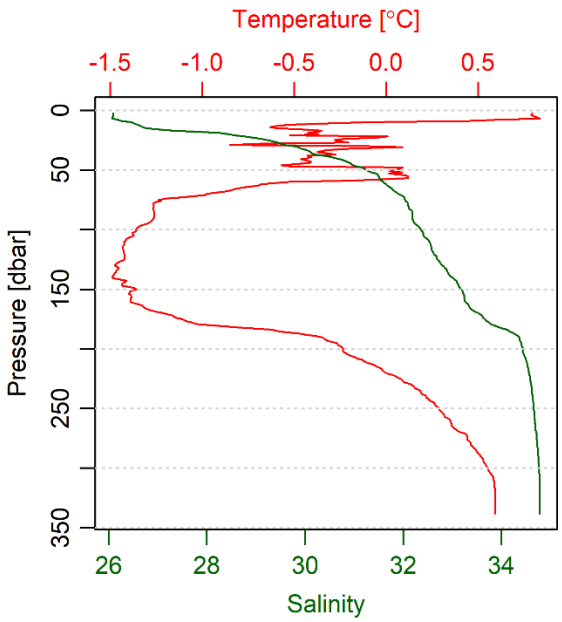

12
14
16
18
20
22
Potential Temperature [°C]
2
4
6
8
16
18
20
22
24
26
28
Salinity

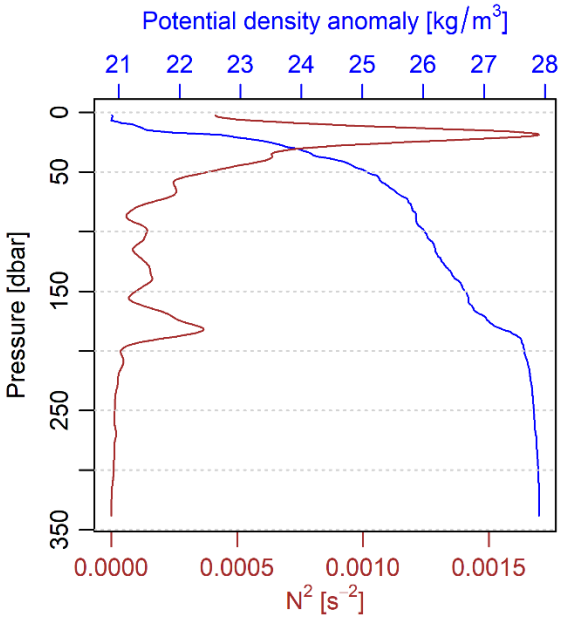

KUG_01
72
70
68
-140
-135
-130
-125

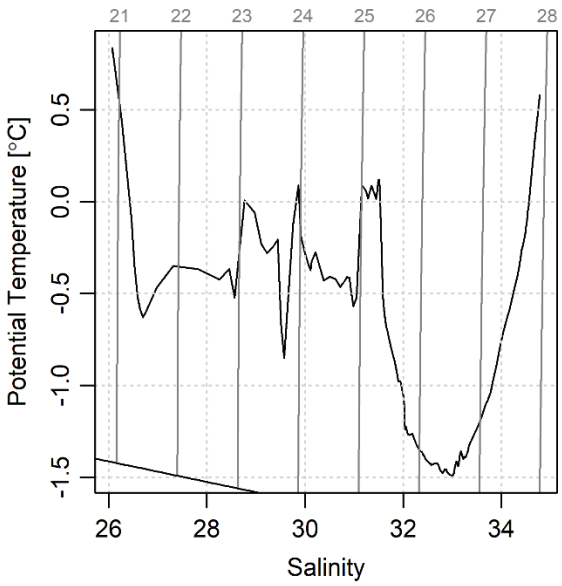

Temperature [°C]
0
2
4
6
Pressure [dbar]
0
10
20
30
40
22
24
26
28
30
32
Salinity
Potential density anomaly [kg/m3]
18
20
22
24
26
0.000
0.002
0.004
0.006
0.008
N2 [s−2]
Potential Temperature [°C]
18
20
22
24
26
KUG_01b
72
70
68
-140
-135
-130
-125

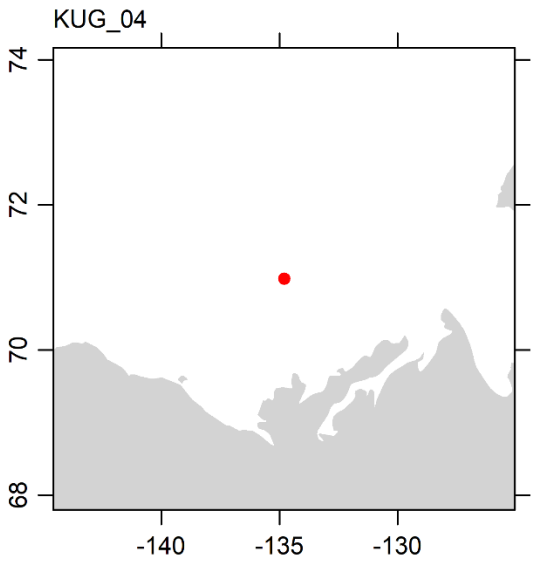

Temperature [°C]
-1
0
1
2
Pressure [dbar]
0
10
20
30
40
50
60
24
26
28
30
32
Salinity
Potential density anomaly [kg/m3]
19
20
21
22
23
24
25
26
0.000
0.002
0.004
0.006
N2 [s−2]
Potential Temperature [°C]
KUG_01c
72
70
68
-140
-135
-130
-125

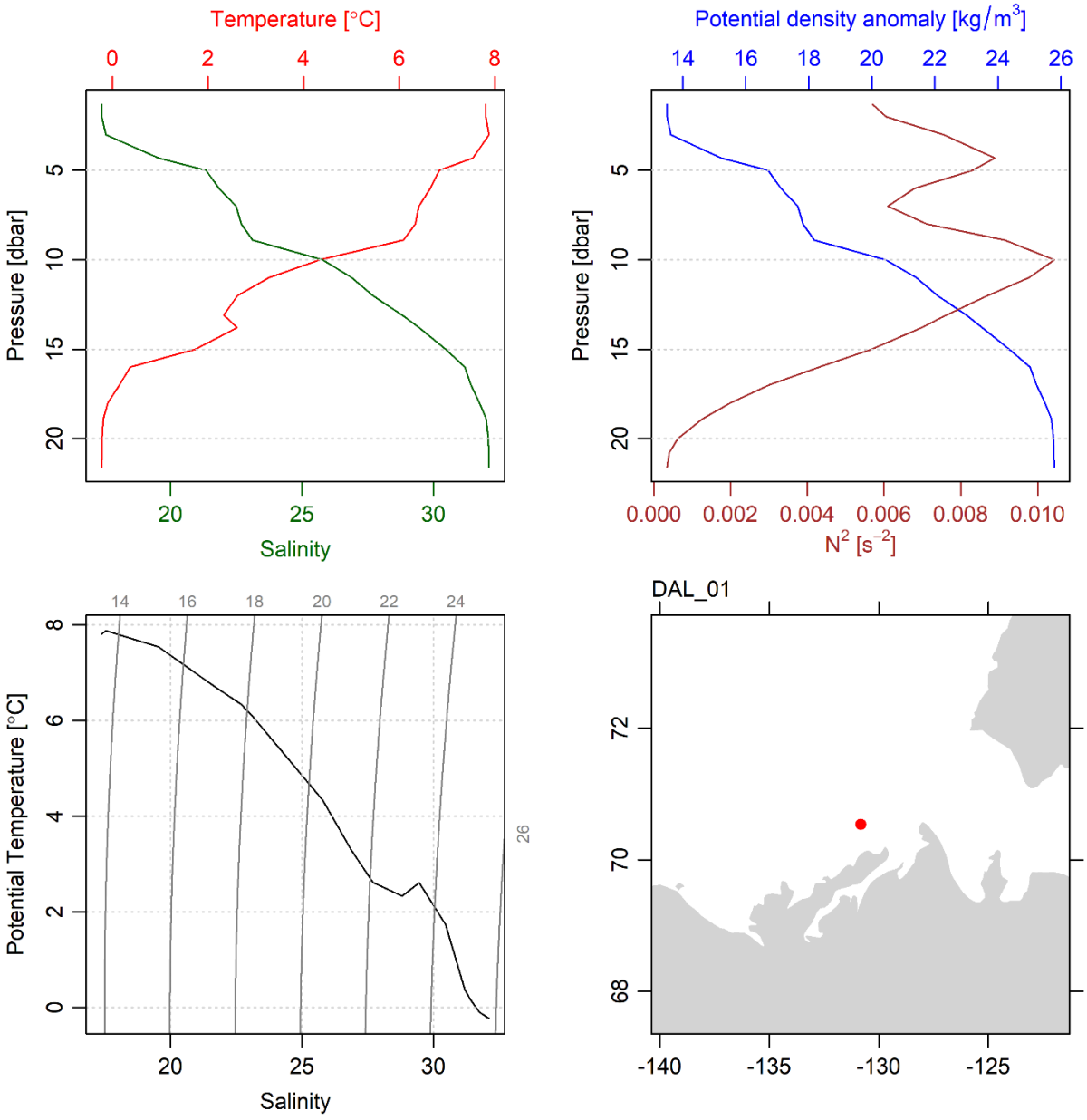

Temperature [°C]
-1.5
-1.0
-0.5
0.0
0.5
Pressure [dbar]
0
50
100
150
200
26
28
30
32
34
Salinity
Potential density anomaly [kg/m3]
21
22
23
24
25
26
27
0.0005
0.0010
0.0015
N2 [s−2]
Potential Temperature [°C]
KUG_03
74
72
70
68
-140
-135
-130

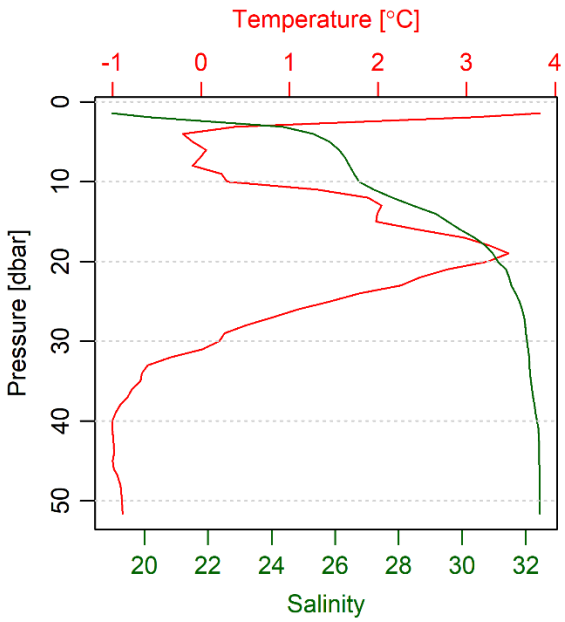

Temperature [°C]
-1.5
-1.0
-0.5
0.0
0.5
Pressure [dbar]
0
50
150
250
350
26
28
30
32
34
Salinity

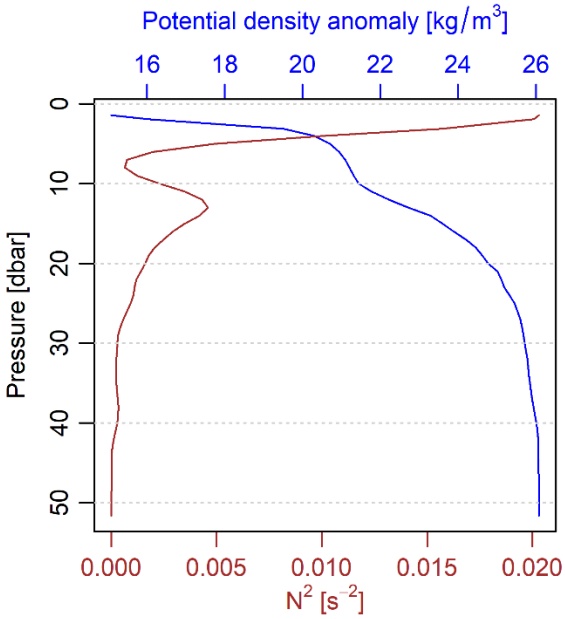

Potential density anomaly [kg/m3]
21
22
23
24
25
26
27
28
Pressure [dbar]
0
50
150
250
350
0.0000
0.0005
0.0010
0.0015
N2 [s−2]

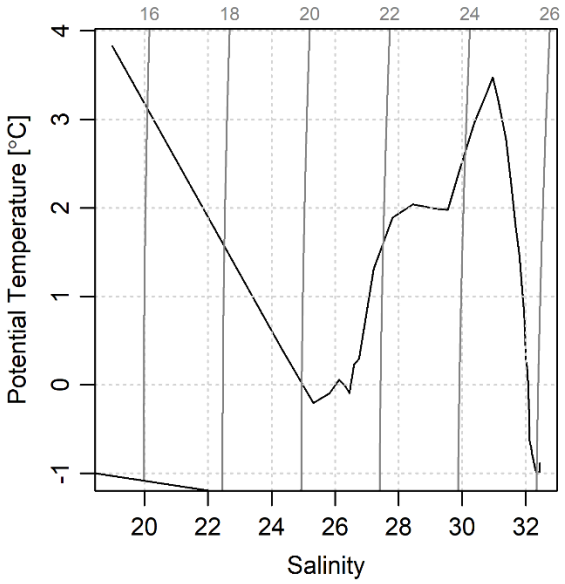

21
22
23
24
25
26
27
28
Potential Temperature [°C]
0.5
0.0
-0.5
-1.0
-1.5
26
28
30
32
34
Salinity

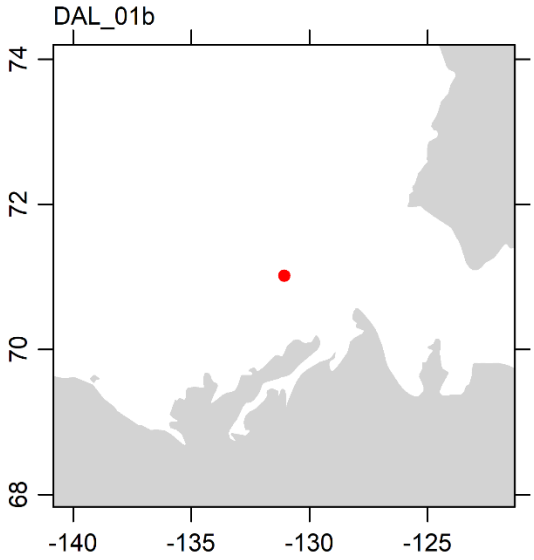

KUG_04
74
72
70
68
-140
-135
-130

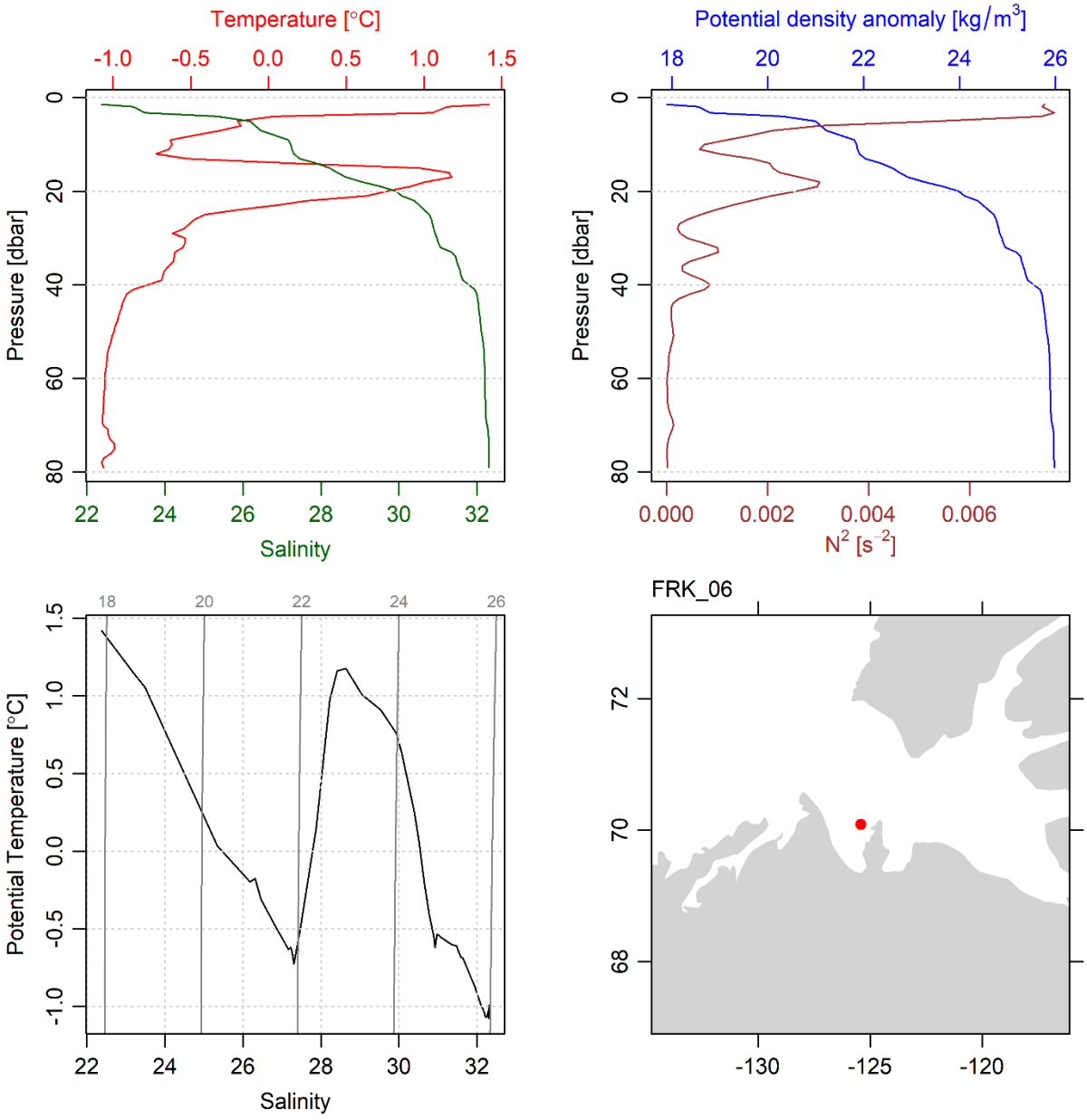

Temperature [°C]
0
2
4
6
8
Pressure [dbar]
5
10
15
20
20
25
30
Salinity
Potential density anomaly [kg/m3]
14
16
18
20
22
24
26
0.000
0.002
0.004
0.006
0.008
0.010
N2 [s−2]
Potential Temperature [°C]
26
DAL_01
72
70
68
-140
-135
-130
-125

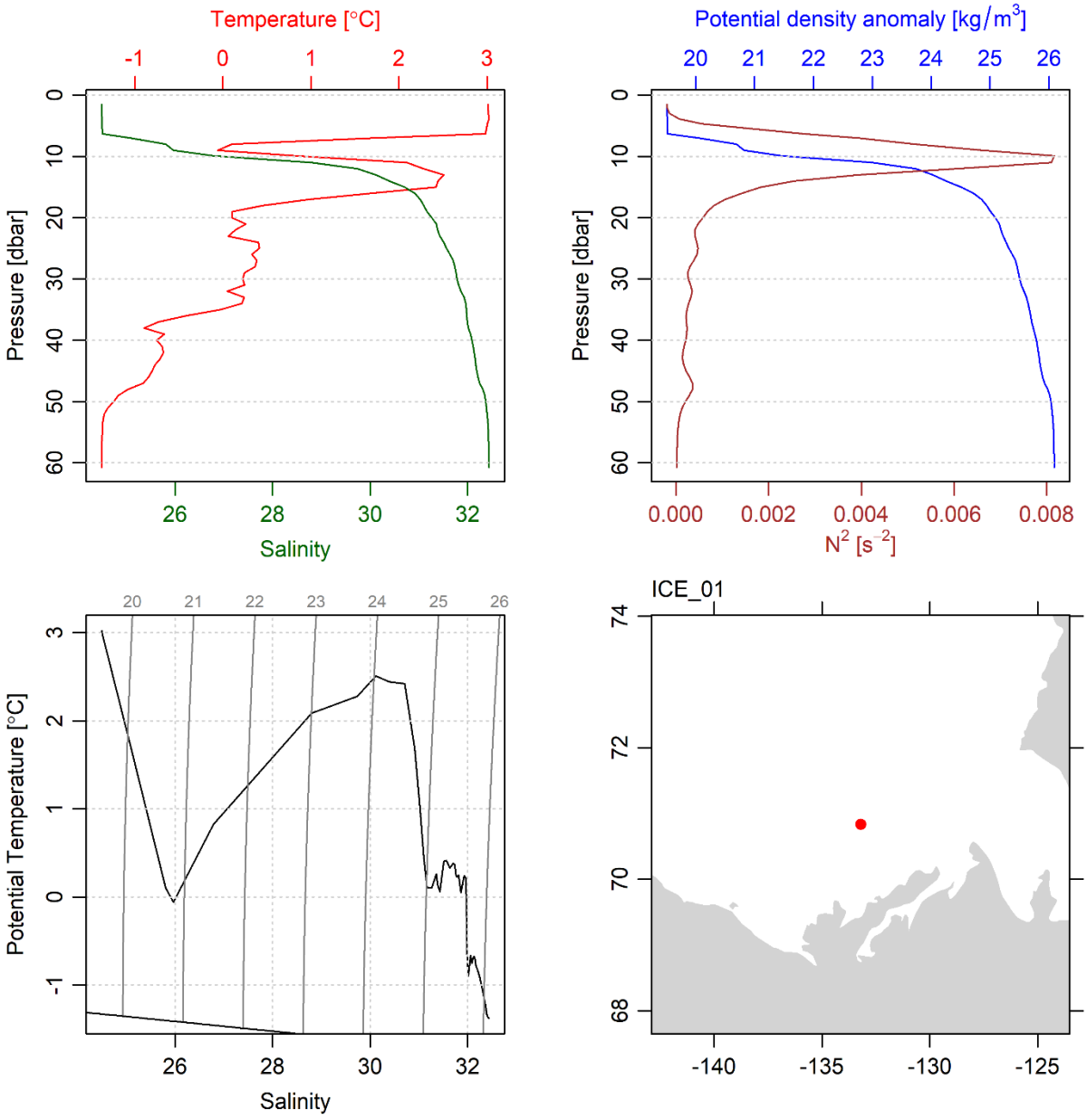

Temperature [°C]
-1
0
1
2
3
4
Pressure [dbar]
0
10
20
30
40
50
20
22
24
26
28
30
32
Salinity

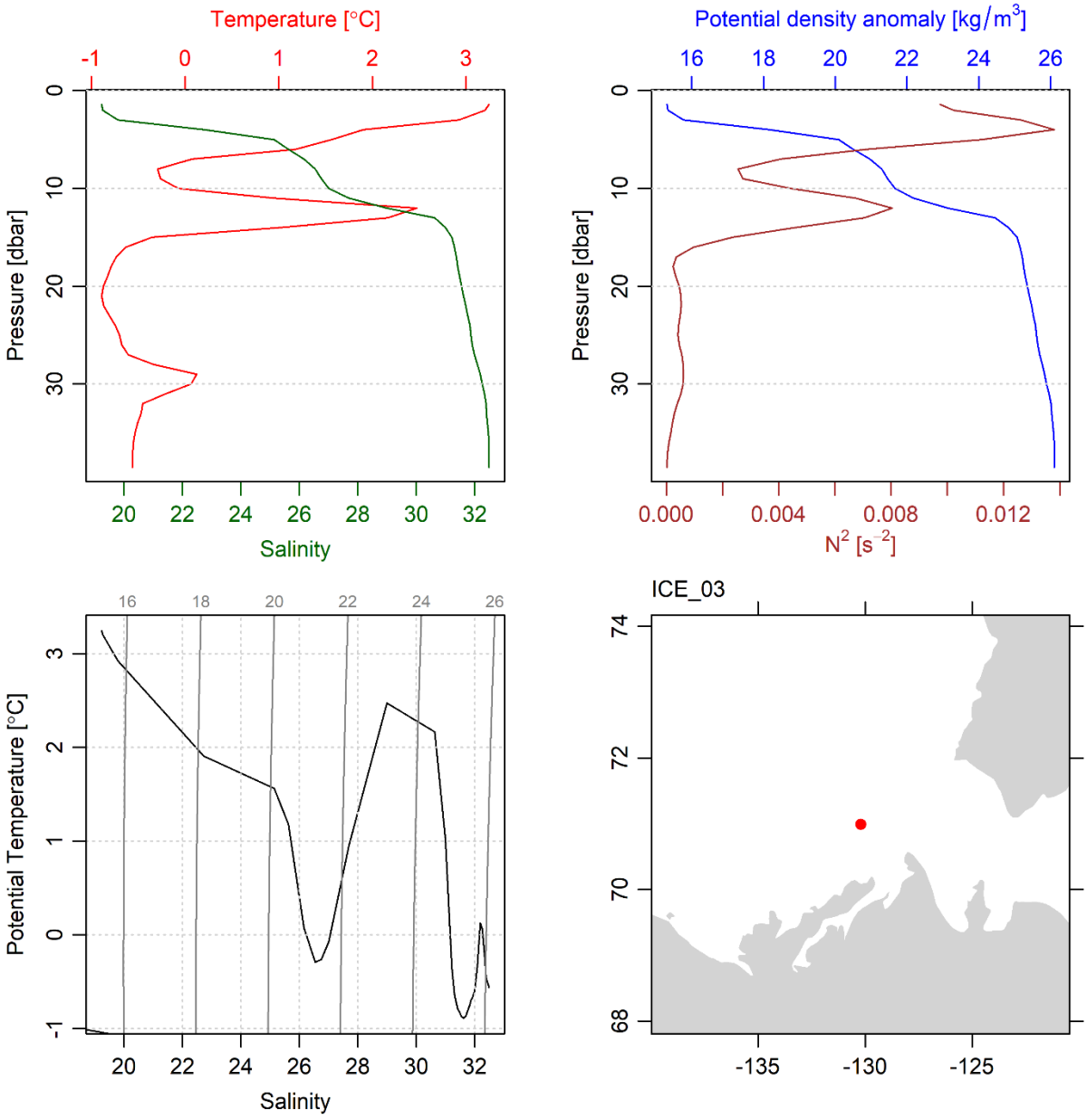

Potential density anomaly [kg/m3]
16
18
20
22
24
26
Pressure [dbar]
0
10
20
30
40
50
0.000
0.005
0.010
0.015
0.020
N2 [s−2]

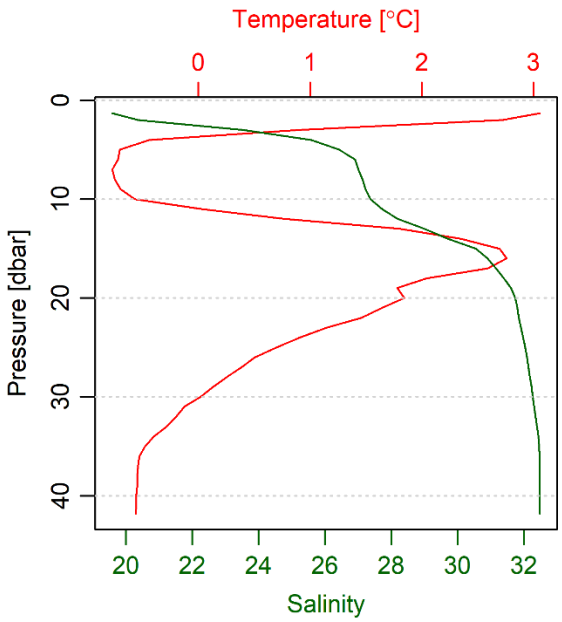

16
18
20
22
24
26
Potential Temperature [°C]
-1
0
1
2
3
4
20
22
24
26
28
30
32
Salinity

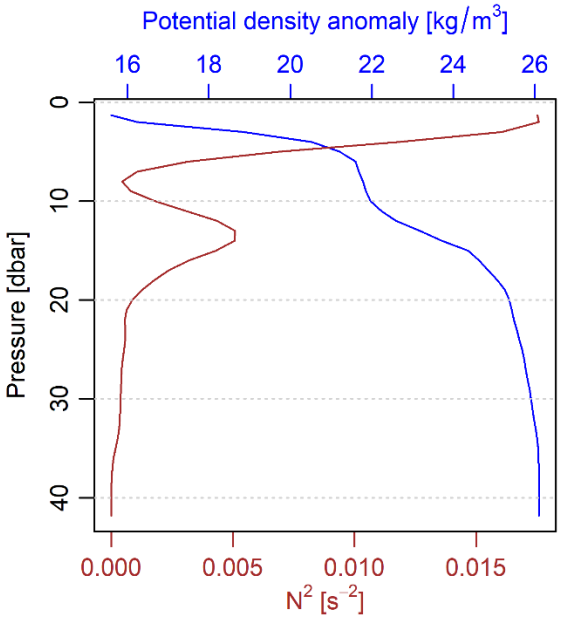

DAL_01b
74
72
70
68
-140
-135
-130
-125

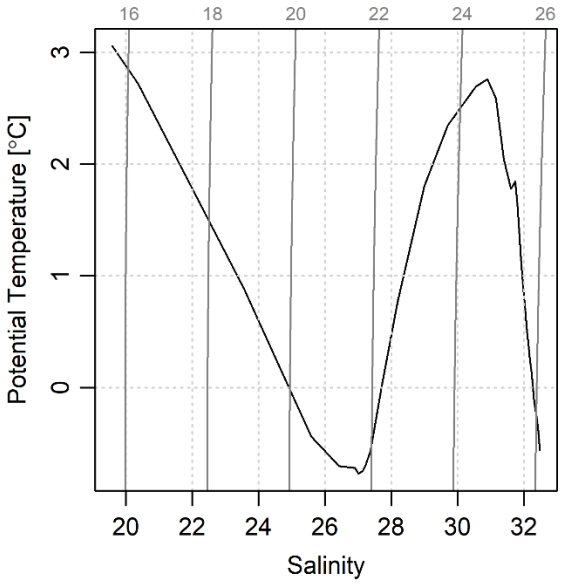

Temperature [°C]
-1.0
-0.5
0.0
0.5
1.0
1.5
Pressure [dbar]
0
20
40
60
80
22
24
26
28
30
32
Salinity
Potential density anomaly [kg/m3]
18
20
22
24
26
0.000
0.002
0.004
0.006
N2 [s−2]
Potential Temperature [°C]
FRK_06
72
70
68
-130
-125
-120

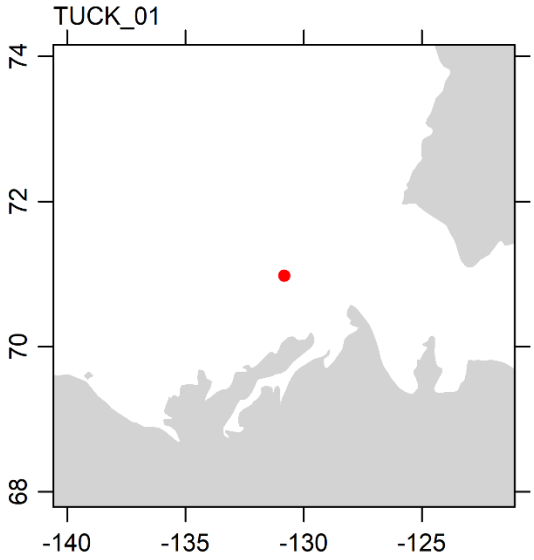

Temperature [°C]
-1
0
1
2
3
Pressure [dbar]
0
10
20
30
40
50
60
26
28
30
32
Salinity
Potential density anomaly [kg/m3]
20
21
22
23
24
25
26
0.000
0.002
0.004
0.006
0.008
N2 [s−2]
Potential Temperature [°C]
ICE_01
74
72
70
68
-140
-135
-130
-125

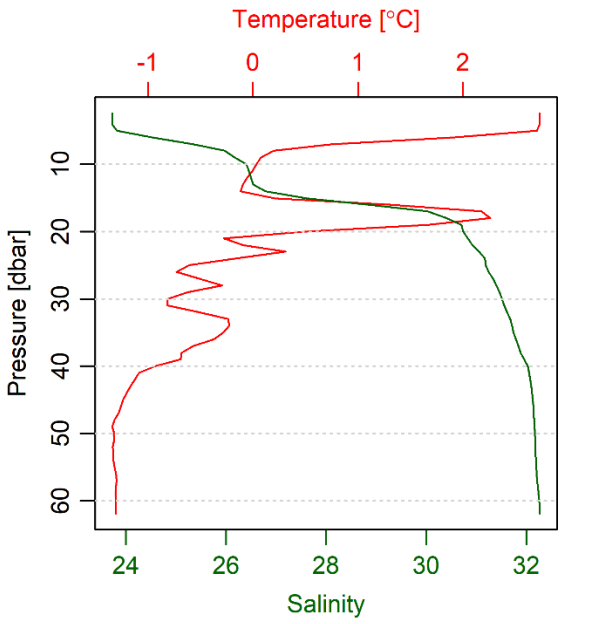

Temperature [°C]
-1
0
1
2
3
Pressure [dbar]
0
10
20
30
20
22
24
26
28
30
32
Salinity
Potential density anomaly [kg/m3]
16
18
20
22
24
26
0.000
0.004
0.008
0.012
N2 [s−2]
Potential Temperature [°C]
ICE_03
74
72
70
68
-135
-130
-125

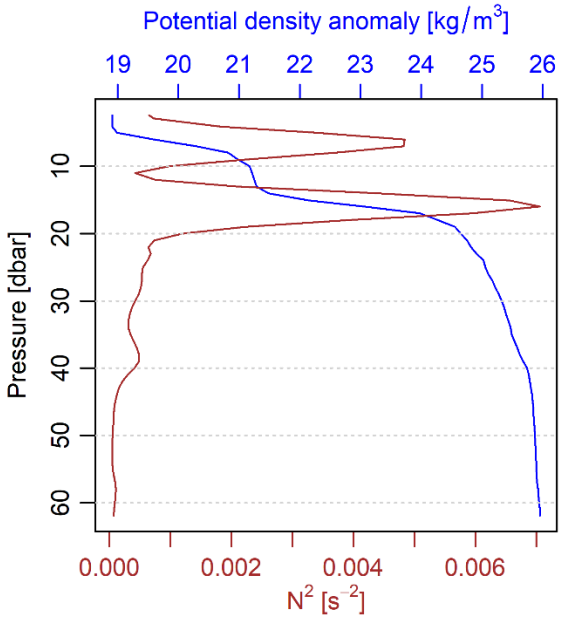

Temperature [°C]
0
1
2
3
Pressure [dbar]
0
10
20
30
40
20
22
24
26
28
30
32
Salinity

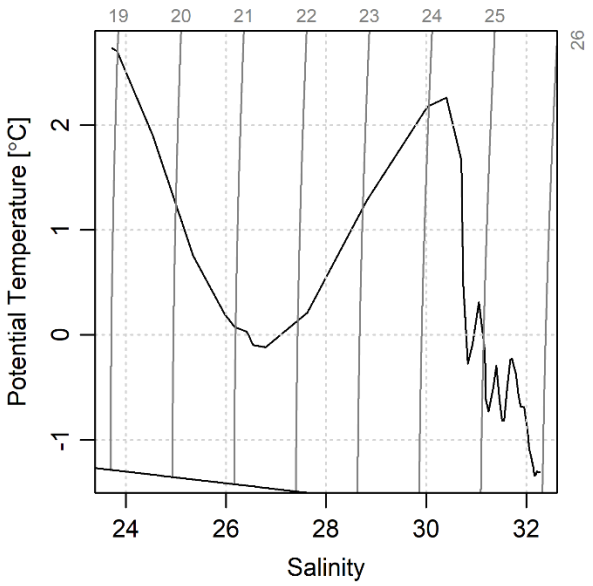

Potential density anomaly [kg/m3]
16
18
20
22
24
26
Pressure [dbar]
0
10
20
30
40
0.000
0.005
0.010
0.015
N2 [s−2]

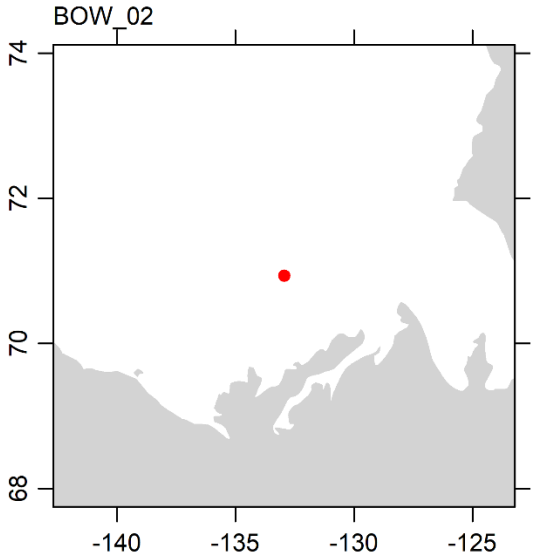

16
18
20
22
24
26
Potential Temperature [°C]
0
1
2
3
20
22
24
26
28
30
32
Salinity

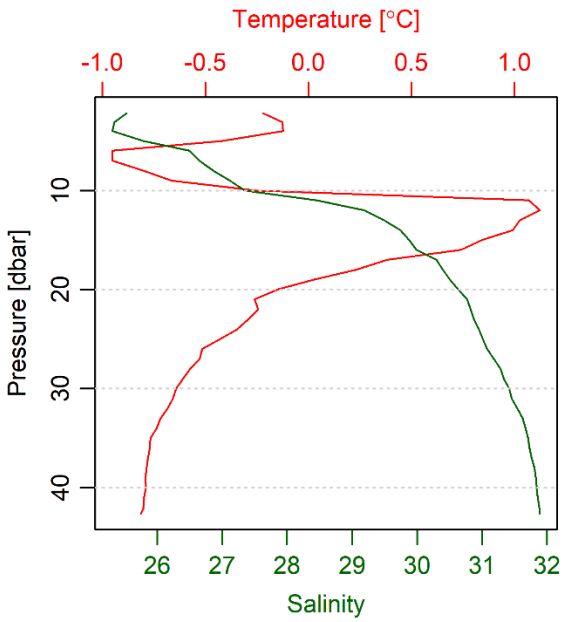

TUCK_01
74
72
70
68
-140
-135
-130
-125

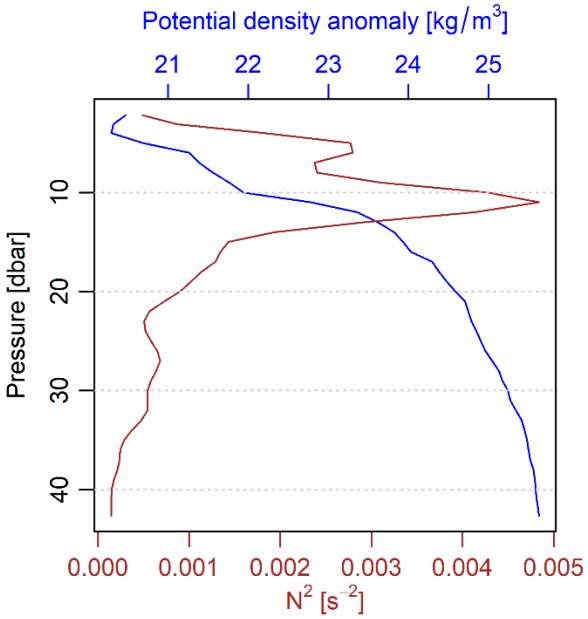

Temperature [°C]
-1
0
1
2
Pressure [dbar]
10
20
30
40
50
60
24
26
28
30
32
Salinity

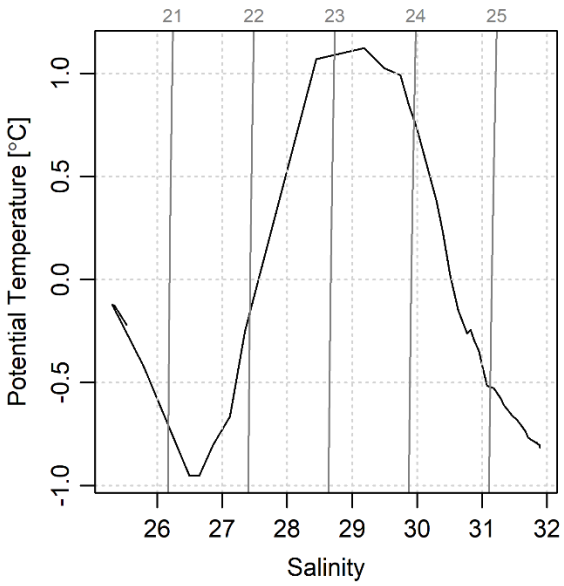

Potential density anomaly [kg/m3]
19
20
21
22
23
24
25
26
Pressure [dbar]
10
20
30
40
50
60
0.000
0.002
0.004
0.006
N2 [s−2]

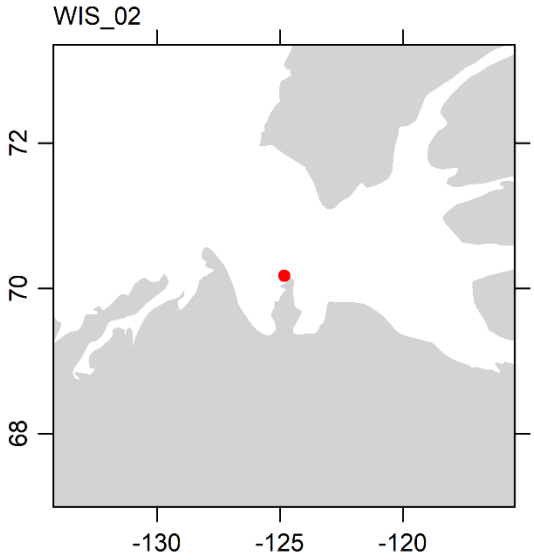

19
20
21
22
23
24
25
26
Potential Temperature [°C]
-1
0
1
2
24
26
28
30
32
Salinity

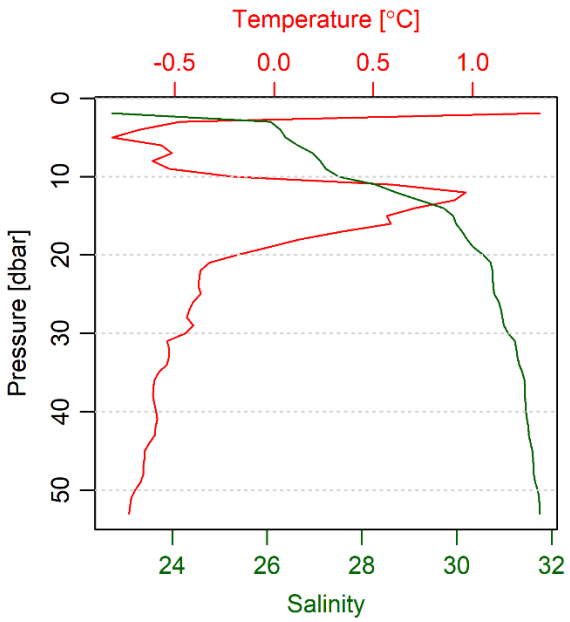

BOW_02
74
72
70
68
-140
-135
-130
-125

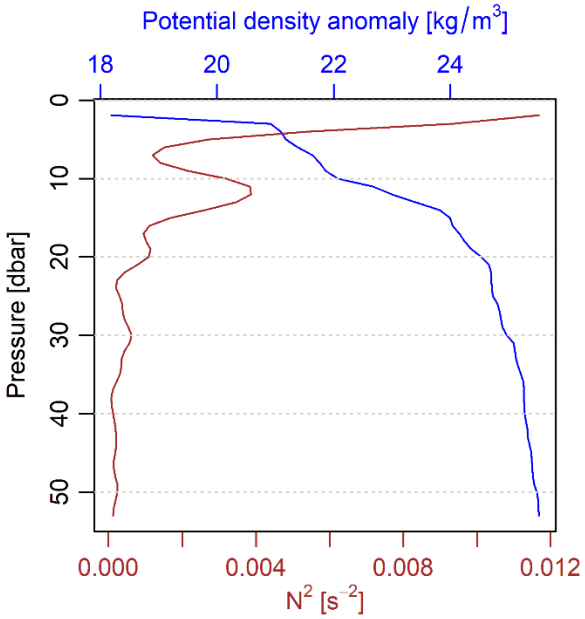

Temperature [°C]
-1.0
-0.5
0.0
0.5
1.0
Pressure [dbar]
10
20
30
40
26
27
28
29
30
31
32
Salinity

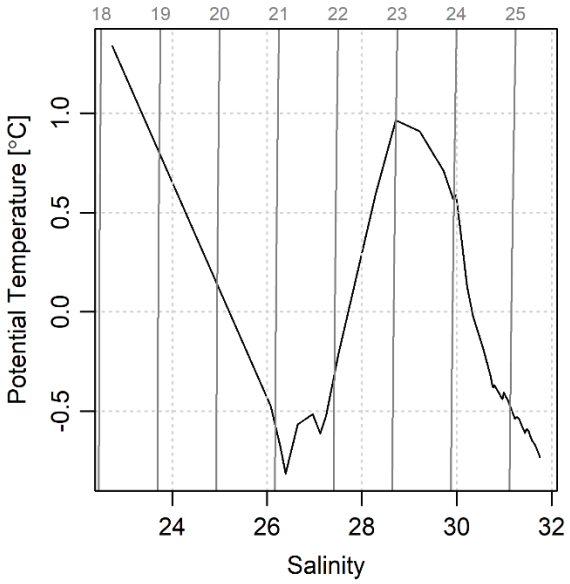

Potential density anomaly [kg/m3]
21
22
23
24
25
Pressure [dbar]
10
20
30
40
0.000
0.001
0.002
0.003
0.004
0.005
N2 [s−2]

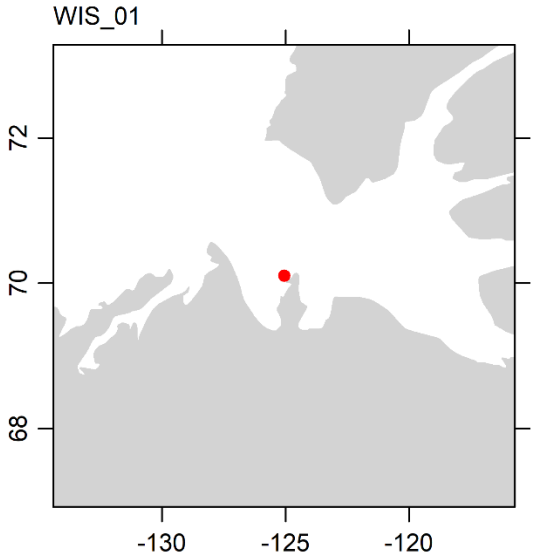

21
22
23
24
25
Potential Temperature [°C]
1.0
0.5
0.0
-0.5
-1.0
26
27
28
29
30
31
32
Salinity


WIS_02
72
70
68
-130
-125
-120


Temperature [°C]
-0.5
0.0
0.5
1.0
Pressure [dbar]
0
10
20
30
40
50
24
26
28
30
32
Salinity


Potential density anomaly [kg/m3]
18
20
22
24
Pressure [dbar]
0
10
20
30
40
50
0.000
0.004
0.008
0.012
N2 [s−2]


18
19
20
21
22
23
24
25
Potential Temperature [°C]
1.0
0.5
0.0
-0.5
24
26
28
30
32
Salinity


WIS_01
72
70
68
-130
-125
-120